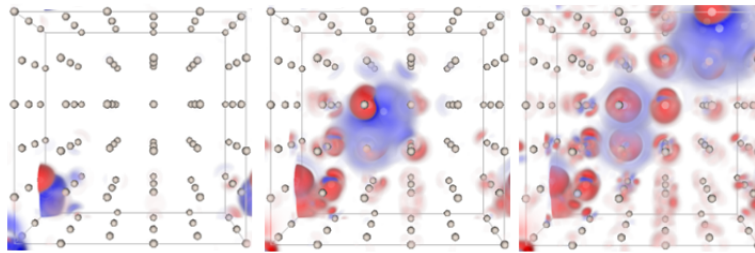


NON-ADIABATIC PROCESSES IN THE
RADIATION DAMAGE OF MATERIALS
FROM FIRST PRINCIPLES



PhD Thesis

by

Rafi Ullah

2018

Supervisor: Emilio Artacho

Co-supervisor: Daniel Sánchez-Portal

eman ta zabal zazu



Universidad Euskal Herriko
del País Vasco Unibertsitatea

Department of Material Physics
University of the Basque Country
Donostia - San Sebastian
Spain.

ابو جی اور امی جان کے نام

Acknowledgements

Firstly, I would like to express my deepest gratitude to my supervisor, *Prof. Emilio Artacho*. Without his continuous support, patience, interest, and guidance this humble effort would not have come to fruition. His depth of knowledge and erudite mentoring, not just as a scientist but as a human being, have been a great influence that I shall carry with me for the rest of my life. It has been a great pleasure working with him. I am thankful to Prof. Daniel Sánchez-Portal, my thesis co-supervisor and collaborator, for his very generous support throughout this thesis.

I am sincerely grateful to my collaborator and mentor *Dr Alfredo Correa*, who I had the opportunity to work with during my visits to LLNL, CA, USA. I have greatly benefitted from his collegial style of mentoring and enthusiastic interest in my work. Thanks are due to my former colleague and dear friend *Dr Fabiano Corsetti*, for his patience, help and bonafide support throughout this work, particularly in the earlier years of this thesis. He made everything easy whether it was debugging a rogue code, an intricate concept of physics or a philosophical discussion. Technical support from *Dr Ahsan Zeb* in the beginning of this thesis is gratefully acknowledged.

During this thesis I have enjoyed the company of my friends and the theory group colleagues *Dr Pablo Aguado* and *Dr Jon Zubelztu*. Having them around along with Fabiano, brought great positivity to the environment in our group. The often extended coffee breaks and the discussions that ensued, from mere gossip to deep philosophical debates, formed the most cherished memories of my PhD experience. I must mention *Dr Ananda K. Sarrella* and *Dr Subir Parui*, for being sincere friends and always there to help.

Dr Mónica García and *Dr Daniel Muñoz-Santiburcio* have helped me translate summary of the thesis into Spanish. *Dr Federico Marchesin* has been very helpful with ensuring the thesis and defence formalities. I have enjoyed tremendous support from the nanoGUNE staff, particularly, *Jose M. Pitarke*, *Miguel Odrizola*, *Julene Lure*, and *Eider García*. I am thankful to *Itziar Otegui* for taking care of the administrative formalities and *Dr Yurdana Castelruiz* for administering the FPI and EEBB fellowships.

Definitely this is due to my parents, and the hard choices they made, that I made it this far. My sincerest gratitude to *Ammi Jee* and *Abbu Jee*, for your prayers, love and unwavering support. I cannot thank enough my elder brother, *Bhai Aman Ullah*, for his love and generosity. Thanks to *Zainab*, *Nasrullah* and *Tassawer* for your love. *Naano Jan!* I am always in need of your prayers.

Last but not the least, I am extremely grateful to my beloved wife, *Ramla*, who has been with me through this for the last couple of years. Her love and support has been a great source of inspiration.

Abstract

We have implemented a real-time time-dependent density-functional theory (RT-TDDFT) algorithm within the SIESTA method. Building on the basic infrastructure of SIESTA we integrate the time-dependent Kohn-Sham equations using the Crank-Nicolson method. Crank-Nicolson integration and other complementary operations are performed in parallel, allowing for the possibility of simulating systems of thousands of atoms. The parallel matrix distribution and manipulation is handled by the SCALAPACK package, and interfaced to SIESTA with the newly-developed MATRIXSWITCH wrapper package. Parallel scalability tests for our new implementation are performed on a system of 5000 atoms, showing a good scaling up to 316 processes.

The direction and impact parameter dependence of electronic stopping power, along with its velocity threshold behavior, is investigated in a prototypical small band gap semiconductor. We calculate the electronic stopping power of H in Ge, a semiconductor with relatively low packing density, using RT-TDDFT. The calculations are carried out in channeling conditions with different impact parameters and in different crystal directions, for projectile velocities ranging from 0.05 to 0.6 atomic units. The satisfactory comparison with available experiments supports the results and conclusions beyond experimental reach. The calculated electronic stopping power is found to be different in different crystal directions; however, strong impact parameter dependence is observed only in one of these directions. The distinct velocity threshold observed in experiments is well reproduced, and its non-trivial relation with the band gap follows a perturbation theory argument surprisingly well. This simple model is also successful in explaining why different density functionals give the same threshold even with substantially different band gaps.

The electronic stopping power of He in Ge is studied within the same framework. Apart from a reasonable agreement with the known experimental results it reproduces the H/He effect observed in jellium models at low electronic densities.

The energy loss to electrons in self-irradiated nickel, a paradigmatic transition metal, is studied. Different core states are explicitly included in the simulations to understand their involvement in the dissipation mechanism. The experimental data are well reproduced in the projectile velocity range of 1.0 – 12.0 atomic units. The core electrons of the projectile are found to open additional dissipation channels as the projectile velocity increases. The systematic, explicit, and flexible inclusion of the core states reveals that almost all of the energy loss is accounted for within this first principles approach. Core electrons as deep as 2s are treated explicitly and are found to be necessary to account for the ion energy loss at relatively high projectile velocities.

The electronic stopping power of self-irradiated W further confirms the role of core states in accounting for the extremely high electronic stopping values of the transition and heavy metals.

Resumen

El paso rápido de iones a través de un sistema de materia condensada constituye un problema cuántico de muchos cuerpos dependiente del tiempo. La complejidad del problema hace que sea extremadamente difícil encontrar una descripción exacta del mismo. Para resolver el problema se han aplicado varios modelos que siendo cuantitativamente precisos proporcionan un grado de éxito variable. En primer lugar, describimos el problema general de la interacción radiación-materia, sus antecedentes, la bibliografía en el campo de la interacción radiación-materia, y campos asociados tales como el estudio del consiguiente daño por radiación. Cuando un ión de movimiento rápido penetra a través de un sólido, pierde energía a través de diferentes mecanismos tales como excitaciones electrónicas en el objetivo, ionización del proyectil, movimiento y desplazamiento de los iones objetivo, emisión de radiación y reacciones químicas o nucleares. Estos mecanismos son extremadamente complicados y la importancia de cada proceso varía dependiendo del material objetivo, del tipo de proyectil, y especialmente del rango de energía. Sin embargo, la pérdida de energía asociada a excitaciones electrónicas, caracterizada como el poder de parada (stopping power) electrónico, es con diferencia el mecanismo más dominante e importante. Los primeros modelos de poder de parada debidos a Bohr, Bethe y Bloch presentaban una validez limitada para iones ligeros en régimen de alta velocidad. El régimen de baja velocidad fue particularmente desafiante ya que en ese rango, los efectos cuánticos se vuelven significantes. Los modelos basados en respuesta lineal del gas de electrones libre, aunque fueron un importante paso adelante, solo tuvieron éxito en la descripción de los fenómenos de parada para iones ligeros e intermedios en metales simples en el régimen de baja velocidad. Dado que en el modelo del gas de electrones se aproxima el material objetivo por un gas de electrones, los efectos del entorno atómico en el poder de parada se ignoran. Además, las características físicas como el band gap en aislantes y semiconductores, la polarización de los electrones del núcleo, y la estructura electrónica detallada del

proyectil son excluidos en dichos modelos limitando su alcance. Se han dado numerosos intentos de modelar teóricamente la interacción de partículas penetrantes cargadas con el material objetivo. Sin embargo, no existe un modelo teórico único, sino diferentes modelos cuyo grado de éxito varía en regímenes específicos, en general caracterizados por el número atómico y velocidad del proyectil.

En los últimos 10 años, la teoría del funcional de la densidad dependiente del tiempo en tiempo real (RT-TDDFT) se ha aplicado con éxito al problema de poder de parada electrónico en metales y aislantes. Sin embargo, la mayoría de los estudios previos basados en RT-TDDFT se han limitado a proyectiles simples (H, He), bajas energías de proyectil y sobre todo elementos objetivo más ligeros con baja parada electrónica. La inclusión de electrones explícitos se ha limitado a electrones de valencia y, en algunos casos, a estados semi-core, mientras que el resto del núcleo permanece congelado y es descrito por un pseudopotencial. En esta tesis hemos abordado la implementación paralela de RT-TDDFT dentro del formalismo de combinación lineal de orbitales atómicos (LCAO). Además, hemos utilizado RT-TDDFT (utilizando tanto el enfoque LCAO como el de ondas planas) para estudiar el problema de parada en un semiconductor representativo con iones simples como H y He en el régimen de baja velocidad así como en metales de transición autoirradiados como Ni y W en un rango completo de velocidades. Con el paso de los años, un área donde la TDDFT se ha aplicado con bastante éxito es la espectroscopía. Se asume una perturbación débil pero espectralmente ancha para evitar efectos no lineales y capturar todas las posibles excitaciones. Una respuesta dependiente del tiempo tal como un dipolo eléctrico se calcula para un tiempo dado, que a su vez se usa para deducir el espectro del sistema. Este formalismo de dominio de frecuencia también se conoce como el enfoque de respuesta lineal. Sin embargo, a pesar de su éxito, este formalismo no se puede aplicar a sistemas sujetos a fuertes perturbaciones. Dichos sistemas incluyen pulsos de láser de alta intensidad o colisiones de partículas rápidas cargadas. El formal-

ismo de dominio de frecuencia tampoco es aplicable cuando se desea seguir la dinámica en tiempo real del sistema, por ejemplo, la interacción radiación-materia y la dinámica del plasmón. El formalismo RT-TDDFT, sin embargo, permite seguir la dinámica de electrones en tiempo real y es capaz de capturar la respuesta en todos los órdenes y los efectos de muchos cuerpos. Además, se puede combinar con la dinámica de iones para realizar dinámicas simultáneas de tipo ion-electrón. Nosotros hemos implementado un algoritmo RT-TDDFT dentro del método Siesta. Sobre la infraestructura básica de SIESTA integramos las Ecuaciones de Kohn-Sham dependientes del tiempo en LCAO utilizando el método de Crank-Nicolson. La integración de Crank-Nicolson y otras operaciones complementarias son realizadas en paralelo, lo que permite la posibilidad de simular sistemas de miles de átomos. La distribución de la matriz en paralelo y su manipulación es manejada por el paquete ScaLAPACK e interconectada con Siesta con el nuevo paquete MatrixSwitch. Las pruebas de escalabilidad en paralelo de nuestra nueva implementación se realizaron en un sistema de 5000 átomos, mostrando un buen escalado hasta 316 procesadores. Hemos utilizado la implementación RT-TDDFT en Siesta junto con qb@ll, un código DFT basado en ondas planas y RT-TDDFT para calcular el poder de parada electrónico. La dependencia del poder de parada electrónico de los parámetros de dirección e impacto, junto con su comportamiento en el umbral de velocidad, se investiga en un semiconductor prototípico de banda prohibida pequeña. Calculamos el poder de parada electrónico de H en Ge, un semiconductor con relativamente baja densidad de empaquetamiento, usando teoría de la densidad del funcional dependiente del tiempo que evoluciona temporalmente. Los cálculos se llevan a cabo en condiciones de canalización con diferentes parámetros de impacto y en diferentes direcciones del cristal para velocidades del proyectil en el rango de 0.05 a 0.6 unidades atómicas. La satisfactoria comparación con los resultados experimentales disponibles apoya los resultados y conclusiones. Encontramos que el poder de parada electrónico calculado es diferente para las

diferentes direcciones cristalinas, sin embargo, la fuerte dependencia del parámetro de impacto se observa solo en una de esas direcciones. El distintio umbral de velocidad observado en los experimentos es bien reproducido, y su relación no trivial con la banda prohibida se ajusta sorprendentemente bien a un argumento de la teoría de la perturbación. Este modelo simple es también exitoso explicando porqué los diferentes funcionales de la densidad dan el mismo umbral incluso con band gaps sustancialmente diferentes. Un cuidadoso análisis de la estructura de bandas del Ge indica que el fenómeno umbral está conectado con el band gap indirecto en direcciones de cristal dadas. Nuestros resultados proporcionan una mayor comprensión del comportamiento umbral de la potencia de parada electrónica en materiales con band gap no nulo.

El poder de parada electrónica de los proyectiles ligeros, como He, generalmente se encuentra que es linealmente proporcional a la velocidad del proyectil en el régimen de baja velocidad. Sin embargo, recientes estudios teóricos y experimentales muestran que esto no siempre es cierto. La estructura de bandas del material objetivo, ocasionalmente junto con los estados de bandas del proyectil, juegan un papel muy importante. El poder de parada electrónico de He en varios materiales (metales y aislantes) ha sido estudiado, tanto teóricamente como experimentalmente. El poder de parada electrónico de He en Al en los experimentos muestra un cambio de pendiente de alrededor de 0.2 unidades atómicas de velocidad. Pero este cambio de pendiente no se reproduce en los cálculos RT-TDDFT, por lo tanto, permanece sin explicación. Un cambio similar de pendiente es medido experimentalmente en Cu y Au, el cual se ha entendido como un efecto de la estructura de bandas dentro de los cálculos RT-TDDFT.

Recientemente, el poder de parada electrónico de He in Ge se ha medido experimentalmente. El experimento muestra un cambio de pendiente alrededor de 0.2 unidades atómicas de velocidad. Nosotros hemos calculado el poder de parada electrónico de He en Ge en el rango de velocidad de 0.05 a 0.6 unidades atómicas. Comparamos el poder de frenado electrónico calculado a lo largo de diferentes direc-

ciones y a diferentes parámetros de impacto. Se encuentra que varía ampliamente entre diferentes canales y dentro de un canal dado para diferentes parámetros de impacto. Muestra una fuerte dependencia de los parámetros de impacto en la dirección [011], que es el canal más ancho. En los otros dos canales, se observa muy poco o nada la dependencia del parámetro de impacto en nuestros cálculos.

El cambio de pendiente observado experimentalmente, alrededor de 0.2 unidades atómicas de velocidad no se observa en nuestros cálculos. Aunque no hay una explicación clara disponible, su aparición en otros sistemas alrededor de la misma velocidad sugiere un cruce de hiper-canalización a más y más trayectorias al azar como una posible causa. A velocidades inferiores a 0.2 unidades atómicas, el proyectil tiene más probabilidades de ser canalizado y muestrear solo trayectorias de grandes parámetros de impacto. Por otra parte, a velocidades relativamente más altas, la canalización es menos probable y el proyectil muestrea todos los parámetros de impacto. La fuerte dependencia del parámetro de impacto revelada en nuestros cálculos significa que trayectorias de bajo parámetro de impacto producirían una mayor potencia de frenado. Otra causa probable del cambio de pendiente de la potencia de frenado electrónica podría haber sido el cruzamiento a la excitación de electrones d en el Ge. Sin embargo, hemos calculado la potencia de parada electrónica con electrones d en Ge tratados explícitamente y no se observa ninguna contribución adicional sobre el rango de velocidades de los proyectiles considerado en este trabajo.

Hemos considerado el problema prototípico de un metal de transición auto-irradiado, níquel (Ni), en el que se dispara un átomo primario (*knock-on atom*) a través del material. Esta es una ocurrencia común en materiales expuestos a la radiación de neutrones. Las aleaciones de Ni son conocidas por su tolerancia a la radiación, estabilidad térmica y sus óptimas propiedades mecánicas, haciendo a estas aleaciones materiales candidatos prometedores para la próxima generación de aplicaciones en energía y aeroespaciales. La presencia

de Ni en las aleaciones estructurales es conocida por desempeñar un papel importante en la mitigación del hinchamiento bajo irradiación.

Hemos estudiado la pérdida de energía de los electrones en el níquel auto-irradiado, un sistema paradigmático, utilizando la teoría del funcional de la densidad dependiente del tiempo en tiempo real. La potencia de parada electrónica en el rango keV/Å se ha calculado de forma exacta. Los diferentes estados de core están explícitamente incluidos en las simulaciones para comprender su participación en el mecanismo de disipación. Los datos experimentales están bien reproducidos en rango de velocidades del proyectil de 1.0 – 12.0 unidades atómicas. Encontramos que los electrones de core del proyectil abren canales adicionales de disipación a medida que la velocidad del proyectil aumenta. La inclusión sistemática, explícita y flexible de los estados de core revela que casi toda la pérdida de energía se puede contabilizar dentro de este enfoque de primeros principios. Electrones de core tan profundos como 2s han sido tratados explícitamente, lo cual se encuentra que es necesario para el cálculo de la pérdida de energía del ión para velocidades del proyectil relativamente altas.

El tungsteno (W) por sus únicas propiedades físicas y químicas es considerado como el material candidato más prometedor para componentes de contención primaria en reactores de fusión nuclear. Hay un creciente interés en estudiar la naturaleza del daño soportado debido a la sostenida exposición a la radiación. Recientes estudios experimentales y de simulaciones atomísticas se han centrado en el daño causado por átomos *knock-on* primarios. Hemos calculado la potencia de parada electrónica de W autoirradiado, un metal pesado paradigmático con poder de frenado de hasta varios miles de eV/Å.

Contents

Acknowledgements	xxi
Abstract	xxiii
Resumen	xxv
1 Introduction	1
1.1 Stopping power	1
1.2 Background	2
1.3 Motivation	6
1.3.1 Radiation damage	6
1.3.2 The electronic stopping power	7
1.4 The electronic stopping power from first principles	9
2 Method	11
2.1 Quantum Many Body Problem	11
2.1.1 Interacting Electrons and Nuclei	12
2.1.2 The Born-Oppenheimer Approximation	13
2.1.3 Classical Nuclei Approximation	14
2.1.4 Interacting Electrons in an External Potential	15
2.2 Density Functional Theory	15
2.2.1 Hohenberg-Kohn Theorems	16
2.2.2 The Kohn-Sham Ansatz	17
2.2.3 Approximations to the Exchange-Correlation Functional	19

2.3	Time Dependent Density Functional Theory	21
2.3.1	Interacting Electrons in a Time-Dependent Potential	21
2.3.2	The Runge-Gross Theorem	22
2.3.3	Time Dependent Kohn-Sham Equations	25
2.3.4	Exchange-Correlation Potential	25
2.4	Computational Methods and Codes	26
2.4.1	Qbox and qb@ll	26
3	RT-TDDFT in SIESTA	27
3.1	Background	27
3.1.1	SIESTA	29
3.2	Formalism	31
3.2.1	The TDKS equation in a fixed basis	31
3.2.2	The TDKS equation in a moving basis	32
3.2.3	Hamiltonian extrapolation	35
3.2.4	Forces	37
3.3	Implementation	39
3.3.1	Parallel matrix manipulation	40
3.3.2	MATRIXSWITCH	42
3.3.3	Scaling	43
4	Electronic stopping power of H in Ge	46
4.1	Introduction	47
4.2	Method	48
4.3	Results and Discussion	53
4.3.1	The velocity threshold	54
4.3.2	Direction and impact parameter dependence	61
5	Electronic stopping power of He in Ge	65
5.1	Motivation	65
5.2	Method	66
5.3	Results and Discussion	67

6	Electronic stopping power of Ni in Ni	71
6.1	Background	71
6.2	Simulation Method	74
6.3	Results and Discussion	75
7	Electronic stopping power of W in W	83
7.1	Motivation	83
7.2	Simulation Details	85
7.3	Results and Discussion	85
8	Conclusions and Outlook	88
8.1	Conclusions	88
8.2	Future Outlook	89
	Appendices	92
A	Work in progress: Low velocity regime	93
A.1	Self-irradiated Ge	93
A.2	Self-irradiated Ni	94
A.3	Self-irradiated W	95

Chapter 1

Introduction

A swift ion shooting through a condensed matter system constitutes a time-dependent quantum many body problem. The obvious complexity of the problem makes it extremely hard to find an exact description, nevertheless, several quantitatively accurate models have been applied to the problem with varying degree of success. In this chapter we outline the general problem of radiation-matter interaction, its background, historical works on radiation matter interaction, its classification into different focus areas, and associated fields such as the study of consequent radiation damage.

1.1 Stopping power

When a fast moving ion penetrates through a solid it loses energy through different channels mainly [1],

- Electronic excitations in the target
- Ionization of the projectile
- Motion and displacements of the target ions
- Emission of radiation
- Chemical or nuclear reactions.

Because these mechanisms are by far complicated, the importance of each process varies depending upon the target material, the type of projectile, and, especially, the energy range. The overall energy loss is described as the stopping power. The stopping power is a quantitative measure of the inelastic interaction between the projectile and the target medium, defined as the energy transferred from the former to the latter per unit path length through the material,

$$\mathcal{S} \triangleq -\frac{dE}{dx}. \quad (1.1)$$

The so-called stopping power, \mathcal{S} , has dimensions of force and acts like a dissipative force which resists the motion of the ion. The fast-moving charged particle dissipates its kinetic energy by collisions with the nuclei and the electrons of the medium. Therefore, it is traditional to divide the energy loss into two components; the energy loss to electronic excitations and the energy loss to the nuclear motion. This convention dates back to the earliest theories of stopping such as Bohr's semiclassical model of stopping power [2]. The energy loss to the host nuclei is called nuclear stopping power and to host electrons is characterized as electronic stopping power,

$$\mathcal{S} = \mathcal{S}_n + \mathcal{S}_e. \quad (1.2)$$

Bohr, quite accurately, understood that the electronic stopping power would be far greater than the nuclear stopping power for the energetic light ions [3]. The contribution of electronic stopping power (\mathcal{S}_e) is dominant in the intermediate to high velocity regime and the nuclear stopping power is only relevant at very low velocities (see Fig. 1.1). The study of electronic stopping power (\mathcal{S}_e) in different realistic systems using first principle methods is the main focus of this thesis.

1.2 Background

The history of using fast moving ions to investigate the structural properties of matter goes back to the early years of modern physics. Soon after the

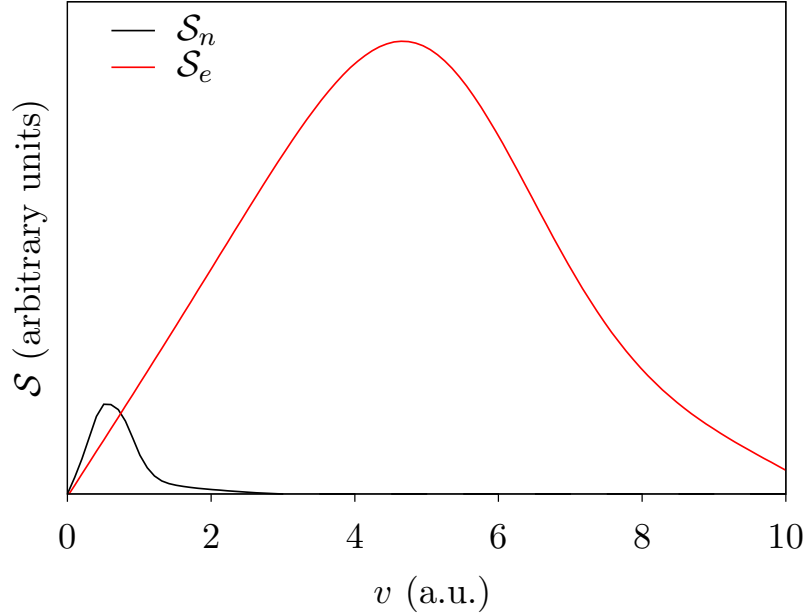


Figure 1.1: Typical dependence of the stopping power on projectile velocity. The graph is just a guide to the eye and is not plotted on scale.

discovery of radioactivity contemporary scientists started wondering how did the emitted energetic particles interact with matter or more precisely lost energy to slow down and eventually stop. A particle energy loss theory was considered the first step towards the development of an atomic model. In 1911 Rutherford performed the famous experiment of showering gold foil with α particles [4]. This experiment, as well as substantiating the nuclear model of atom, gave birth to the field of stopping power. Although it has been around for more than a hundred years, interest in the general area of particle-radiation and matter interaction remains fresh and relevant. Over the years it has both informed our understanding of the basic physics and contributed to the technological advances in medicine [5–7], energy industry [8], aerospace technologies [9], semiconductor and material physics [10].

The study of particle energy loss, essentially, started as an experimental science but quickly became the subject of theoretical studies. The shared

aim has been obtaining a quantitatively accurate description of the problem. A wide range of experimental possibilities have been extensively explored with the development of more sophisticated detectors, particle accelerators and fission reactors. Experimental investigations have been carried out with different types of particles and over a broad range of energies. With the experimental studies the concept of scattering cross section was introduced to statistically describe the interaction of penetrating particles with matter. The swift ions shooting through condensed matter can simultaneously deflect (scatter) or lose energy (stop). The scattering is described by statistical laws underpinning the concept of scattering cross section [11]. Therefore, the stopping must be distinguished from random scattering particularly when the projectile gets channeled in a crystalline solid. The experimental investigations were complemented by attempts to develop more analytical models to describe the energy loss of a charged particle shooting through matter. The initial approaches were mainly based upon the concepts of classical mechanics which occasionally included relativistic effects. Bohr's work [2], in this regard, is one of the earliest and most significant ones. It was, however, limited by its underlying classical assumptions. The first significant step towards the quantum description of collisions and scattering was the first order perturbation theory given by Born in 1926 [12]; which was extended to the theory of stopping of charged particles by Bethe in 1930 [13] and Bloch in 1933 [14]. Bethe-Bloch model was limited by the failure of Born approximation to correctly account for close collisions and the lack of dynamical screening.

Fermi and Teller in 1947 [15], approximating a solid by a degenerate electrons gas, calculated the energy loss per unit path length of charged particle in the velocity range of $v < 1$ atomic unit (a.u. henceforth). They found that energy loss of the charged particle, shooting through the electron gas, is linearly proportional to its velocity. Following the pioneering work of Fermi and Teller, Lindhard in 1954 [16] and Ritchie in 1959 [17], applied a linear response formalism to study the energy loss in simple metals. They modelled simple metals by an electron gas and found linear dependence

between energy loss and the projectile velocity. In 1976, Almladh *et al.* [18], by calculating the static screening of a proton in an electron gas using density functional theory (DFT), pointed out the significant limitations of the linear response treatment. Beginning in 1981, Echenique *et al.* [19–21] have used DFT to calculate the nonlinear response of the electron gas to the perturbation produced by the swift ion. The nonlinear treatment accounted for nonlinear effects such as the presence of bound states and the complex electronic structure of the incoming projectile in the low velocity regime. This pioneering work clearly established the superiority of nonlinear approaches in studying the stopping of slow ions ($v < 1$ a.u.) in solids. An extensive amount of interesting work has been carried out on the problem of stopping within the linear response theory [22–26] and non-linear formalism [27–29]. Relatively recently, the modeling of proton and antiproton stoppings in metals, using jellium clusters as a model of the target, has been extended to intermediate and high projectile velocities using real-time time-dependent density functional (RT-TDDFT) simulations [30–32]. A vast majority of these approaches is limited to an electron gas model of metals and do not take into account important features such as the local inhomogeneity of the electron density, core state excitations and band gaps in case of insulators and semiconductors. These features become increasingly important at low velocities and for heavier projectiles.

The stopping in different realistic systems has been studied using real-time time dependent tight binding (RT-TDTB) approach [1, 33, 34] and linear-response time-dependent density functional theory (LR-TDDFT) [35]. Pruneda *et al.* [36] in 2007 and Hatcher *et al.* [37] in 2008 have successfully applied RT-TDDFT to different realistic systems, bringing the study of ion stopping to a new level a theory that was never achieved before. Since 2007, RT-TDDFT has been successfully used to study many different realistic condensed matter host systems for various projectiles over a wide range of velocities [36–49] where other theoretical approaches had limited success. This is a cursory overview of the past significant works on the problem of stopping

power of swift charged particles. A detailed background on the subject can be found in Refs. [1, 3, 11] and references therein.

1.3 Motivation

1.3.1 Radiation damage

The fast moving charge particles leave the target medium extremely perturbed. The perturbed state of the medium relaxes back to the original state and sometimes to a new state with structural defects. The study of such defects, formally known as ‘radiation damage’, is of great interest from the point of view of nuclear engineering applications [8]. In nuclear reactors both the fast and slow moving neutrons can create fast moving ions in the shielding containment material. The fast moving neutrons knock off ions by direct elastic collisions, while the slow neutrons can produce fast moving ions by triggering nuclear reactions. These effects alter physical properties of the structural materials such as embrittlement, hardening, and swelling. These changes are directly related to the safety, stability, and lifetime of the nuclear reactors. Therefore, the detailed understanding of radiation damage in structural materials is important for nuclear waste processing and storage.

Radiation damage effects are not limited to nuclear reactors but have much wider implications, from biological soft matter [5, 50] to semiconductor electronic devices [9]. In relation to biomedicine research radiations can have both the desired and undesired effects. Uncontrolled radiation swiftly damages the biological soft matter, either burning it or causing mutations in the genetic material which lead to cancer. Sometimes these mutations¹ don’t lead to immediate effects, but ones that appear in the next generation in the form of disabilities. These disabilities are then inherited to several following generations. This makes safety a prime concern when dealing with ionizing radiation. On the other hand radiation is frequently used for diagnosis

¹All kinds of ionizing radiations are a potential (but not the sole) source of mutations and cancer.

and cure, particularly in cancer treatment. This too needs a very careful handling and understanding of the radiation's interaction with the biological soft matter.

Our planet is shielded against a host of cosmic radiations by the geomagnetic field. All spacecrafts traveling beyond this field are exposed to such radiation. This radiation can seriously affect the solar cells, sensors, integrated circuits, and electronic control devices, including computers. In miniaturized digital electronic devices the total charge in the circuit is comparable to that of the of radiation particles [51]. This makes the electronics extremely susceptible to radiation interference. Almost all of solid state electronics is semiconductors-based.

Physical properties of the materials can be engineered to match future technological needs. The presence of defects and impurities in the materials significantly alters their mechanical, electronic and optical properties [52]. Semiconductor materials are an important class of materials in which impurities have been used to greatly optimize their electronic and optical properties. The variation of properties depends on the type of impurity and its distribution and concentration in the matrix. One of the most frequently used methods of adding impurities in semiconductors is ion implantation [10], in which the desired ions are accelerated and showered on the target material to implant. The fashion, in which, these ions are distributed in the material is very important in determining its properties. Therefore, knowing the ion distribution profile and being able to control it is at the heart of semiconductor engineering, and, hence the study of radiation damage in semiconductor materials is of great technological interest.

1.3.2 The electronic stopping power

The characterization of radiation damage by the underlying mechanisms lies at the heart of many future technologies. The experimental study of radiation damage is primarily limited by accessible time and length scales. That is where the simulation of radiation damage in materials is of critical impor-

tance. Historically radiation damage in materials have been simulated using classical molecular dynamics (MD) [53]. In classical MD simulations, atoms are represented by classical potentials overlooking their detailed electronic structure. The effects of electrons on ionic motion are implicitly modelled by thermal reservoirs [54], temperature dependent damping forces [55], and velocity dependent friction forces [56, 57]. In *ab-initio* MD, non-adiabatic dynamic response of electrons is ignored. The MD simulations rely on experimentally measured friction forces due to electrons or in other words electronic stopping power. However, accurate experimental stopping power data is not always available. Other sources of electronic stopping power are semi-empirical models like SRIM [58] which are not always very reliable, in certain limits [40].

The MD approaches, both classical and *ab-initio*, have serious limitations in correctly reproducing the radiation damage effects [59]. The radiation damage events are strongly influenced by the explicit interaction between the swift ions and the electrons [60, 61]. The interaction between the ionic subsystem and the electronic subsystem is complex and multifaceted [62]. The Born-Oppenheimer approximation [63] quickly fails with the increasing velocity of the ions. Beyond the Born-Oppenheimer approximation, the electronic excitations alter the forces acting on ions. Moreover, the electrons have comparatively higher thermal conductivity which can help spread away the heat from relatively hot ions. The electrons can also act as a heat bath in thermal contact with the ionic subsystem. The electronic degrees of freedom play a critically non-trivial role, not only in the initial stages of radiation damage [39, 64] but over the final outcome [59].

This background warrants an accurate description and a clear understanding of the problem of electronic stopping power in solids. Quantitatively correct electronic stopping powers are essential for the MD simulations of radiation damage in solids [65]. A quantum mechanical model of electronic stopping is first step towards non-adiabatic approaches such as the Ehrenfest dynamics (classical ions and quantum electrons) [66, 67] and correlated ion-

electron dynamics (quantum ions and quantum electrons) [68–70] to study the radiation damage. Moreover, a deeper understanding of the stopping mechanism is of interest from the point of view of fundamental physics.

1.4 The electronic stopping power from first principles

The earliest models of stopping power due to Bohr, Bethe and Bloch had a limited validity for light ions in high velocity regime. The low velocity was particularly challenging as the quantum effects became significant. The models based on linear and non-linear response of free electron gas, although an important step forward, were only successful in describing the stopping phenomena for light and intermediate ions in simple metals in the low velocity regime. Since the electron gas models approximate target material by an electron gas, the effects of the atomic environment on the stopping power are ignored. Moreover, the physical features like band gap in insulators and semiconductors, polarization of core electrons, and detailed electronic structure of the projectile are excluded from such models limiting their scope. There have been numerous attempts at theoretically modelling the interaction of penetrating charged particles with the target material; however, there is no unified theoretical model but different models with varying degree of success in specific regimes, generally, characterized by the atomic number and velocity of the projectile.

In the past 10 years, a considerable progress has been made thanks to the advances in electronic structure methods [71–74] and the availability of high throughput computational resources. The application of RT-TDTB to the problem of stopping power in metals has been quite successful [1, 34, 64]. LR-TDDFT has been another successful approach [35]. However, RT-TDDFT offers a much superior description of the problem when it comes to capturing the full effects of band structure [44]. It allows following dynamics in real time capturing non-linear effects to all orders. Therefore, it allows to study the

stopping phenomena in systems which may not be possible with RT-TDTB and LR-TDDFT. Transition metals, insulators, and semiconductors are a general example of such systems.

This pioneering work of using RT-TDDFT to study the electronic stopping power [36, 37, 39, 40] has successfully demonstrated both; its practical applicability and the quantitative superiority. The RT-TDDFT has been applied to metals [40, 44], insulators [47, 75], two-dimensional materials [41] and liquid water [46]. However, most of the previous RT-TDDFT based studies have been limited to simple projectiles (H, He), low projectile energies and mostly lighter host elements with low electronic stopping. The inclusion of explicit electrons has been limited to valence and in some cases semi-core states while the rest of the core is frozen and described by a pseudopotential.

In this thesis we have addressed the parallel implementation of RT-TDDFT within linear combination of atomic orbitals (LCAO) formalism. Moreover, we have used RT-TDDFT (using both the LCAO and planewave approaches) to study the problem of stopping in a representative semiconductor with simple ions such as H and He in the low velocity regime, and self-irradiated transition metals such as Ni and W over a full range of velocities. The application of RT-TDDFT to realistic systems is discussed later in more detail.

Chapter 2

Method

In this chapter we briefly outline the DFT and TDDFT approaches, which are the main methods used to study the problem of electronic stopping power in this thesis.

2.1 Quantum Many Body Problem

The fullest understanding of the structural and functional properties of condensed matter lies in the exact knowledge of the electronic structure of atoms, molecules and compounds. This amounts to solving the Schrödinger equation in quantum mechanics. An exact solution when dealing with a multi-particle system, hits, in Walter Kohn's words, an 'exponential wall' with increasing number of particles. The exponential computational cost of the wavefunction based quantum mechanics limits its applicability to the systems of practical interest. In 1964 Hohenberg and Kohn reformulated quantum mechanics by proposing that all observable properties of a static many-body system can be exactly obtained from its ground-state density [71]. This is what provided the basis for density-functional theory (DFT). In 1984 Runge and Gross [73] proved that the time-dependent density of a time-dependent many-body system can serve as an effective replacement to the time-dependent many-body wavefunction, laying down the foundations for time-dependent

density-functional theory (TDDFT). They further extended the work of Kohn and Sham [72] to model the time-dependent multi-particle system by an auxiliary time-dependent one-particle system, making it practically possible to solve realistic many-body time-dependent problems within condensed matter physics and quantum chemistry.

The central idea of DFT is that any physical property of a system of many interacting electrons can be formalized as a functional of the ground state electron density. The ground state electron density, $\rho_0(\vec{r})$, is a scalar function defined on \mathbb{R}^3 and carries all the information one would want to extract from the many body wave function in the ground state. The many body wave-function is a scalar defined on \mathbb{R}^{3N} , so the DFT reduces the original problem by $3N - 3$ degrees of freedom. Hohenberg and Kohn [71] and Mermin [76] have proved the existence of such functionals which can map physical properties from the ground state electronic density. Kohn and Sham [72] have provided a practical way to make approximate ground state functionals for real systems of many electrons. The Kohn-Sham formalism replaces the interacting problem with an auxiliary independent particle problem with all the many-body effects included in the so-called exchange-correlation functional. DFT has become a basic tool for electronic structure calculations in condensed matter and seen as the most promising approach towards accurate and practical methods in the theory of condensed matter.

2.1.1 Interacting Electrons and Nuclei

For a system of N nuclei and n electrons the non-relativistic Hamiltonian is given by,

$$\begin{aligned}
 H = & - \sum_{I=1}^N \frac{\hbar^2}{2M_I} \nabla_{\vec{R}_I}^2 - \sum_{i=1}^n \frac{\hbar^2}{2m} \nabla_{\vec{r}_i}^2 + \frac{e^2}{2} \sum_{I=1}^N \sum_{J \neq I}^N \frac{Z_I Z_J}{|\vec{R}_I - \vec{R}_J|} \\
 & + \frac{e^2}{2} \sum_{i=1}^n \sum_{j \neq i}^n \frac{1}{|\vec{r}_i - \vec{r}_j|} - e^2 \sum_{I=1}^N \sum_{i=1}^n \frac{Z_I}{|\vec{R}_I - \vec{r}_i|},
 \end{aligned} \tag{2.1}$$

where M_I and Z_I denote the nuclear mass and charge, respectively, m is mass of the electron and e is absolute electronic charge. Solving the many body problem of interacting nuclei and electrons means solving the Schrödinger equation to find the many body wave function, which is intractable in practice for systems with more than a few particles [77].

2.1.2 The Born-Oppenheimer Approximation

Certain approximations are usually employed to reduce the complexity and hence the difficulty in solving the many body problem. The first such approximation is that of Born and Oppenheimer [63] to separate the electronic and nuclear degrees of freedom. The approximation is based on the fact that electrons are very light compared to nuclei (by 3-5 orders of magnitude), and so they instantaneously adjust their positions subject to nuclear motion. This allows to consider nuclei as stationary relative to the fast electronic motion, therefore, we can calculate the ground state electronic structure as a function of the nuclear coordinates first and consider nuclear dynamics separately. In order to decouple the electron-nucleus dynamics we assume a separable form of the total many-body wavefunction,

$$\Psi(\vec{r}^n, \vec{R}^N) = \psi(\vec{r}^n; \vec{R}^N)\chi(\vec{R}^N), \quad (2.2)$$

where $\psi(\vec{r}^n; \vec{R}^N)$ is the electronic wavefunction which only parametrically depends on the nuclear positions and $\chi(\vec{R}^N)$ is the nuclear wavefunction. Applying the many-body Hamiltonian defined in Equation (2.1) on the total many-body wavefunction given by Equation (2.2) and rearranging the terms we get two separate equations one describing the electron dynamics and the other describing the nuclear dynamics. The electronic problem is governed by,

$$H^{el}\psi(\vec{r}^n; \vec{R}^N) = E^{el}(\vec{R}^N)\psi(\vec{r}^n; \vec{R}^N), \quad (2.3)$$

where the electronic Hamiltonian \hat{H}^{el} is given as,

$$H^{el} = -\sum_{i=1}^n \frac{\hbar^2}{2m} \nabla_{r_i}^2 + \frac{e^2}{2} \sum_{i=1}^n \sum_{j \neq i}^n \frac{1}{|\vec{r}_i - \vec{r}_j|} - e^2 \sum_{I=1}^N \sum_{i=1}^n \frac{Z_I}{|\vec{R}_I - \vec{r}_i|}. \quad (2.4)$$

The nuclear dynamics is described by,

$$H^{nuc}\chi(\vec{R}^N) = -i\frac{\partial}{\partial t}\chi(\vec{R}^N), \quad (2.5)$$

where the nuclear Hamiltonian \hat{H}^{nuc} is given as,

$$H^{nuc} = -\sum_{I=1}^N \frac{\hbar^2}{2M_I} \nabla_{R_I}^2 + \frac{e^2}{2} \sum_{I=1}^N \sum_{J \neq I}^N \frac{Z_I Z_J}{|\vec{R}_I - \vec{R}_J|} + E^{el}(\vec{R}^N). \quad (2.6)$$

So the many body interacting electron-nucleus problem decouples into the problem of interacting electrons in an external potential and interacting nuclei in the electronic potential [78].

2.1.3 Classical Nuclei Approximation

Nuclear masses are typically large enough that individual nuclear wave-packets are quite localized. Moreover, the nuclei do not exhibit any significant exchange and correlation effects except at very low temperatures [77]. These two observations allow us to regard nuclei as point-like classical particles. The dynamics of the mean value of the position and momentum operator can be obtained by virtue of Ehrenfest theorem [79],

$$M \frac{d^2 \langle \vec{R}^N \rangle}{dt^2} = -\langle \nabla E^{el}(\vec{R}^N) \rangle. \quad (2.7)$$

This is classical equation of motion defined over the mean value of the position operator. Within the classical nuclei approximation, the mean value of the position can be identified as the classical position of a classical particle,

$$M \frac{d^2 \vec{R}^N(t)}{dt^2} = -\nabla E^{el}(\vec{R}^N). \quad (2.8)$$

The numerical solution of the above equation is called first-principles or *ab-initio* molecular dynamics. In order to obtain $E^{el}(\vec{R}^N)$ we need to solve the time independent electronic problem which is explained in the following sections, and which forms the basis of an electronic structure calculation.

2.1.4 Interacting Electrons in an External Potential

The Hamiltonian for n interacting electrons, as obtained in the previous section, is,

$$H^{el} = - \sum_{i=1}^n \frac{\hbar^2}{2m} \nabla_{r_i}^2 + \frac{e^2}{2} \sum_{i=1}^n \sum_{j \neq i}^n \frac{1}{|\vec{r}_i - \vec{r}_j|} - e^2 \sum_{I=1}^N \sum_{i=1}^n \frac{Z_I}{|\vec{R}_I - \vec{r}_i|}, \quad (2.9)$$

where the last term is external potential $v_{ext}(\vec{r})$ due to the nuclei. The Born-Oppenheimer approximation has allowed us to decouple the electronic degrees of freedom from the nuclear degrees of freedom. Now we have to solve the Schrödinger wave equation for n interacting electrons,

$$H^{el} \psi(\vec{r}^n; \vec{R}^N) = E^{el}(\vec{R}^N) \psi(\vec{r}^n; \vec{R}^N), \quad (2.10)$$

where the electronic many-body wavefunction $\psi(\vec{r}^n; \vec{R}^N)$ depends on the nuclear degrees of freedom \vec{R}^N only parametrically, E^{el} is the corresponding electronic energy. The solution of equation (2.10) is still practically impossible because the electrons interact with each other through the Coulomb two-body interaction. Consequently the presence of an electron in a region of space influences the behavior of all other electrons. Therefore, they cannot be treated independently. In other words, the many-body wave of an interacting electronic system cannot be factored into one-particle wave functions. This is known as a quantum many-body problem.

2.2 Density Functional Theory

Density functional theory (DFT) is one of the most popular first principle methods. DFT is liked for its ability to deal with relatively larger systems, computationally inexpensive and flexible towards its applications to different systems. DFT is, in principle, an exact formulation of the ground state problem for a many-body electronic system. The formulation does not necessitate computation of many-body electronic wave-function, which radically reduces the inherent complexity of the problem.

The Thomas-Fermi model by L. H. Thomas and E. Fermi provided the basis for later development of DFT. Thomas in 1927 and Fermi in 1928 independently proposed that the full electronic density is a fundamental variable of the many-body problem. They gave a recipe for calculating the energy of a many-body electronic system exclusively in terms of the electronic density. The Thomas-Fermi model failed to accurately express the kinetic energy in terms of the electronic density. Moreover, the mean field approximation did not include exchange and correlations effects. Later on P. M. Dirac included exchange effects in the model, but correlation interaction was still missing.

Here we, briefly, revisit the DFT formalism while greatly benefiting from the treatises on DFT by R. Martin [78] and J. Kohanoff [77].

2.2.1 Hohenberg-Kohn Theorems

P. Hohenberg and W. Kohn in 1964 [71] proposed two theorems showing how the ground state energy and other ground state properties can be expressed as a functional of the ground state electron density $\rho(\vec{r})$ only.

Theorem 1. *The external potential $v_{ext}(\vec{r})$, up to a trivial additive constant, is uniquely determined by the ground state electron density $\rho(\vec{r})$.*

Theorem 2. *A universal functional of the density $\rho(\vec{r})$ for the energy $E[\rho]$ can be defined for all electron's systems. Furthermore, for any trial electron density $\tilde{\rho}(\vec{r})$ associated with some external potential $v_{ext}(\vec{r})$, the ground state density $\rho(\vec{r})$ minimizes the functional $E[\tilde{\rho}]$ and the corresponding minimum energy is the ground state energy.*

From equations (2.9) and (2.10) we write,

$$E[\rho] = F[\rho] + \int_{\mathbb{R}^3} v_{ext}(\vec{r})\rho(\vec{r})d^3\vec{r}, \quad (2.11)$$

where,

$$F[\rho] = \langle \psi | - \sum_{i=1}^n \frac{\hbar^2}{2m} \nabla_{r_i}^2 | \psi \rangle + \langle \psi | \frac{e^2}{2} \sum_{i=1}^n \sum_{j \neq i}^n \frac{1}{|\vec{r}_i - \vec{r}_j|} | \psi \rangle, \quad (2.12)$$

or

$$F[\rho] = T_e[\rho] + V_{ee}[\rho]. \quad (2.13)$$

$F[\rho]$ is called Hohenberg-Kohn functional. Both the Hohenberg-Kohn functional and the exact ground state density are unknown. The electron-electron interaction $V_{ee}[\rho]$ can be split into two parts; the classical electrostatic Coulomb repulsion between the electrons and the non-classical exchange and correlation interaction,

$$V_{ee}[\rho] = E_H[\rho] + E_{XC}[\rho]. \quad (2.14)$$

The classical electrostatic interaction between the electrons E_H is also known as Hartree energy, and is defined as,

$$E_H[\rho] = \frac{1}{2} \int_{\mathbb{R}^3} d^3\vec{r} \rho(\vec{r}) V_H(\vec{r}), \quad (2.15)$$

where $V_H(\vec{r})$ is called Hartree potential,

$$V_H(\vec{r}) = \int_{\mathbb{R}^3} d^3\vec{r}' \frac{\rho(\vec{r}')}{|\vec{r} - \vec{r}'|}. \quad (2.16)$$

Therefore, $F[\rho]$ comprises three parts; $T_e[\rho]$, $E_H[\rho]$, and $E_{XC}[\rho]$, of which only $E_H[\rho]$ is known.

2.2.2 The Kohn-Sham Ansatz

Soon after the publication of Hohenberg-Kohn's two theorems, W. Kohn and L. J. Sham in 1965 [72] proposed a practical scheme to find the ground state density. Kohn and Sham proposed to map the full interacting system with the real potential onto a fictitious non-interacting system where electrons are subject to an effective single particle (Kohn-Sham) potential V_{KS} . The Kohn-Sham method gives the same ground state density as the real system but greatly simplifies the calculation. Beginning with independent electron (Kohn-Sham) orbitals, $\{\varphi_i(\vec{r})\}$, the Kohn-Sham kinetic energy $T_{KS}[\rho]$ of a non-interacting system of electrons is defined as¹,

$$T_{KS}[\rho] = \sum_i f_i \langle \varphi_i | -\frac{1}{2} \nabla^2 | \varphi_i \rangle = -\frac{1}{2} \sum_i f_i \int_{\mathbb{R}^3} d^3\vec{r} \varphi_i(\vec{r}) \nabla^2 \varphi_i^*(\vec{r}), \quad (2.17)$$

¹For the sake of simplicity we have taken $\hbar = e = m_e = 1$.

and the electronic charge density as,

$$\rho(\vec{r}) = \sum_i f_i |\varphi_i(\vec{r})|^2, \quad (2.18)$$

where f_i is the occupancy number for each orbital and at $0K$ $f_i = 1$ for states below the Fermi level, $f_i = 0$ for states above the Fermi level, and $\sum_i f_i = n$ (total number of electrons). Now using equations (2.13), (2.14) and (2.17) we can write,

$$F[\rho] = T_{KS}[\rho] + E_H[\rho] + \tilde{E}_{XC}[\rho], \quad (2.19)$$

where,

$$\tilde{E}_{XC}[\rho] = E_{XC}[\rho] + T_e[\rho] - T_{KS}[\rho]. \quad (2.20)$$

The exchange and correlation functional $\tilde{E}_{XC}[\rho]$ is the only unknown in the energy functional.

The second Hohenberg-Kohn theorem is essentially a variational principle for the ground state, therefore, we can minimize $E[\rho]$ with respect to $\{\varphi_i(\vec{r})\}$ subject to the constraint $\langle \varphi_i | \varphi_i \rangle = 1$, while $\rho(\vec{r})$ depends on the Kohn-Sham orbitals. Formally, we require,

$$\frac{\delta \mathcal{L}[\rho(\{\varphi_i\})]}{\delta \varphi_j^*} = 0, \quad (2.21)$$

where,

$$\mathcal{L}[\rho(\{\varphi_i\})] = E[\rho(\{\varphi_i\})] - \sum_i \lambda_i \{\langle \varphi_i | \varphi_i \rangle\} \quad (2.22)$$

and $\{\lambda_i\}$ are Lagrange multipliers. This implies,

$$\begin{aligned} \frac{\delta \mathcal{L}}{\delta \varphi_j^*(\vec{r})} &= \frac{\delta T_{KS}}{\delta \varphi_j^*(\vec{r})} + \frac{\delta \rho(\vec{r})}{\delta \varphi_j^*(\vec{r})} \left[\frac{\delta E_H}{\delta \rho(\vec{r})} + \frac{\delta \tilde{E}_{XC}}{\delta \rho(\vec{r})} + \frac{\delta}{\delta \rho(\vec{r})} \int_{\vec{R}^3} v_{ext}(\vec{r}) \rho(\vec{r}) d^3 \vec{r} \right] \\ &\quad - \lambda_j \varphi_j. \end{aligned} \quad (2.23)$$

The individual functional derivatives, except $\frac{\delta \tilde{E}_{XC}}{\delta \rho(\vec{r})}$, on the right hand side of

the equation (2.23) can be simplified as,

$$\frac{\delta T_{KS}}{\delta \varphi_j^*(\vec{r})} = -\frac{1}{2} f_j \nabla^2 \varphi_j(\vec{r}), \quad (2.24)$$

$$\frac{\delta \rho(\vec{r})}{\delta \varphi_j^*(\vec{r})} = f_j \varphi_j(\vec{r}), \quad (2.25)$$

$$\frac{\delta E_H}{\delta \rho(\vec{r})} = V_H[\rho], \quad (2.26)$$

$$\frac{\delta}{\delta \rho(\vec{r})} \int_{\vec{R}^3} v_{ext}(\vec{r}) \rho(\vec{r}) d^3 \vec{r} = v_{ext}(\vec{r}). \quad (2.27)$$

By substituting equations (2.24), (2.25), (2.26), and (2.27) into equation (2.23) we get the single particle Kohn-Sham equations,

$$\left(-\frac{1}{2} \nabla^2 + V_{KS} \right) \varphi_j(\vec{r}) = \epsilon_j \varphi_j(\vec{r}), \quad (2.28)$$

where V_{KS} (the Kohn-Sham potential) is,

$$V_{KS}[\rho] = v_{ext}(\vec{r}) + V_H[\rho] + V_{XC}[\rho]. \quad (2.29)$$

The Kohn-Sham formulation reduces the n interacting electron problem to n single electron problems and a practical way to calculate the ground state density. The solution of the system of Kohn-Sham equations produces the ground state electron density, and hence, the ground state energy and other ground state properties. It is important to note that the Kohn-Sham potential V_{KS} depends on $\rho[\vec{r}]$ which in turn depends on the Kohn-Sham orbitals $\varphi_i(\vec{r})$. Therefore the Kohn-Sham equations can be solved self-consistently.

The exact form of the exchange-correlation functional is unknown and contains the full complexity of the original problem, nevertheless, approximations to it make electronic structure calculations practically possible.

2.2.3 Approximations to the Exchange-Correlation Functional

The most popular and commonly used approximations to the exchange-correlation functional are the local density approximation (LDA) and the generalized gradient approximation (GGA).

Within LDA, the exchange-correlation functional is constructed based on the assumption that the exchange and correlation energy per electron at any point in the electron gas is the same as that of an electron gas with uniform density. The exchange and correlation energy within LDA is given as;

$$\tilde{E}_{XC}^{LDA} = \int \rho(\vec{r}) \tilde{\epsilon}_{XC}^{LDA} d\vec{r}, \quad (2.30)$$

where $\tilde{\epsilon}_{XC}^{LDA}(\rho)$ is energy density and can be written as a sum of exchange and correlation energy densities,

$$\tilde{\epsilon}_{XC}^{LDA}(\rho) = \tilde{\epsilon}_X^{LDA}[\rho] + \tilde{\epsilon}_C^{LDA}[\rho]. \quad (2.31)$$

The exchange energy density, $\tilde{\epsilon}_X^{LDA}[\rho]$, is obtained using Dirac's expression for homogeneous electron gas;

$$\tilde{\epsilon}_X^{Dirac}(\rho) = -\frac{3}{4} \left(\frac{9}{4\pi^2} \right)^{1/3} \frac{1}{r_s}, \quad (2.32)$$

where $r_s = (\frac{3}{4\pi\rho})^{1/3}$ is the mean electron-electron distance. The correlation energy density, $\tilde{\epsilon}_C^{LDA}[\rho]$, is obtained using a parameterisation of Ceperley and Alder's simulation data [80] by Perdew and Zunger [81],

$$\tilde{\epsilon}_C^{PZ}[\rho] = \begin{cases} A \ln r_s + B + C r_s \ln r_s + D r_s, & r_s \leq 1 \\ \gamma / (1 + \beta_1 \sqrt{r_s} + \beta_2 r_s), & r_s > 1. \end{cases} \quad (2.33)$$

The coefficients for both the spin-polarised and spin-neutral cases have been fitted to the Ceperley and Alder's data. The LDA approximation fails to take into account inhomogeneities in the density and non-local exchange and correlation effects among other physical effects.

GGA is a semi-local extension of LDA, which partially overcomes its shortcomings. Within GGA, the exchange-correlation is constructed as a functional of both the density and the magnitude of the gradient of the density at each point in space.

2.3 Time Dependent Density Functional Theory

In 1984, E. Runge and E. K. U. Gross proposed time-dependent density functional theory formalism for time-dependent quantum problems analogous to DFT reformulation of the time-independent quantum problem [73]. Time-dependent density functional theory (TD-DFT) is essentially an extension of Kohn-Sham DFT. The TD-DFT formalism is based on the Runge-Gross theorem, which is a generalization of the Hohenberg-Kohn theorems. First, we provide a brief outline of the many body time-dependent problem, and then the Runge-Gross theorem and its proof are presented.

2.3.1 Interacting Electrons in a Time-Dependent Potential

A system of n electrons in a time-dependent potential obeys the time-dependent Schrödinger equation,

$$i\frac{\partial}{\partial t}\phi(t) = H(t)\phi(t). \quad (2.34)$$

The Hamiltonian $H(t)$ has the form,

$$H(t) = T + V_{ee} + V_{en} + v(\vec{r}, t). \quad (2.35)$$

The first term is the kinetic energy of the electrons,

$$T = -\frac{1}{2} \sum_{i=1}^n \nabla_{r_i}^2, \quad (2.36)$$

the second term is the Coulomb repulsion between the electrons,

$$V_{ee} = \frac{1}{2} \sum_{i \neq j}^n \frac{1}{|\vec{r}_i - \vec{r}_j|}. \quad (2.37)$$

and the third term is the Coulomb interaction between the electrons and nuclei,

$$V_{en} = - \sum_{I=1}^N \sum_{i=1}^n \frac{Z_I}{|\vec{r}_i - \vec{R}_I(t)|}. \quad (2.38)$$

The time-dependence of the nuclear degrees of freedom \vec{R}^N is used to incorporate the situations in which the nuclei move along classical trajectories. The last term in the time-dependent Hamiltonian, $v(\vec{r}, t)$, is a generic time-dependent potential to account for the physical and chemical phenomena which fall within the premise of time-dependent many body problem, like the interaction of atoms, molecules and solids with an arbitrary time-dependent electric field and the scattering experiments. We will regard the last two terms in the Hamiltonian together as a generic time-dependent external potential $v_{ext}(\vec{r}, t)$ in the forthcoming discussion.

It is impossible to analytically solve the time-dependent Schrödinger wave equation (2.34), therefore we need an alternative formulation of the time-dependent many body quantum problem. An alternative description of the time-independent quantum many-body problem is the DFT which is based on the variational principle for total energy. For the time-dependent many body problem there is no variational principle on the total energy as the total energy is not a conserved quantity. However, there exists a quantum mechanical action, a quantity analogous to the energy in the time-dependent case,

$$\mathcal{A}[\phi] = \int_{t_0}^{t_1} dt \langle \phi(t) | i \frac{\partial}{\partial t} - H(t) | \phi(t) \rangle. \quad (2.39)$$

The many-body wavefunction $\phi(t)$ which makes the action functional stationary is the legitimate solution of the many body time-dependent Schrödinger wave equation. Therefore, the variational principle for the time-dependent many body problem is on the quantum mechanical action.

2.3.2 The Runge-Gross Theorem

The Runge-Gross theorem constitutes the mathematical foundations of TD-DFT. It shows that, like in the DFT formalism, the density can be used as a fundamental variable.

Theorem. *For a many body system starting from a given initial wavefunction, there exists a one-to-one mapping between the potential and the density of the*

system.

The proof of the theorem is not straight forward like that of the Hohenberg-Kohn theorem. Here we, briefly, revisit the proof while an extensive description of the TDDFT formalism, its background and applications are covered in Ref. [82]. We need to prove that if two potentials, $v(\vec{r}, t)$ and $v'(\vec{r}, t)$, differ by more than a purely time-dependent function $f(t)$, they cannot produce the same time-dependent density, $\rho(\vec{r}, t)$; formally,

$$v(\vec{r}, t) \neq v'(\vec{r}, t) + f(t) \implies \rho(\vec{r}, t) \neq \rho'(\vec{r}, t). \quad (2.40)$$

This statement establishes the one-to-one correspondence between the potential and the density. To prove the Runge-Gross theorem we need to prove this statement. We Taylor expand the external potential in time around the initial time t_0 ,

$$v(\vec{r}, t) = \sum_{k=0}^{\infty} c_k(\vec{r})(t - t_0)^k, \quad (2.41)$$

with the expansion coefficients,

$$c_k(\vec{r}) = \frac{1}{k!} \left. \frac{d^k}{dt^k} v(\vec{r}, t) \right|_{t=t_0}. \quad (2.42)$$

We define,

$$u_k(\vec{r}) = \left. \frac{\partial^k}{\partial t^k} [v(\vec{r}, t) - v'(\vec{r}, t)] \right|_{t=t_0} \neq \text{const.}, \quad (2.43)$$

because if the two potentials differ by more than a purely time dependent function, at least one of the coefficients will differ by more than a constant. First we prove that if $v(\vec{r}, t) \neq v'(\vec{r}, t) + f(t)$ then the current densities, \vec{j} and \vec{j}' corresponding to v and v' are also different. The current density is the expectation value of the current density operator,

$$\langle j(\vec{r}, t) \rangle = \langle \phi(t) | j(\vec{r}) | \phi(t) \rangle, \quad (2.44)$$

where

$$j(\vec{r}) = -\frac{1}{2i} \{ [\nabla \phi^\dagger(\vec{r})] \phi(\vec{r}) - \phi^\dagger(\vec{r}) [\nabla \phi(\vec{r})] \}. \quad (2.45)$$

Now we use the Heisenberg equation of motion to get the equations of motion for the current densities,

$$i \frac{d}{dt} j(\vec{r}, t) = \langle \phi(t) | [j(\vec{r}), H(t)] | \phi(t) \rangle, \quad (2.46)$$

$$i \frac{d}{dt} j'(\vec{r}, t) = \langle \phi'(t) | [j'(\vec{r}), H'(t)] | \phi'(t) \rangle. \quad (2.47)$$

Since we begin with the same initial many body state, at $t = t_0$ the wave-functions, densities and current densities have to be equal for both potentials. Taking the difference between equation (2.46) and equation (2.47) at $t = t_0$, after a little algebra, we get,

$$\begin{aligned} i \frac{d}{dt} [j(\vec{r}, t) - j'(\vec{r}, t)]_{t=t_0} &= \langle \phi_0 | [j(\vec{r}), v(\vec{r}, t_0) - v'(\vec{r}, t_0)] | \phi_0 \rangle \\ &= i \rho_0(\vec{r}) \nabla [v(\vec{r}, t_0) - v'(\vec{r}, t_0)] \end{aligned} \quad (2.48)$$

Suppose that equation (2.43) is satisfied for $k = 0$, which means that the two potentials differ at $t = t_0$. This implies that the derivative on the left-hand side of equation (2.48) is non-zero. The two current densities will subsequently differ for $t > t_0$. If k is greater than zero then the $(k + 1)$ st time derivative on the left-hand side of equation (2.48) will be non-zero,

$$\frac{d^{k+1}}{dt^{k+1}} [j(\vec{r}, t) - j'(\vec{r}, t)]_{t=t_0} = \rho_0(\vec{r}) \nabla u_k(\vec{r}), \quad (2.49)$$

which again implies that the two densities will be different at $t > t_0$.

Now we use the equation of continuity to prove that,

$$j \neq j' \implies \rho \neq \rho'. \quad (2.50)$$

We write the equation of continuity for both systems and take the difference to get,

$$\frac{\partial}{\partial t} [\rho(\vec{r}, t) - \rho'(\vec{r}, t)] = -\nabla \cdot [j(\vec{r}, t) - j'(\vec{r}, t)]. \quad (2.51)$$

Here again we would like to have the k th time derivative of the external potential, therefore we take the $(k + 1)$ st time derivative of equation (2.51) at $t = t_0$ and using equation (2.49) we get,

$$\frac{\partial^{k+2}}{\partial t^{k+2}} [\rho(\vec{r}, t) - \rho'(\vec{r}, t)]_{t=t_0} = -\nabla \cdot [\rho_0(\vec{r}) \nabla u_k(\vec{r})]. \quad (2.52)$$

This implies, by virtue of the assumption $u_k(\vec{r}) \neq \text{const.}$, that

$$\nabla \cdot [\rho_0(\vec{r}) \nabla u_k(\vec{r})] \neq 0 \implies \rho \neq \rho'. \quad (2.53)$$

This proves the Runge-Gross theorem.

2.3.3 Time Dependent Kohn-Sham Equations

The Runge-Gross theorem establishes the time-dependent density as a fundamental representation of a many-body time dependent system but it does not outline the way to compute the important physical quantities including the density itself. Again, to avoid the complexity of solving a full many-body time-dependent problem the interacting many-body electronic problem is mapped onto an auxiliary non-interacting single particle (Kohn-Sham) system. The Kohn-Sham equations are reconstructed to include the time-dependence [73, 82],

$$i \frac{\partial}{\partial t} \varphi_i(\vec{r}, t) = \left[-\frac{\nabla^2}{2} + v_{KS}(\vec{r}, t) \right] \varphi_i(\vec{r}, t). \quad (2.54)$$

The time independent Kohn-Sham potential is replaced by a time-dependent Kohn-Sham potential, which is unique by virtue of the Runge-Gross theorem. The density of the interacting system is obtained from the time-dependent Kohn-Sham orbitals,

$$\rho(\vec{r}, t) = \sum_i |\varphi_i(\vec{r}, t)|^2. \quad (2.55)$$

2.3.4 Exchange-Correlation Potential

In traditional DFT the exchange-correlation potential is normally written as the functional derivative of the exchange and correlation energy which follows from the variational principle on the total energy. As we have already mentioned that the total energy is no more a conserved quantity, the exchange-correlation formalism of DFT cannot be extended to TD-DFT. In TD-DFT the exchange-correlation functional is written as the functional derivative of

the exchange-correlation part of the action,

$$v_{XC}(\vec{r}, t) = \left. \frac{\delta \mathcal{A}_{XC}}{\delta \rho(\vec{r}, \tau)} \right|_{\rho(\vec{r}, t)}, \quad (2.56)$$

where τ is so-called Keldish pseudo-time. The exact expression of the exchange-correlation functional is unknown, as in DFT. Therefore we need to approximate it, the first and simplest approximation is the adiabatic local density approximation (ALDA). ALDA in essence is LDA the only difference is that it is evaluated at each time with the density $\rho(\vec{r}, t)$.

2.4 Computational Methods and Codes

The time-dependent Kohn-Sham equation (2.54) being a single particle equation is fairly easy to solve numerically. This is essentially an initial value problem. Once an initial state $\varphi_i(\vec{r}, t_0)$ at time $t = t_0$ is known, the main task is to propagate it to some final state $\varphi_i(\vec{r}, \tau)$ at time $t = \tau$. Generally, the initial state is the ground state of the system, *i.e.*, the solution of the time independent Kohn-Sham equations. We have used the SIESTA [83], Qbox [84, 85], and qb@ll [86] for our calculations. The TDDFT implementation within SIESTA method and code constitutes part of this thesis and its detailed description is deferred to Chapter 3.

2.4.1 Qbox and qb@ll

Qbox, of which qb@ll is a fork, is an open source highly parallel plane-wave DFT code. Standard qb@ll and custom modifications of Qbox have TDDFT flavours within the plane-wave basis formalism.

Detailed implementation and underlying algorithms of these closely related codes are covered in these Refs. [84–86]. The TDDFT implementation solves the time-dependent Kohn-Sham equations (2.54) in real time using different numerical integration algorithms. The Kohn-Sham wavefunctions are expanded in plane-wave basis. Other important features are the provision of periodic boundary conditions and pseudopotential approximation.

Chapter 3

RT-TDDFT in SIESTA

We have implemented a real-time time-dependent density-functional theory algorithm within the SIESTA method. Building on the basic infrastructure of SIESTA we integrate the time-dependent Kohn-Sham equations using the Crank-Nicolson method. Crank-Nicolson integration and other complementary operations are performed in parallel, allowing for the possibility of simulating systems of thousands of atoms. The parallel matrix distribution and manipulation is handled by the SCALAPACK package, and interfaced to SIESTA with the newly-developed MATRIXSWITCH wrapper package. Parallel scalability tests for our new implementation are performed on a system of 5000 atoms, showing a good scaling up to 316 processes.

3.1 Background

In 1964 Hohenberg and Kohn reformulated quantum mechanics by proposing that all observable properties of a static many-body system can be exactly obtained from its ground-state density [71]. This is what provided the basis for density-functional theory (DFT). In 1984 Runge and Gross [73] proved that the time-dependent density of a time-dependent many-body system can serve as an effective replacement to the time-dependent many-body wavefunction, laying down the foundations for time-dependent density-functional theory

(TDDFT). They further extended the work of Kohn and Sham [72] to model the time-dependent multi-particle system by an auxiliary time-dependent one-particle system, making it practically possible to solve realistic many-body time-dependent problems within condensed matter physics and quantum chemistry.

The time dependent Schrödinger wave equation;

$$\hat{H}(t)\psi(t) = i\frac{\partial\psi(t)}{\partial t}, \quad (3.1)$$

when applied to a multi-particle system the computational cost grows exponentially. The exponential computational cost makes it almost impossible to study systems of practical interest. However, within the TDDFT formalism the computational cost grows as N^3 at worst, with N being the number of interacting particles. TDDFT, due to its useful balance between efficiency and accuracy, is increasingly being applied to problems in quantum biology, quantum chemistry, condensed matter physics, material science, and geophysics.

Over the years, one area where TDDFT has been applied quite successfully is spectroscopy. A weak but spectrally-broad external perturbation is assumed to avoid non-linear effects and capture all possible excitations. A time-dependent response such as an electric dipole is calculated for a given time, which in turn is used to deduce the spectrum of the system. This frequency-domain formalism is also known as the linear-response approach. However, as successful as it has been, this formalism cannot be applied to systems subject to strong perturbations. Such systems include high-intensity laser pulses or swift charged particle collisions. The frequency domain formalism is also not applicable when it is desirable to follow the real-time dynamics of the system, e.g., radiation-matter interaction and plasmon dynamics.

The real-time (RT)-TDDFT formalism, however, allows to follow electron dynamics in real time and is capable of capturing the response to all orders and many-body effects. Moreover, it can be combined with ion dynamics to perform simultaneous ion-electron dynamics. The time-dependent Kohn-Sham (TDKS) equation has previously been solved in real time for a number

of uses, e.g., by Yabana and Bertsch [87] to study dipole response in atomic clusters, by Rubio *et al.* [88] to compute the photoabsorption spectra of metal clusters, and by Tsolakidis *et al.* [89] to study optical response in atomic clusters. RT-TDDFT has also been successfully used to study radiation-related non-adiabatic processes in different materials [36, 39, 40, 44–46, 90, 91].

RT-TDDFT has been formally implemented in a number of first-principles based codes such as Qbox [85], qb@ll [86], OCTOPUS [92, 93], and GPAW [94], to name a few. In this manuscript we report a novel parallel implementation of RT-TDDFT in the SIESTA code [83, 95]. SIESTA is a well-established DFT method and code making use of an efficient numerical atomic orbital (NAO) [96] basis set and the pseudopotential approximation [97]. The code is distributed under the GNU General Public License 3 since 2016. Our RT-TDDFT implementation is integrated in the trunk (the main development branch) of the code which is available from Launchpad (<https://launchpad.net/siesta>). It will be included as a new feature in the next production release of SIESTA. We note that a separate serial implementation in an old version of the code has previously been reported [89], and the SIESTA method has also been used elsewhere as a foundation for testing different RT-TDDFT implementations [98, 99].

3.1.1 SIESTA

SIESTA is a suite of computer codes which implement the self-consistent density functional method using norm-conserving pseudopotentials and a linear combination of numerical atomic orbitals (LCAO) as a basis [83, 100, 101]. Instead of doing an all-electron calculation the core electrons are replaced by pseudopotentials and only the valence electrons are treated explicitly. Exchange and correlation functionals are calculated with the local density approximation (LDA) or generalized gradient approximation (GGA). The choice of the LCAO basis set makes SIESTA an $\mathcal{O}(N)$ method, which means the computational cost (computer time and memory) scales linearly with the

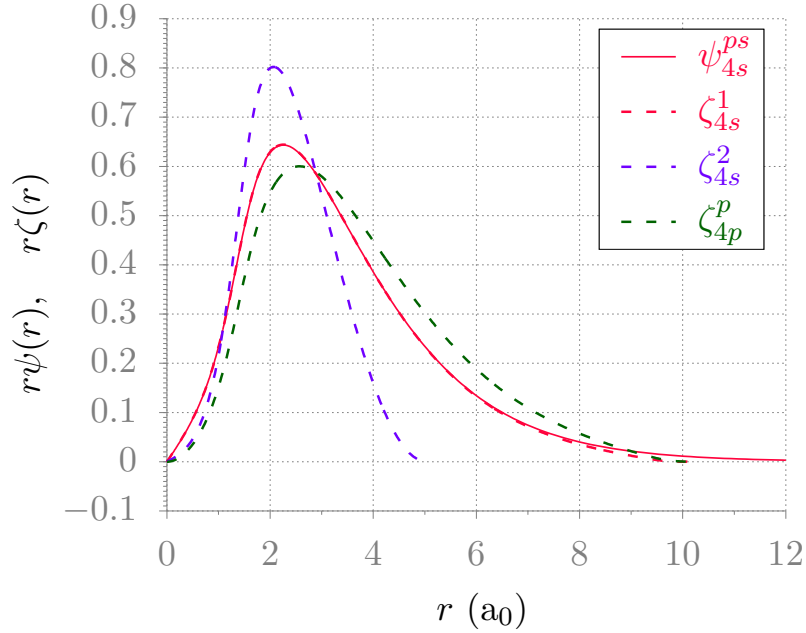


Figure 3.1: The solid line shows pseudo-wavefunction of 4s state of Ni. The dotted lines show POA basis orbitals.

size of the system being simulated [96]. Since SIESTA uses pseudopotentials, pseudo-atomic orbitals (PAO) are used instead of the atomic orbitals. The PAO basis set scheme implemented in SIESTA is described in detail in Refs. [102, 103]. A typical double zeta polarised ($d\zeta + p$) basis set for the 4s orbital of Ni is shown in Fig. 3.1.

SIESTA has been extended beyond ground state electronic structure calculations and *ab-initio* molecular dynamics to include the calculation of phonons, infra-red spectra [95], TDDFT [89], and transport properties [104, 105]. An extensive review of the studies using SIESTA method and code can be found in Ref. [106] As a part of this thesis, we undertook to re-implement and parallelise an earlier and almost obsolete serial implementation of RT-TDDFT in SIESTA.

3.2 Formalism

The non-interacting time-dependent Kohn-Sham system obeys the time-dependent Kohn-Sham (TDKS) equation;

$$i\frac{\partial}{\partial t}\phi(\vec{r}, t) = H^{TDKS}\phi(\vec{r}, t), \quad (3.2)$$

(assuming $\hbar = m_e = e = 1$) such that the time-dependent density of the interacting system can be obtained from the TDKS orbitals, $\phi(\mathbf{r}, t)$;

$$n(\vec{r}, t) = \sum_{\nu} |\phi_{\nu}(\vec{r}, t)|^2. \quad (3.3)$$

The time-dependent Kohn-Sham Hamiltonian, H^{TDKS} , is given as;

$$H^{TDKS} = -\frac{\nabla^2}{2} + V^{TDKS}(\vec{r}, t), \quad (3.4)$$

where,

$$V^{TDKS} = V_{ext}(\vec{r}, t) + \int \frac{\rho(\vec{r}', t)}{|\vec{r} - \vec{r}'|} dr' + V_{XC}[\rho](\vec{r}, t). \quad (3.5)$$

The exchange-correlation potential, V_{XC} , is approximated using the adiabatic local density approximation (ALDA). Solving the TDKS equation (3.2), along with the Hamiltonian evaluation, is the main and most resource-intensive task in RT-TDDFT calculations. SIESTA already has a very efficient mechanism to build the matrix elements of Hamiltonian in parallel; therefore, in this work we have focused on solving the TDKS equation in parallel using the NAO basis set.

3.2.1 The TDKS equation in a fixed basis

The use of NAOs greatly reduces the problem size compared to a plane-wave basis or a real-space grid method. The TDKS orbitals are expanded in a non-orthogonal NAO basis;

$$|\phi(\vec{r}, t)\rangle = \sum_{\mu} C_{\mu}(t) |e_{\mu}(\vec{r})\rangle, \quad (3.6)$$

where

$$\mathbf{S} = \langle e_\mu | e_\nu \rangle \quad (3.7)$$

is the overlap matrix between basis functions. The TDKS equation (3.2), when expressed in the NAO basis in matrix form becomes;

$$i \frac{\partial \mathbf{C}}{\partial t} = \mathbf{S}^{-1} \mathbf{H} \mathbf{C}, \quad (3.8)$$

provided the basis set is fixed (hereafter, the superscript from the TDKS Hamiltonian will be dropped for simplification). This is an initial value problem where the system is in some initial, usually self-consistent ground state at time $t = t_0$. The task at hand is to find a suitable initial state and time-propagate it by numerically integrating equation (3.8). Different numerical integrators, to solve the TDKS equation or similar equations, have been used and tested for stability and efficiency [85, 107, 108].

The Crank-Nicolson propagator [109] has been used successfully to integrate the TDKS equation in local basis frameworks [89]. It preserves orthonormality and, for time-dependent Hamiltonians, time-reversal symmetry. The coefficients at time t can be propagated to time $t + \Delta t$ by forward and backward propagation, respectively, to the so-called mid-point;

$$\mathbf{C}(t + \Delta t/2) = \left[\mathbf{S} - i\mathbf{H}(t) \frac{\Delta t}{2} \right] \mathbf{C}(t), \quad (3.9)$$

$$\mathbf{C}(t + \Delta t/2) = \left[\mathbf{S} + i\mathbf{H}(t + \Delta t) \frac{\Delta t}{2} \right] \mathbf{C}(t + \Delta t). \quad (3.10)$$

Combining equations (3.9) and (3.10) to eliminate the mid-point gives;

$$\mathbf{C}(t + \Delta t) = \left[\mathbf{S} + i\mathbf{H}(t + \Delta t) \frac{\Delta t}{2} \right]^{-1} \left[\mathbf{S} - i\mathbf{H}(t) \frac{\Delta t}{2} \right] \mathbf{C}(t). \quad (3.11)$$

3.2.2 The TDKS equation in a moving basis

The SIESTA method uses a non-orthogonal basis of NAOs centered on atoms. In this scenario each basis function parametrically depends on the nuclear positions;

$$|e_\mu\rangle = |e_\mu(\{\vec{R}\})\rangle. \quad (3.12)$$

Each time the atoms move, the basis functions move with them. For a basis set moving in time, the TDKS equation becomes [74, 110, 111];

$$i\frac{\partial\mathbf{C}}{\partial t} = \mathbf{S}^{-1}(\mathbf{H} - i\mathbf{D})\mathbf{C}, \quad (3.13)$$

where $\mathbf{D} = \langle e_\mu | \frac{\partial}{\partial t} | e_\nu \rangle$. A straightforward generalization of the Crank-Nicolson algorithm, analogous to equation (3.11), can be used to solve equation (3.13), giving;

$$\mathbf{C}(t + \Delta t) = \left[\mathbf{S}(t + \Delta t) + i(\mathbf{H}(t + \Delta t) - i\mathbf{D}) \frac{\Delta t}{2} \right]^{-1} \left[\mathbf{S}(t) - i(\mathbf{H}(t) - i\mathbf{D}) \frac{\Delta t}{2} \right] \mathbf{C}(t). \quad (3.14)$$

However, the propagation is not strictly unitary. An alternative and better algorithm has been very recently proposed by Artacho and O'Regan [111];

$$\mathbf{C}(t + \Delta t) = \mathbf{S}^{-1}(t + \Delta t)\mathbf{S}'(t, t + \Delta t) \left[\mathbf{S}(t) + i\mathbf{H}(t + \Delta t) \frac{\Delta t}{2} \right]^{-1} \left[\mathbf{S}(t) - i\mathbf{H}(t) \frac{\Delta t}{2} \right] \mathbf{C}(t), \quad (3.15)$$

where $\mathbf{S}'(t_0, t_1) = \langle e_\mu(t_0) | e_\nu(t_1) \rangle$. Although the change of basis is captured exactly in this algorithm, the propagation is strictly unitary only in the limit of a complete basis. Furthermore, it requires the inversion of the overlap matrix \mathbf{S} at $t + \Delta t$ and the calculation of the overlap \mathbf{S}' between basis functions at t and $t + \Delta t$, on top of the standard Crank-Nicolson propagation.

Another way of changing basis, based on Löwdin orthonormalization, was proposed by Tomfohr and Sankey [112]. When combined with the Crank-Nicolson algorithm, it becomes;

$$\mathbf{C}(t + \Delta t) = \mathbf{S}^{-\frac{1}{2}}(t + \Delta t)\mathbf{S}^{\frac{1}{2}}(t) \left[\mathbf{S}(t + \Delta t) + i\mathbf{H}(t + \Delta t) \frac{\Delta t}{2} \right]^{-1} \left[\mathbf{S}(t) - i\mathbf{H}(t) \frac{\Delta t}{2} \right] \mathbf{C}(t). \quad (3.16)$$

This algorithm is unitary by construction, and so the preservation of orthonormality is guaranteed. As discussed in detail in Ref. [111], this algorithm is relatively non-rigorous within the framework of a finite evolving basis set. Nevertheless, the discrepancies due to the inconsistencies in its physical significance are negligible when using atomic orbitals as a basis, as further evidenced by its successful use to study time-dependent problems [39, 40, 90].

The algorithm in equation (3.16) can be separated into two procedures. Firstly, the propagation of the wavefunctions in the same basis, using the Crank-Nicolson algorithm and replacing $\mathbf{S}(t + \Delta t)$ by $\mathbf{S}(t)$ for practical convenience;

$$\mathbf{C}_t(t + \Delta t) = \left[\mathbf{S}(t) + i\mathbf{H}(t + \Delta t)\frac{\Delta t}{2} \right]^{-1} \left[\mathbf{S}(t) - i\mathbf{H}(t)\frac{\Delta t}{2} \right] \mathbf{C}_t(t). \quad (3.17)$$

The subscript is used to indicate that the basis remains that from time t . The Crank-Nicolson procedure is then followed by a change of basis operation, if the ionic positions have changed;

$$\mathbf{C}_{t+\Delta t}(t + \Delta t) = \mathbf{S}^{-\frac{1}{2}}(t + \Delta t)\mathbf{S}^{\frac{1}{2}}(t)\mathbf{C}_t(t + \Delta t). \quad (3.18)$$

The practical benefit of separating the two procedures is to perform the change of basis only when necessary; the Crank-Nicolson procedure is the same for both the fixed and moving basis.

As the overlap matrix is positive definite, it is guaranteed to have a unique positive definite square root. The square root and inverse square root are calculated by first computing its eigenvalues and eigenvectors,

$$\mathbf{S} = \mathbf{V}\mathbf{E}\mathbf{V}^\dagger, \quad (3.19)$$

where \mathbf{E} is a diagonal matrix with eigenvalues of \mathbf{S} as its diagonal elements. And \mathbf{V} is a square matrix with eigenvectors of \mathbf{S} as its columns. Then, $\mathbf{S}^{\frac{1}{2}}$ and $\mathbf{S}^{-\frac{1}{2}}$ are calculated as follows;

$$\mathbf{S}^{\frac{1}{2}} = \mathbf{V}\mathbf{E}^{\frac{1}{2}}\mathbf{V}^\dagger, \quad (3.20)$$

$$\mathbf{S}^{-\frac{1}{2}} = \mathbf{V}\mathbf{E}^{-\frac{1}{2}}\mathbf{V}^\dagger, \quad (3.21)$$

where $\mathbf{E}^{\frac{1}{2}}$, $\mathbf{E}^{-\frac{1}{2}}$ are obtained by replacing diagonal elements of \mathbf{E} with their square root and inverse square root, respectively.

3.2.3 Hamiltonian extrapolation

The Crank-Nicolson propagator, equation (3.11) or (3.17), requires *a priori* knowledge of the Hamiltonian $\mathbf{H}(t + \Delta t)$. Different approaches have been adopted to deal with this problem. The most commonly used scheme is to approximate $\mathbf{H}(t + \Delta t)$ by $\mathbf{H}(t)$ [89, 98];

$$\mathbf{C}_t(t + \Delta t) = \left[\mathbf{S}(t) + i\mathbf{H}(t)\frac{\Delta t}{2} \right]^{-1} \left[\mathbf{S}(t) - i\mathbf{H}(t)\frac{\Delta t}{2} \right] \mathbf{C}_t(t). \quad (3.22)$$

The integration using this approximation is only stable at very small time steps, as shown in Figure 3.2. Meng and Kaxiras [98] have introduced an iterative self-consistent operation to improve upon it. Although using a different implicit integrator, Bao *et al.* [113] have introduced a self-consistent predictor-corrector scheme for $\mathbf{H}(t + \Delta t)$. However, any technique employing a proper self-consistent prediction of $\mathbf{H}(t + \Delta t)$ requires the recalculation of the self-consistent functional (SCF) Hamiltonian from the density for every iteration of the self-consistency scheme, which greatly adds to the computational cost.

We have instead implemented a simple heuristic mid-point extrapolation scheme which avoids the recalculation of the SCF Hamiltonian and the need for multiple iterations. The extrapolation requires the current Hamiltonian, $\mathbf{H}(t)$, and the one of the immediate past step, $\mathbf{H}(t - \Delta t)$;

$$\tilde{\mathbf{H}}\left(t + \frac{\Delta t}{2}\right) = \mathbf{H}(t) + \frac{1}{2}[\mathbf{H}(t) - \mathbf{H}(t - \Delta t)]. \quad (3.23)$$

When the extrapolated Hamiltonian is used, the Crank-Nicolson algorithm

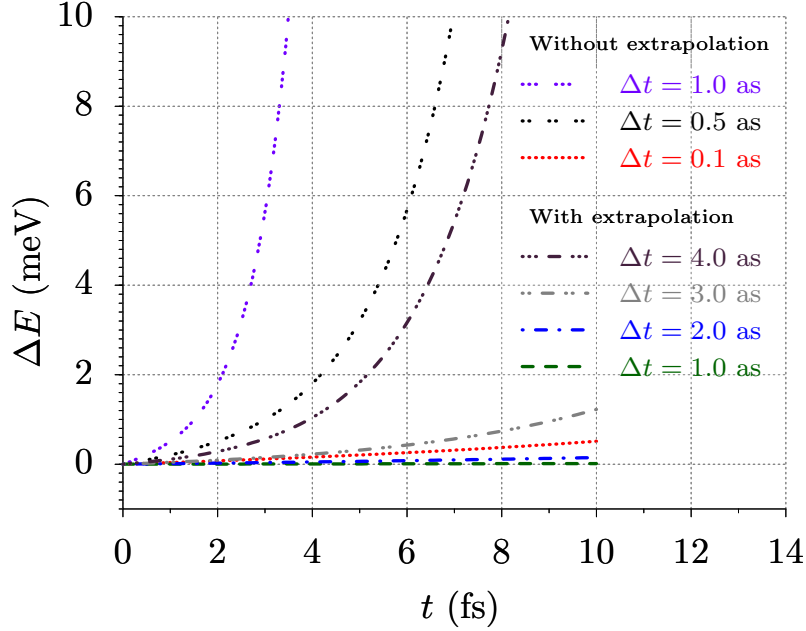


Figure 3.2: The stability and accuracy of different Crank-Nicolson algorithms are compared. The change in the Kohn-Sham energy of a water molecule initially polarized by an electric field and then evolved in time is plotted as a function of time. The dotted lines show the results using the algorithm given by equation (3.22) with different time steps. The dashed-dotted lines show the results using the algorithm given by equation (3.24), also with different time steps.

becomes;

$$\mathbf{C}_t(t + \Delta t) = \left[\mathbf{S}(t) + i\tilde{\mathbf{H}} \left(t + \frac{\Delta t}{2} \right) \frac{\Delta t}{2} \right]^{-1} \left[\mathbf{S}(t) - i\tilde{\mathbf{H}} \left(t + \frac{\Delta t}{2} \right) \frac{\Delta t}{2} \right] \mathbf{C}_t(t). \quad (3.24)$$

It is important to note that the self-consistent Hamiltonian is evaluated only at $t - \Delta t$, t , and $t + \Delta t$.

The stability and accuracy of the algorithms with no extrapolation, given by equation (3.22), and with extrapolation, given by equation (3.24), are compared in Figure 3.2. A water molecule is placed in an electric field of

0.3 V/Å to calculate the self-consistent initial state. Subsequently, the electric field is removed and the the self-consistent ground state is evolved in time using different time steps. The atomic positions of the molecule are fixed. The change in the Kohn-Sham energy of the molecule is plotted as a function of time.

The Hamiltonian extrapolation scheme not only improves stability but allows much larger time steps to be used, at very small additional computational cost. For example, a time step of $\Delta t = 2.0$ attosecond (as) with extrapolation has a smaller drift than a much smaller time step of $\Delta t = 0.1$ as without extrapolation, as shown in the figure. Schleife *et al.* [85], using a fourth-order Runge-Kutta algorithm to solve the TDKS equation in a plane-wave basis, have reported an energy drift of 23 meV/fs when simulating a 64-atom system with a time step of $\Delta t = 0.691$ as. Instead, the energy drift in our example (albeit for a smaller system) is ≤ 1 meV/fs with $\Delta t = 2.0$ as and the extrapolation scheme.

3.2.4 Forces

The TDKS equation of motion describing electron dynamics within RT-TDDFT changes when working in a local basis. Similarly, while performing molecular dynamics or Ehrenfest dynamics in a local basis, there are additional terms involving derivatives of the basis functions that appear in the definition of the forces [74, 110]. This complicates the computation of classical trajectories for the ions. Instead, a plane-wave approach does not have this problem [85, 86].

The accurate computation of forces in conjunction with RT-TDDFT is beyond the scope of this implementation. Nevertheless, it is still possible to address situations in which the forces are negligible or the simulation time-scale is such that there is not enough time for the ions to move significantly. This can be achieved by muting the forces and allowing the ions to move at constant velocities, or following predefined trajectories. This approach has been successfully applied to the problem of electronic stopping power (ESP)

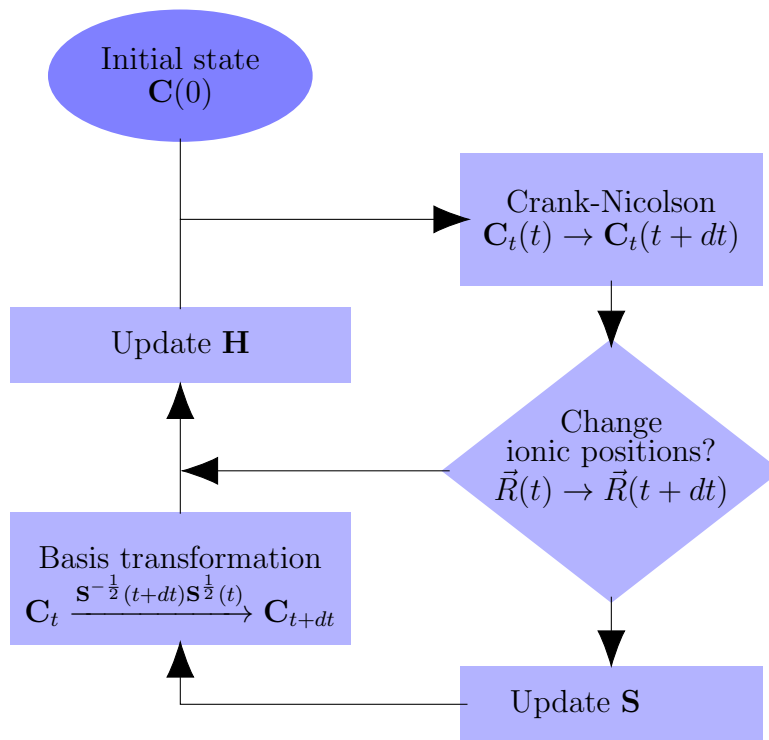


Figure 3.3: Schematic representation of the overall algorithm. The notation is explained in the text.

in several different materials [39, 40, 75, 90], including the example presented in this work. The total simulation time for an ESP calculation is, generally, in the range of femtoseconds, allowing for the projectile ion to move at a constant velocity, while the ions of the host material are fixed.

3.3 Implementation

We have implemented two algorithms to perform the numerical integration of the TDKS equation (3.2). The goal is to numerically perform these operations in a parallel manner to exploit high performance computer (HPC) resources making possible simulation of systems ranging up to thousands of atoms. Since it is an initial value problem, a self-consistent initial state of the system is calculated using a standard DFT method. This self-consistent initial state can be the ground state of system, although not necessarily. The self-consistent Kohn-Sham wavefunction of a molecule initially placed in an electric field is an example of such an initial state; the electric field can be removed to allow the system to evolve in time [89].

A schematic description of the algorithm is given in Fig. 3.3. The system is prepared in some initial state. The coefficients of the basis functions are evolved in time using the Crank-Nicolson algorithm. Depending on whether the atomic positions have changed or not, the overlap matrix and the self-consistent Hamiltonian are computed. The change of basis operation, since it involves the overlap matrix at t and $t + dt$, is applied after the Crank-Nicolson procedure and updating the ionic positions. The Crank-Nicolson step gives the coefficients at the next time step but in the same basis. Finally, the change of basis operator is applied to complete the step. Calculations with a k-point grid in the Brillouin zone are optionally possible using the sampling schemes already available in SIESTA.

in the system (ignoring spin).

The computation of the overlap matrix and Hamiltonian is handled by pre-existing SIESTA routines, which are already parallelized and well-optimized for HPC environments [114, 115]. Our aims for the implementation of the new RT-TDDFT routines were to keep the code clear and physically transparent while ensuring a high level of performance. In order to do so we have employed a new package called MATRIXSWITCH, which abstracts the details of the storage and manipulation of the matrices, and allows for conversions between different storage formats.

Conversion between storage formats is an important consideration here. The native matrix storage format employed by SIESTA is a compressed sparse column (CSC) scheme with a one-dimensional block-cyclic distribution (1D-BCD) over MPI processes. An example of such a distribution is shown in Table 3.1. The combination of the sparse storage and the distribution over processes ensures that memory usage per node on an HPC system stays constant with a soft scaling of the problem (the number of nodes is increased proportionally with the size of the system being simulated). Furthermore, the choice of a 1D distribution is optimal for building the matrices and many physical post-processing operations, as each column represents a basis orbital, and neighboring columns give orbitals on the same atomic site. The use of a block-cyclic distribution, instead, is due to its compatibility with BLACS [116] and the SCALAPACK package [117]. This is important because it has been found that in many practical examples, even for large systems of thousands of atoms, the use of dense matrices for matrix operations gives a superior performance and good scalability and stability. The matrices can therefore be temporarily converted from sparse to dense using the same parallel distribution; this is a very efficient operation, since no MPI communication is necessary.

In the case of our RT-TDDFT implementation, the use of dense matrices is additionally desirable to avoid spurious effects from having to impose a range for truncating the inverse matrix and confining the wavefunctions during

propagation. We therefore convert the overlap matrix and Hamiltonian as described above, and carry out equations (3.18) and (3.24) in parallel using SCALAPACK routines, interfaced through MATRIXSWITCH.

It should be noted that a two-dimensional (2D) BCD is known to be more efficient in terms of parallel scaling [115]. The conversion from 1D to 2D does however carry a heavier cost, as MPI communication is inevitable. The overall benefit of doing so will be investigated in future.

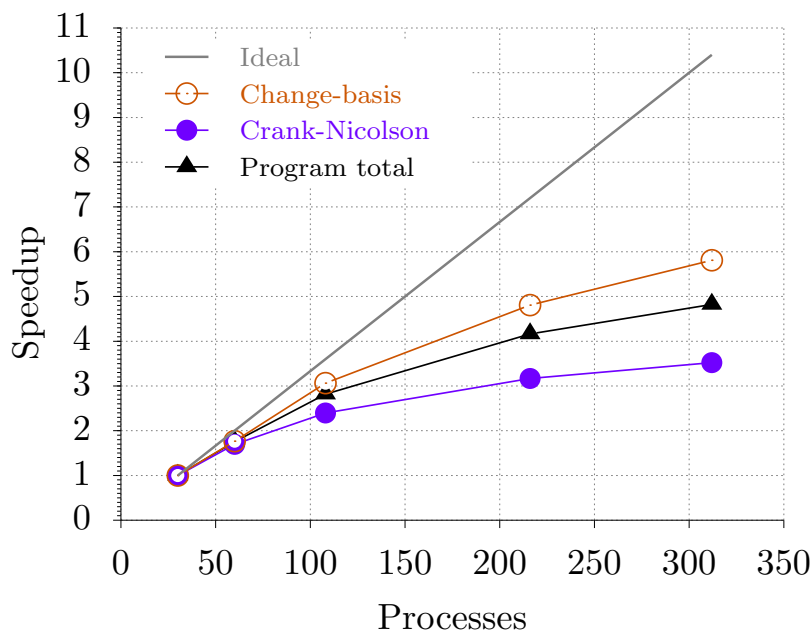


Figure 3.4: A test of scaling efficiency for the RT-TDDFT implementation using a system of 5000 Ge + 1 He atoms. The solid line shows the ideal speedup using a baseline of 30 processes. The total speedup and the two main components of the RT-TDDFT algorithm are shown.

3.3.2 MATRIXSWITCH

MATRIXSWITCH is a software library written in modern Fortran and released under the BSD 2-Clause license. It was developed by Fabiano Corsetti under the Electronic Structure Library initiative (ESL, <http://esl.cecam.org>). Docu-

mentation is maintained on the ESL website (<http://esl.cecam.org/MatrixSwitch>), and the code is available from the E-CAM software repository (<https://www.ecam2020.eu>).

The aim of the package is to act as an intermediary layer between high-level routines for physics-related algorithms and low-level routines dealing with matrix storage and manipulation, allowing the high-level routines to be written in a way which is close to the mathematical notation used in the description of many algorithms while also enabling them to switch seamlessly between different matrix storage formats and implementations of the matrix operations. MATRIXSWITCH is currently being used in parts of SIESTA and in the main interface layer of the recently released ELSI package [118], as well as smaller codes used for individual research projects [119].

3.3.3 Scaling

The parallel efficiency of our implementation is chiefly determined by that of the underlying SCALAPACK drivers. The inversion of the matrix,

$$\left[\mathbf{S}(t) + i\tilde{\mathbf{H}}(t + \Delta t/2) \frac{\Delta t}{2} \right], \quad (3.25)$$

is obtained using LU factorization. Matrix inversion is known to scale poorly with system size. The algorithms that avoid this operation, such as the fourth-order Runge-Kutta scheme, have other overheads such as multiple evaluations of the Hamiltonian [85]. Nevertheless, investigation in this direction is the subject of ongoing work. For the diagonalization of the overlap matrix we have implemented the option of using either a standard diagonalization approach (tridiagonal reduction followed by the implicit QR algorithm) or a divide-and-conquer algorithm as described in Ref.[120]. The latter is known to scale better with system size.

We have tested the scaling efficiency of our implementation using a system of 5000 Ge + 1 He atoms described with a single-zeta polarized ($s\zeta - p$) basis set. The speedup, as shown in Figure 3.4, is defined relative to the time taken on 30 processes for the same simulation. The speedup of the

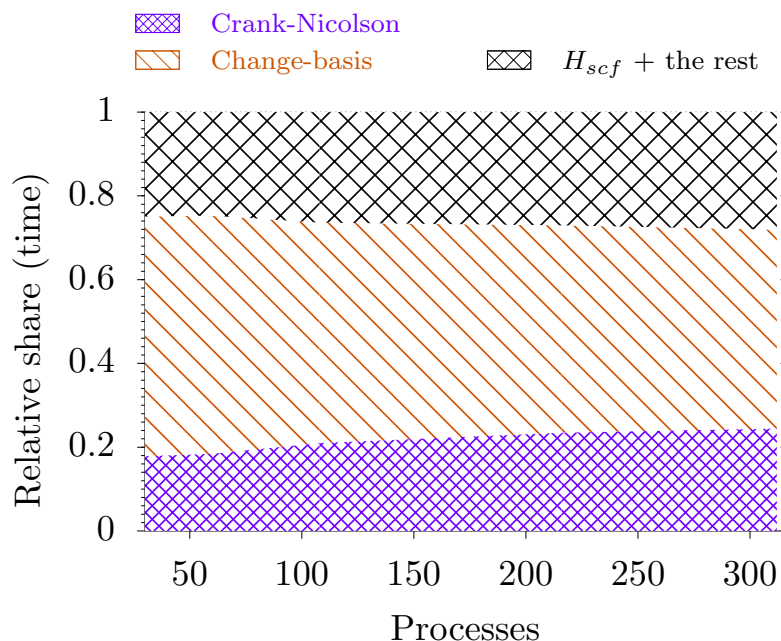


Figure 3.5: The relative share of the total running time for the Crank-Nicolson algorithm, the change of basis operation, and the rest of the program operations (including the building of the SCF Hamiltonian).

overall program reaches almost 50% of the ideal efficiency using 316 processes. The change of basis operation, which involves matrix-matrix multiplication and the diagonalization of the overlap matrix using the divide-and-conquer algorithm, scales better than the overall average; it reaches up to 60% of the ideal efficiency using 316 processes. Instead, as expected the Crank-Nicolson procedure scales worse than the average, reaching only 35% of the ideal efficiency. This is because the most expensive operation, the matrix inversion, determines its scaling.

Figure 3.5 shows the relative share in the total running time of the three main procedures involved: the Crank-Nicolson algorithm, the change of basis, and the calculation of the SCF Hamiltonian plus other minor procedures such as building the density matrix. The Crank-Nicolson algorithm takes about 18% of the total time on 30 processes, which increases to 25% on 316 processes.

Instead, the change of basis procedure take about 38% of the total time on 30 processes, which decreases as the parallelization increases, reflecting its better scaling properties. Nevertheless, it is important to note that the change of basis is the most expensive operation on all number of processes, giving an idea of the extra computational cost involved in performing a RT-TDDFT simulation with a changing basis rather than a fixed one.

Chapter 4

Electronic stopping power of H in Ge: a narrow band gap semiconductor

The direction and impact parameter dependence of electronic stopping power, along with its velocity threshold behavior, is investigated in a prototypical small band gap semiconductor. We calculate the electronic stopping power of H in Ge, a semiconductor with relatively low packing density, using time-evolving time-dependent density-functional theory. The calculations are carried out in channeling conditions with different impact parameters and in different crystal directions, for projectile velocities ranging from 0.05 to 0.6 atomic units. The satisfactory comparison with available experiments supports the results and conclusions beyond experimental reach. The calculated electronic stopping power is found to be different in different crystal directions; however, strong impact parameter dependence is observed only in one of these directions. The distinct velocity threshold observed in experiments is well reproduced, and its non-trivial relation with the band gap follows a perturbation theory argument surprisingly well. This simple model is also successful in explaining why different density functionals give the same threshold even with substantially different band gaps.

4.1 Introduction

There is a growing interest in modeling the stopping power of ions with velocities between 0.1-1 a.u. [121]. In this regime the electronic stopping power (ESP) is generally dominant; however, at lower velocities the contribution from nuclear collisions also becomes sizable [122]. Relatively recently, TD-DFT based first principles calculations of ESP [36, 39, 40, 75] have been performed for insulators and noble metals to explain some interesting effects observed experimentally [123–126] which do not fit the known theoretical models [21, 34]. These TD-DFT based calculations have successfully reproduced the expected threshold behavior in wide band gap insulators, and the role of d electrons in the non-linear behavior found in gold. In contrast, there has not been much work done on semiconductors, except for a study [37] which investigated oscillations in the ESP by varying the atomic number Z . However, no systematic velocity-dependent investigation has been attempted at this level of theory. Recent experiments show a possible small velocity threshold for protons in bulk Ge, a system with very small band gap [127]. The band gap of Ge is almost 20 times smaller than that of LiF while the observed threshold velocity in Ge is only 2 to 3 times smaller. Very little is known about the velocity threshold in small band gap materials.

Experimentally it is almost impossible to measure directly the ESP at velocities $\lesssim 0.2$ a.u., as usually the total stopping power $S = S_n + S_e$ of the medium is measured. The ESP can then be extracted from the measured spectrum using different models [58, 128]. However, a quantitative knowledge of all possible mechanisms contributing to the total stopping power is necessary to extract the electronic component properly. At velocities not much higher than 0.1 a.u. it becomes rather difficult to disentangle the two contributions [129]. However, in simulations it is possible to directly access the ESP using TD-DFT based non-adiabatic electron dynamics simulations. In such simulations the projectile is directed along a crystal direction, where it does not get too close to any of the target nuclei. The nuclear contribution to the stopping power, therefore, is negligibly small and can even be completely

suppressed by constraining the host atoms to be immobile.

In this study we have investigated the ESP of H in Ge. A small band gap and relatively low packing density makes Ge particularly interesting for the investigation of the threshold behavior which has been observed in wide band gap insulators [75, 126]. The simulations have been carried out using an equivalent method to Refs. [40, 75]. Furthermore, we have systematically studied the direction and impact parameter dependence of the ESP, for which very little is known. The accuracy offered by this method, as verified in the satisfactory comparison to experiments below, allows us to explore these aspects explicitly.

4.2 Method

The calculations are carried out using RT-TDDFT implementation in SIESTA program and method [83, 95] as explained in Chapter 3. The ground state of the system is calculated with the projectile placed at its initial position. The ground state Kohn-Sham (KS) orbitals serve as initial states. Once the ground state of the system is known, the projectile is given an initial velocity and the KS orbitals are propagated according to the time-dependent KS equation using the Crank-Nicolson method with a time step of 1 as. The forces on the nuclei are muted so that energy is transferred only through inelastic scattering to the electrons. In any case, the projectile velocities are fast enough to leave little or no time for the nuclei to respond. The projectile velocity itself is similarly kept constant by neglecting forces on the projectile. This allows for a simple extraction of the ESP at a well-defined velocity for each simulation, which is the main aim of our study. The change in velocity, if considered, can be expected to be of no more than 10%.

The total energy of the electronic subsystem is recorded as a function of the projectile displacement for a given velocity, as shown by the example in Figure 4.2 (dotted black line). The peaks reflect the crystal periodicity. We then adiabatically move the projectile along the same trajectory (i.e.,

using standard ground-state DFT) and calculate a corresponding adiabatic energy profile (solid red line). Subtracting the adiabatic total electronic energy $E_a(z)$ from the time-dependent total electronic energy $E_{td}(z)$ gives an oscillation-free profile of the non-adiabatic energy transfer to the electronic subsystem along the trajectory:

$$\Delta E_{na}(z) = E_{td}(z) - E_a(z); \quad (4.1)$$

$\Delta E_{na}(z)$ is therefore the non-adiabatic contribution shown by the dashed blue line, from which the gradient can easily be extracted by a linear fit; this gives our value for the ESP at that velocity.

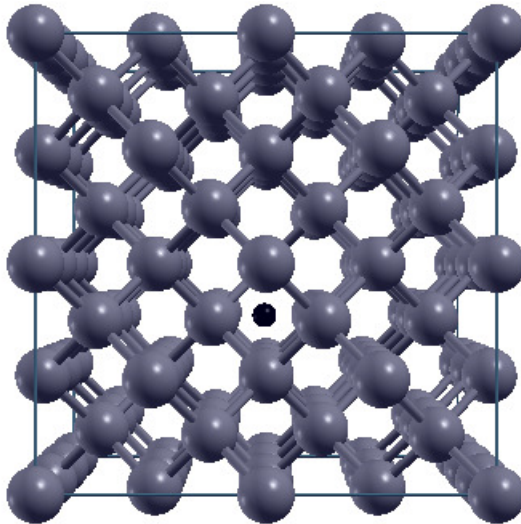


Figure 4.1: Ge supercell in the [001] direction with H in a channel.

The Kohn-Sham orbitals were expanded in a basis of numerical atomic orbitals of finite extent [96, 130]. A double- ζ polarized (DZP) basis set was used to represent the valence electrons of the projectile and the host material, while the core electrons were replaced by norm conserving Troullier-Martins pseudopotentials [131], factorized in the separable Kleinman-Bylander (KB) form [132]. Pruneda and Artacho [133] have studied the validity of pseudopotentials for short range interatomic interactions, showing how the

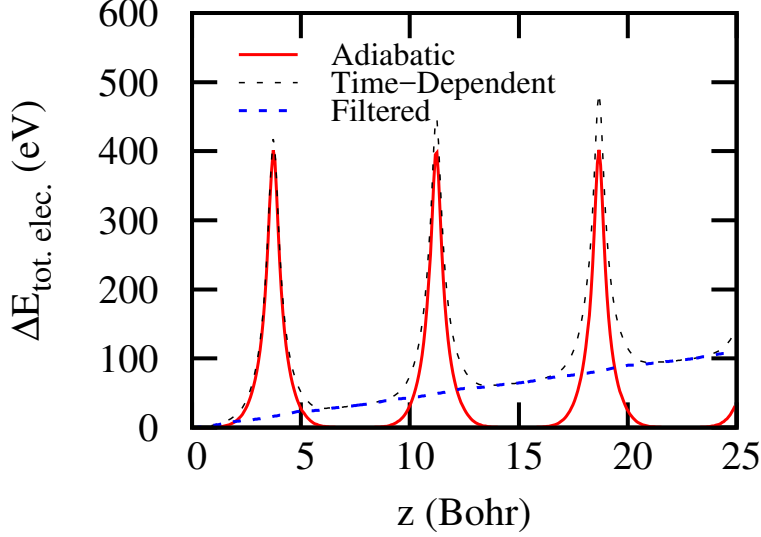


Figure 4.2: The total energy of the electronic subsystem as a function of the projectile displacement is shown by the dotted (black) line (for a projectile traveling along the [011] direction of Ge with a small impact parameter at a velocity of 0.6 a.u.). The solid (red) line shows the adiabatic total energy of the electronic subsystem along the same trajectory. The dashed (blue) line shows the difference between the two, i.e., the non-adiabatic energy contribution.

inclusion of core electrons in the valence configuration mitigates the errors from this approximation. Therefore the effect of the Ge pseudopotential was checked by introducing the core ($3d$) electrons into the valence shell, which might be important for the lowest impact parameter trajectories passing very close to some of the Ge ions in the supercell. We did not find a significant error in the ESP for any of the impact parameters shown in our results. Considering the point expected to have the largest pseudopotential error (the lowest impact parameter and the highest projectile velocity), the semicore calculations give an increase of $0.35 \text{ eV}/\text{\AA}$ (an error of 4%). The parameters needed for the generation of the basis set used in this work, according to the

procedure explained in Ref. [96], are given in Table 4.1. The parameters need to generate the pseudopotentials are listed in Table 4.2. The sampling of the real-space grid, for representing the electronic density and basis functions for the calculation of some terms of the Hamiltonian matrix [95], was chosen to correspond to an energy cutoff of 200 Ry.

Table 4.1: Cutoff radii $r(\zeta_1)$, $r(\zeta_2)$ of first and second zeta functions respectively, and the soft-confinement potential’s internal radius r_i are in Bohr; the soft-confinement potential pre-factor V_0 is in Ry.

Species	n	l	V_0	r_i	$r(\zeta_1)$	$r(\zeta_2)$
Ge	3	2	50	6	6.50	
	4	0	50	6	6.50	5.00
	4	1	50	6	6.50	4.50
	4	2	50	6	6.50	
H	1	0	50	6	7.00	2.90
	2	1	100	0	6.00	

Table 4.2: Matching radii for each of the angular momentum channels of Ge and H. All lengths are in Bohr.

Species	s	p	d	f
Ge($4s^24p^2$)	2.06	2.85	2.58	2.58
Ge($3d^{10}4s^24p^2$)	1.98	1.98	1.49	1.98
H($1s^1$)	1.25	1.25	1.25	1.25

A 96-atom supercell (Figure 4.1) constructed by $2 \times 2 \times 3$ conventional cubic cells of Ge was used. We have checked the convergence of the ESP with respect to supercell size using a larger 144-atom supercell at a projectile

velocity of 0.6 a.u., finding an increase of 0.29 eV/Å (an error of 4%). A k -point mesh of $4 \times 4 \times 3$ points generated with the Monkhorst-Pack method [134] corresponding to an effective cutoff length of 22.36 Å [135] was used after testing its convergence (see Fig. 4.3). The exchange and correlation functional was evaluated using the local density approximation (LDA) in the Ceperley-Alder form [80].

We used the theoretical lattice constant, which was found to be 5.59 Å, compared to an experimental value of 5.66 Å. This underestimation of $\sim 1\%$ is typical for the LDA. An indirect band gap of 0.70 eV was found for bulk Ge, compared with an experimental value of 0.74 eV (at 0 K). However, it is important to note that this good agreement is fortuitous, as DFT with LDA generally either underestimates the band gap or does not produce one at all. Pseudopotential can be one of the sources of cancellation of errors [136] along with a smaller lattice parameter which tend to open the band gap. Lee *et al.* [137], using a plane-wave method, have reported an indirect band gap of 0.41 eV. Much larger band gap, up to 0.81 eV [138], have been reported depending upon the details of the calculation. The dependence on the density functional was checked by repeating the calculations for the Perdew-Burke-Ernzerhof (PBE) functional [139], for which the theoretical lattice constant was found to be 5.78 Å with a direct band gap of 0.33 eV.

In order to check the convergence of our basis in SIESTA, we have also computed the band structure with the plane-wave DFT code ABINIT [140], making use of exactly the same pseudopotential including the same choice of local potential and KB projectors, and a high kinetic energy cutoff of 95 Ry for the basis. The agreement for the valence and low-lying conduction bands is excellent, although we find a slightly smaller band gap of 0.58 eV with the plane-wave calculation (see Fig. 4.4).

The projectile trajectories are chosen along the [001], [011], and [111] directions. A sectional view of the simulation box orthogonal to the [001] channel is shown in Figure 4.1. Different representative impact parameters are considered within the [001], [011], and [111] channels. The projectile

velocities range from 0.05 a.u. to 0.6 a.u. for each trajectory.

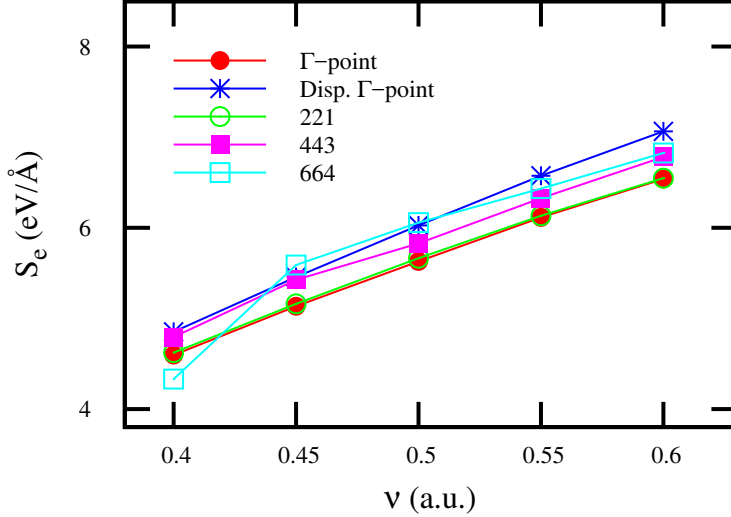


Figure 4.3: The electronic stopping power calculations in the [111] channel with different k -point sampling. The red solid circle and blue star data points indicate a Γ -point and displaced Γ -point calculations, respectively. The empty green circle, solid magenta rectangle, and empty cyan rectangles represent the calculations with $2 \times 2 \times 1$, $4 \times 4 \times 3$, $6 \times 6 \times 4$ k -points generated using Monkhorst-Pack method [134], respectively.

4.3 Results and Discussion

In an experiment with a polycrystalline sample the projectile gets channeled along different crystal directions. We have therefore taken into account the direction and impact parameter dependence. We have computed the ESP along three different channels. The calculated ESP is compared with experimentally measured values by Roth *et al.* [127] in Figure 4.5.

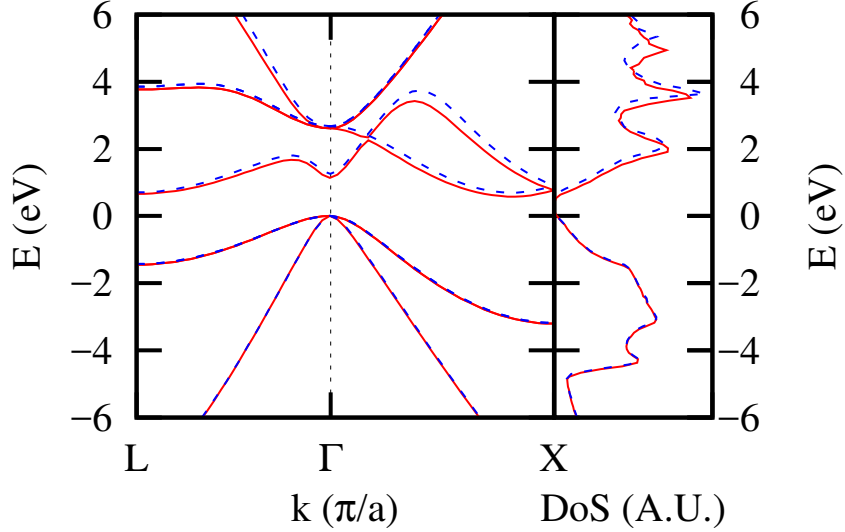


Figure 4.4: The band structure and density of states of bulk Ge calculated using SIESTA (LCAO) and ABINIT (Plane Waves) is compared. The same pseudopotential (and its local and non-local components) is used in both codes. The solid and dashed lines represent ABINIT and SIESTA calculations, respectively.

4.3.1 The velocity threshold

The ESP varies linearly with projectile velocity, intercepting zero at a finite velocity. This indicates a definitive threshold. Roth *et al.* [127] determine the threshold velocity, by extrapolating the experimental data, to be 0.027 a.u. $\pm 10\%$. We have found the threshold velocity to be different for different channels. It is 0.05 a.u. in the [001] direction and 0.03 a.u. in the [111] and [011] directions.

The threshold behavior has been observed in insulators both experimentally and theoretically. From perturbation theory a relationship between the projectile velocity and electronic transitions is given by (see, *e.g.*, Ref. [141])

$$\mathbf{v}_{th} \cdot \Delta \mathbf{k} = \varepsilon_g, \quad (4.2)$$

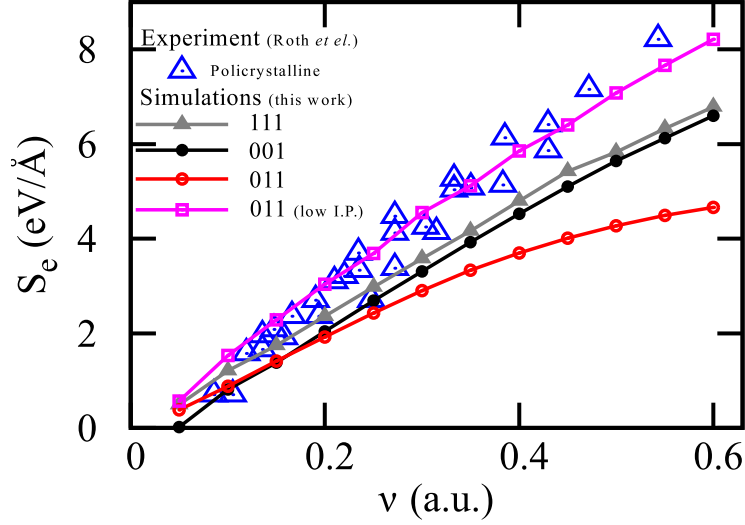


Figure 4.5: Electronic stopping power (S_e) vs velocity (v) of a H projectile in bulk Ge along different crystal directions, as obtained from TD-DFT, and compared with the experimental measurements (empty triangle data points) reported in Ref. [127]. The trajectories in all the three directions are along the centers of respective channels with one additional trajectory in the [011] direction (empty square data points) at a very low impact parameter, (0.24 Bohr position 1 in Figure 4.12).

where \mathbf{v} is the projectile velocity, $\Delta\mathbf{k}$ is the change in momentum in electronic excitations, and ε_g is the band gap and we are taking $\hbar = 1$ for simplification through out this article. This is a known relationship that can be obtained in several different ways; here, we present one such way of deriving it. If a particle of mass m and initial momentum \mathbf{k}_i collides with another particle of mass M and initial momentum \mathbf{K}_i , conservation of momentum requires that

$$\Delta\mathbf{k} \equiv \mathbf{k}_f - \mathbf{k}_i = \mathbf{K}_i - \mathbf{K}_f, \quad (4.3)$$

where \mathbf{k}_f and \mathbf{K}_f are the final momenta of the particles, respectively, and $\Delta\mathbf{k}$ denotes the change in momentum. Conservation of energy requires that

$$\varepsilon_f - \varepsilon_i = \frac{1}{2M}(K_i^2 - K_f^2), \quad (4.4)$$

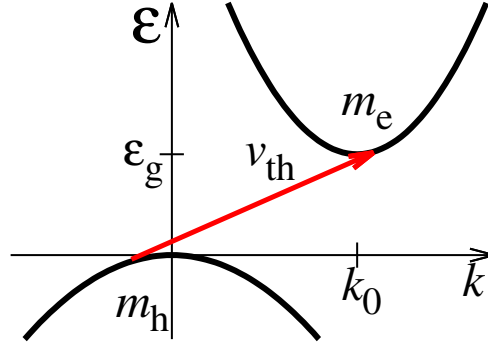


Figure 4.6: Schematic illustration of the relationship between an indirect band gap and the threshold velocity. The arrow shows a common tangent line from the top valence band to the bottom of conduction band.

where ε_i and ε_f are initial and final energies of the particle of mass m , respectively. From equation 4.3, we can write

$$K_i^2 - K_f^2 = 2\Delta\mathbf{k} \cdot \mathbf{K}_i - \Delta k^2. \quad (4.5)$$

On substituting equation 4.5 in equation 4.4, we obtain

$$\varepsilon_f - \varepsilon_i = \frac{1}{M}\mathbf{K}_i \cdot \Delta\mathbf{k} - \frac{1}{2M}\Delta k^2. \quad (4.6)$$

In the limit $M \rightarrow \infty$, the second term in equation 4.6 vanishes, and the rest simplifies to

$$\varepsilon_f - \varepsilon_i = \mathbf{v} \cdot \Delta\mathbf{k}, \quad (4.7)$$

where $\mathbf{v} = \frac{\mathbf{K}_i}{M}$. The smallest excitation in the system would require $\varepsilon_f - \varepsilon_i = \varepsilon_g$, where ε_g is the band gap of the material, with an accompanying change in momentum $\Delta\mathbf{k}$ of the electron undergoing the transition. The threshold velocity of the projectile at the onset of energy loss would therefore relate to the band gap as:

$$\varepsilon_g = \mathbf{v}_{th} \cdot \Delta\mathbf{k}. \quad (4.8)$$

The argument for deducing the excitation condition in a direct band gap case

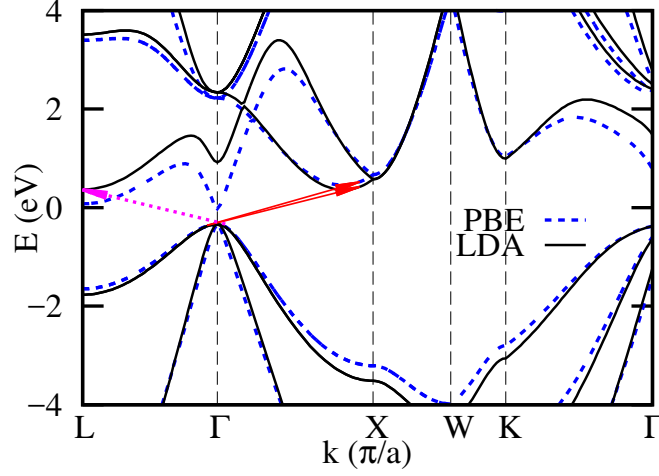


Figure 4.7: Band structure of bulk Ge, calculated using PBE (dashed blue line) and LDA (solid black line). The valence band maxima from the two calculations are aligned with each other for clarity. The two solid (red) arrows illustrate the threshold velocity corresponding to electron-hole excitations in both cases following equation 4.2 in the [001] direction. The dotted (magenta) arrow shows the same (LDA only) in the [111] direction.

can be extended to the case of parabolic bands with an indirect band gap. The condition for the direct band gap [$\varepsilon_g = \frac{1}{2}(m_e + m_h)v_{th}$] can be found in Ref. [141]. A geometrical way to proceed for the indirect band gap is to find the conditions for which a straight line (corresponding to the red arrow in Figure 4.6) would cross both of the parabolas, and from these derive the limiting velocity value below which there is no crossing. Considering first the parabola for electrons, we can write

$$\varepsilon_e = \frac{1}{2m_e}|\mathbf{k}_e - \mathbf{k}_0|^2 + \varepsilon_g. \quad (4.9)$$

The transition line $\varepsilon_t = \mathbf{k}_e \cdot \mathbf{v} + \varepsilon_0$ should cross the parabola ε_e , where ε_0 is a constant defining the vertical positioning of the transition line of slope \mathbf{v} (red arrow in Figure 4.6):

$$\frac{1}{2m_e}|\mathbf{k}_e - \mathbf{k}_0|^2 + \varepsilon_g = \mathbf{k}_e \cdot \mathbf{v} + \varepsilon_0. \quad (4.10)$$

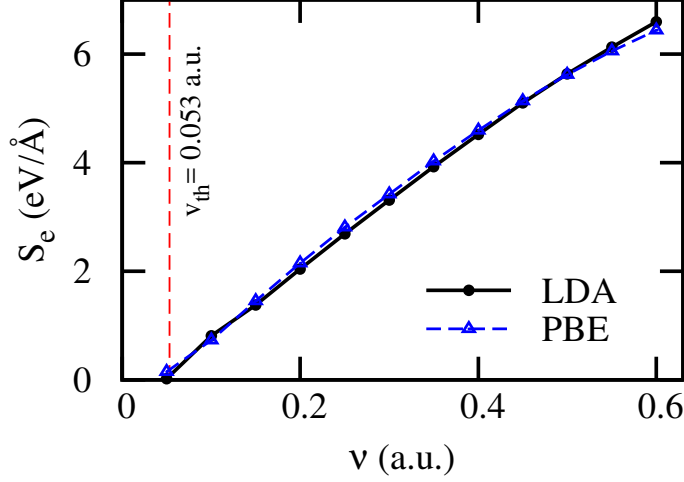


Figure 4.8: The ESP, calculated using the PBE (dashed blue line with triangle data points) and LDA (solid black line with circle data points) functionals, in the [001] direction. The dashed (red) line shows the threshold velocity estimated from the band structure.

Here for simplicity we consider that \mathbf{k}_0 and \mathbf{v} are collinear. Furthermore, since we are interested in obtaining an equation for the threshold velocity, we can consider that \mathbf{k}_e is parallel to \mathbf{v} without loss of generality. The equation 4.10 is quadratic in k_e and can be solved to give

$$k_e = k_0 + m_e v \pm \sqrt{(k_0 + m_e v)^2 - 2m_e(\varepsilon_g - \varepsilon_0) - k_0^2}. \quad (4.11)$$

Similarly, for holes we can write

$$\varepsilon_h = -\frac{k_h^2}{2m_h}. \quad (4.12)$$

Again, the transition line $\varepsilon_t = \mathbf{k}_h \cdot \mathbf{v} + \varepsilon_0$ should cross this parabola. Equating the two gives a quadratic equation in k_h which can be solved to give

$$k_h = -m_h v \pm \sqrt{(m_h v)^2 - 2m_h \varepsilon_0}. \quad (4.13)$$

The two conditions 4.11 and 4.13 (for electrons and holes, respectively) can

be combined as

$$\frac{1}{2}m_h v^2 \geq \varepsilon_0 \geq \varepsilon_g - \frac{1}{2}m_e v^2 - k_0 v; \quad (4.14)$$

for that to be possible,

$$\frac{1}{2}m_h v^2 \geq \varepsilon_g - \frac{1}{2}m_e v^2 - k_0 v, \quad (4.15)$$

leading to

$$\varepsilon_g \leq \frac{1}{2}(m_e + m_h)v^2 + k_0 v, \quad (4.16)$$

or, at $v = v_{th}$,

$$\varepsilon_g = \frac{1}{2}(m_e + m_h)v_{th}^2 + k_0 v_{th}. \quad (4.17)$$

Following equation 4.2, the velocity threshold for an indirect band gap modelled as in Figure 4.6 would correspond to the relation 4.17, where m_e and m_h are the electron and hole masses, respectively, k_0 is the difference in crystal momentum between the valence band maximum and the conduction band minimum, and ε_g is the indirect band gap. It follows that for small k_0 the threshold returns to the direct band gap behaviour (see Ref. [141]), and $v_{th} \propto \sqrt{\varepsilon_g}$. In the case when both parabolas are thin on the scale of k_0 , *i.e.*, when $k_0 \gg \sqrt{(m_e + m_h)\varepsilon_g}$, the threshold velocity rather goes as $v_{th} = \frac{\varepsilon_g}{k_0}$ and is thus linear with ε_g . This argument implies that, for parabolic bands, below a threshold velocity the ESP would drop to zero. For the case of periodic bands, however, this threshold would not be strict, but can still be defined within some accuracy depending on the smoothness of the projectile's potential convoluted with the relevant electronic wave functions [141]. From Equation 4.2, a threshold velocity in a given direction can be estimated from the band structure of the material by finding the gradient of the line which is a joint tangent to the valence and conduction bands, shown by the arrow in Figure 4.6. The threshold velocity estimated from the band structure in the [001] direction is found to be 0.053 a.u. as shown in Figure 4.7 (solid arrows), which is in good agreement with the calculated value of 0.05 a.u. in the same direction. Furthermore, the reason for finding different threshold velocities in different directions becomes clear, as the gradient of the joint

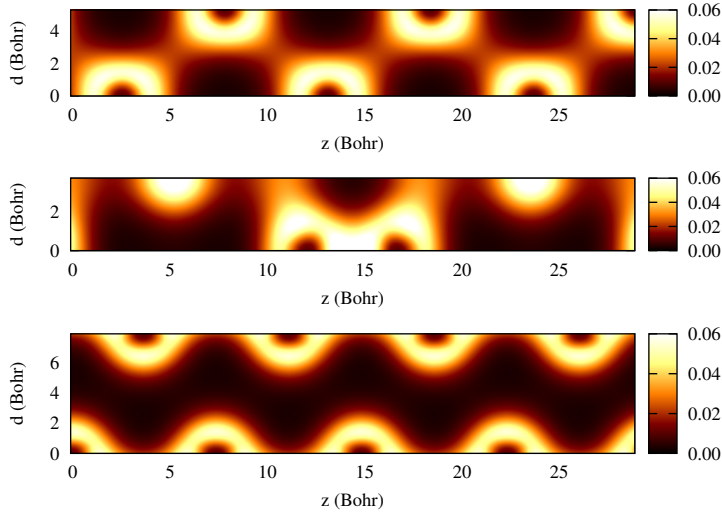


Figure 4.9: The projected electronic densities along the trajectories of projectile in different channels, top [001], middle [111], bottom [011]. The depicted planes are defined by the projectile direction of propagation (z) and a high symmetry perpendicular direction d (the [011] in case of the [001] channel). The electron density increases from dark to bright.

tangent line in the [111] direction (dotted arrow in Figure 4.7) is different and smaller, in qualitative agreement with the TD-DFT calculations. Although the mentioned experiments average out this direction dependence, here we can relate it with the band structure of the host material.

The comparison between LDA and PBE results in Figures 4.7 and 4.8 is of special interest. The electronic band gaps differ by a factor of 2, and yet the ESP shows no significant difference. The LDA functional produces an indirect band gap of 0.70 eV, while the PBE functional produces a direct band gap of 0.33 eV. The calculated band structures are shown in Figure 4.7. However, the ESP calculated using LDA and PBE does not differ significantly at low velocities, and the two calculations produce almost the same threshold. This is a clear indication that the threshold phenomenon is not straightforwardly related to the band gap. The gradient of the joint tangent line of the valence

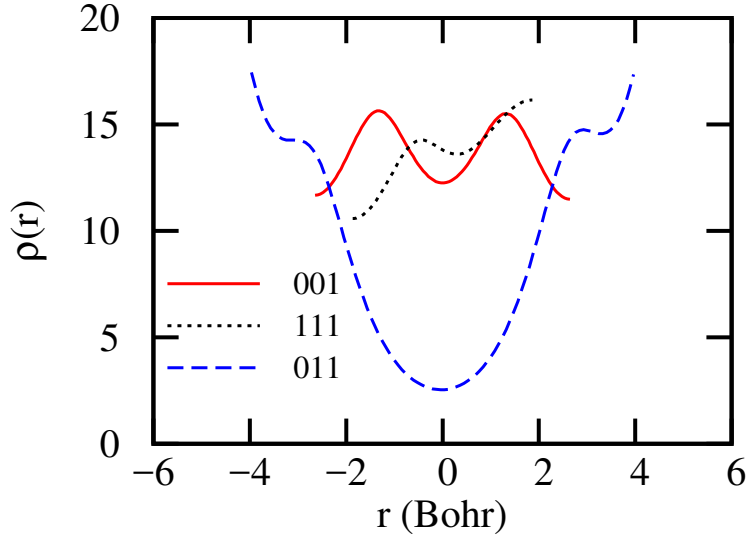


Figure 4.10: The projected density is averaged over the z -axis for all three channels.

and conduction bands in both cases is almost the same (shown by the solid arrows in Figure 4.7). This suggests that the behavior of the ESP threshold at low velocities is rather related to the indirect band gap in the given direction regardless of its being the absolute gap. This further supports the above described model of the ESP threshold. The fact that the relation in Equation 4.17 is accurate using the unperturbed host band structure is somewhat surprising. Such agreement is due to the fact that the perturbing projectile potential does not significantly affect the band structure around the gap.

4.3.2 Direction and impact parameter dependence

We have found that the ESP strongly depends on direction in the crystal, particularly at high velocities. The difference in the ESP between the [111] and [001] channels is up to 3%, and between these two and the [011] channel it is up to 33%. The electron density along these channels is shown in Figure 4.9 in suitable planes. The electron density is then averaged over the z -axis,

as shown in Figure 4.10. The direction with the lowest ESP for a channeled projectile ([011]) has a lower average density in the center of the channel compared with the two other channels. For [001] and [111] the averaged density is not significantly different, similarly what happens for the ESP. This suggests that the ESP in channeling conditions can be related to the average density along the trajectory, corroborating and supporting assumptions and approximations used in the literature [142–145].

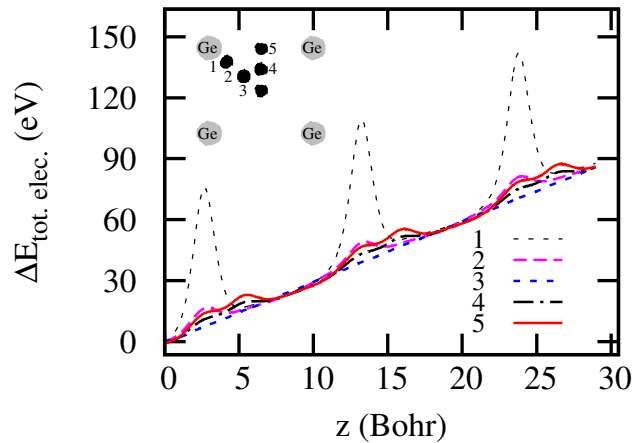


Figure 4.11: Electronic energy against distance along the different projectile trajectories in the [001] direction. The projectile velocity for all the trajectories is 0.5 a.u.. The inset shows a sectional view of the [001] channel and the trajectories. The gray circles represent Ge atoms in different transverse planes (defining the channel), while the black circles show the projectile positions for different impact parameters.

We have simulated five different trajectories in the [001] channel, as shown in the inset of Figure 4.11. The five trajectories are chosen to sample different impact parameters (different closest distance to any of the host atoms) within the channel. For each trajectory we show the total energy of the electronic subsystem versus distance for a given velocity of 0.5 a.u. in Figures 4.11 and 4.12. The plots in Figure 4.11 show the energy profile along the [001]

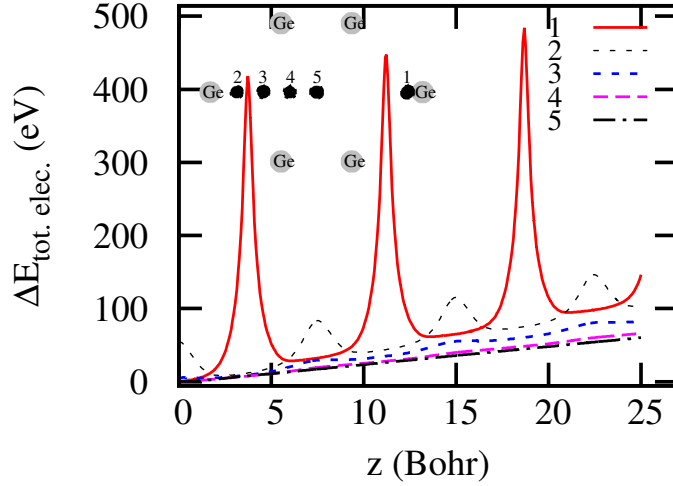


Figure 4.12: Electronic energy against distance along the different projectile trajectories in the [011] direction. The projectile velocity for all the trajectories is 0.5 a.u.. The inset shows a sectional view of the [011] channel and the trajectories. The gray circles represent Ge atoms in different transverse planes (defining the channel), while the black circles show the projectile positions for different impact parameters.

channel; the periodic variation in the electronic energy reflects the periodicity of the crystal. A larger variation is seen for the trajectories with the lowest impact parameters, as should be expected; however, the base-lines of all the trajectories have the same gradient, which shows that, in this direction, the ESP is quite insensitive to impact parameters. A similar calculation in the [111] direction gives the same result (not shown). However, the ESP strongly depends on impact parameter in the [011] direction. The total electronic energy profile for five different trajectories in this direction is shown in Figure 4.12. The change in ESP from the highest impact parameter, i.e., the center of channel (empty circle data points in Figure 4.5) and the lowest impact parameter, i.e., close to the edge of channel (empty square data points in Figure 4.5) changes by a factor of 2. Again looking at the average density

in the [011] direction (Figure 4.10), we can see that it changes by a factor of 3 from the center to the edge of the channel. This reflects the proposed strong correlation between the ESP and the averaged local density within a small radius of the impact parameter. It is to be expected that such a radius (or cross section) would increase for slower projectiles. This is verified by the larger slope of the ESP for the center of the [011] channel trajectory for lower velocities. Indeed, the low velocity limit displays the same behavior for all trajectories, indicating that the larger cross section is seeing the same average electron density in all the cases.

In experiment the ESP is naturally averaged over different directions and impact parameters, and precise knowledge of this averaging mechanism would be necessary to obtain a comparable average from our calculations. We have not attempted to do so, although it is clear from Figure 4.5 that any such averaging would result in a slight underestimation with respect to experiment, especially for high velocities.

Chapter 5

Electronic stopping power of He in Ge

5.1 Motivation

The electronic stopping power of light projectiles, such as H and He, is generally found to be linearly proportional to the projectile velocity in the low velocity regime. However, recent theoretical [40, 44] and experimental [124, 127, 146] works have showed that this is not always true. The band structure of the host material [40, 44] and sometimes combined with the projectile states [45] plays an important role. The electronic stopping power of He in various materials (metals and insulators) has been studied, both theoretically [40, 75] and experimentally [124–126, 129]. The electronic stopping power of He in Al in experiments shows a change of slope around 0.2 a.u. of velocity [125]. But this change of slope does not appear in the RT-TDDFT based calculations [75], thus remains unexplained. A similar change of slope is experimentally measured in Cu and Au [124] which has been understood as an effect of the band structure within RT-TDDFT calculations [40, 44].

Scattering of the low energy He ions off the Ge surface has been subject of experimental studies [147]. Recently \mathcal{S}_e of He in Ge has been experimentally measured [148]. The \mathcal{S}_e of He in Ge shows a change of slope around 0.2 a.u.

of velocity. This background makes He-Ge an interesting system to study. We have calculated the \mathcal{S}_e of He in Ge in the velocity of range of 0.05 to 0.6 a.u..

5.2 Method

The simulation method explained in Chapter 4 used to calculate the \mathcal{S}_e of H in Ge is used for this system. A 96-atom supercell constructed by $2 \times 2 \times 3$ conventional cubic cells of Ge was used. A k -point mesh of $4 \times 4 \times 3$ points generated with the Monkhorst-Pack method [134] corresponding to an effective cutoff length of 22.36 Å [135] was used. The exchange and correlation functional was evaluated using the local density approximation (LDA) in the Ceperley-Alder form [80]. A double- ζ polarized (DZP) basis set was used to represent the valence electrons of the projectile and the host material (see Table 5.1), while the core electrons were replaced by norm conserving Troullier-Martins pseudopotentials [131], factorized in the separable Kleinman-Bylander (KB) form [132] (see Table 5.2). The rest of the simulation parameters for the bulk Ge as same as given in Chapter 4.

Table 5.1: Cutoff radii $r(\zeta_1)$, $r(\zeta_2)$ of first and second zeta functions respectively, and the soft-confinement potential’s internal radius r_i are in Bohr; the soft-confinement potential pre-factor V_0 is in Ry.

Species	n	l	V_0	r_i	$r(\zeta_1)$	$r(\zeta_2)$
Ge	3	2	50	6	6.50	
	4	0	50	6	6.50	5.00
	4	1	50	6	6.50	4.50
	4	2	50	6	6.50	
He	1	0	50	6	8.00	3.00
	2	1	100	0	8.00	

Table 5.2: Matching radii for each of the angular momentum channels of Ge and He. All lengths are in Bohr.

Species	s	p	d	f
Ge($4s^24p^2$)	2.06	2.85	2.58	2.58
Ge($3d^{10}4s^24p^2$)	1.98	1.98	1.49	1.98
He($1s^2$)	1.14	1.14	1.14	1.14

The calculations are performed in channeling conditions along the [001], [011], and [111] directions.

5.3 Results and Discussion

The calculated \mathcal{S}_e of He in Ge in different channels is compared with the experimental results [148] in Fig. 5. A clear velocity threshold is observed at 0.05 a.u. of velocity for the [001] and 0.07 a.u. in [011] channel. The velocity threshold for the [111] channel is estimated to be 0.02 a.u. by extrapolation. The velocity threshold is in line with the conclusions, discussed in Chapter 4, in case of H in Ge. The calculated \mathcal{S}_e in [111] channel is only slightly larger than that of the [001] direction. The experimental values of the \mathcal{S}_e are for a polycrystalline sample, hence, a direct comparison with the \mathcal{S}_e calculated in channeling conditions is not straightforward. However, overall agreement between the calculated and the experimentally measured \mathcal{S}_e is reasonable, except for the [011] channel. The calculated \mathcal{S}_e in [011] direction with hyperchanneling condition, given by red line joining red square data points in Fig. 5.1, is by a factor of 3 smaller than that of the [111] and [001] channels.

The theoretically calculated \mathcal{S}_e not only varies widely between different channels, but within a given channel for different impact parameters. We have calculated \mathcal{S}_e with different impact parameters as shown in Fig. 5.2 in the widest channel, which in this case is the [011] channel. The \mathcal{S}_e shows a

very strong dependence on impact parameters in this direction. From center to edge (from large to small impact parameter) the \mathcal{S}_e increases by a factor of 4. As discussed in the previous chapter, steep change in electronic density from center to edge of the channel is most like cause of this behaviour. Very little or no impact parameter dependence is observed in our calculations in the other two channels. The \mathcal{S}_e of He in Ge is lower than that of H in Ge, in

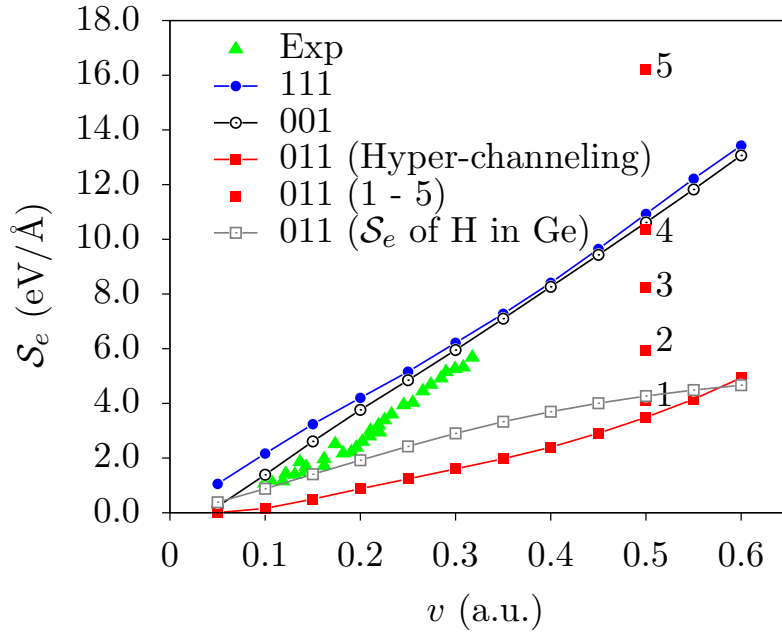


Figure 5.1: The calculated electronic stopping power (\mathcal{S}_e) is compared with experimental data. The solid green triangle data points represent experimental data [148]. The solid blue circle data points show the calculated \mathcal{S}_e in the [111] channel. The empty black circle data points show the calculated \mathcal{S}_e in the [001] direction. The solid red square data points show the calculated \mathcal{S}_e in the [011] direction. The solid red data points from 1 to 5 at $v = 0.5$ a.u. show the calculated \mathcal{S}_e in the [011] direction with different impact parameters as shown in Fig. 5.2. The empty grey square data points show the calculated \mathcal{S}_e of H in Ge in the [011] direction.

the [011] channel as show in Fig. 5.1. This is not the case in any of the other

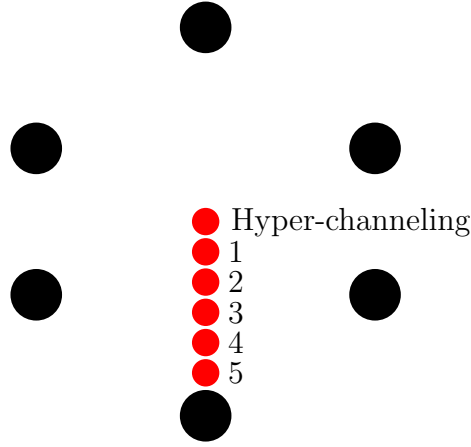


Figure 5.2: Schematic representation of impact parameters in the [011] direction. The black circles represent the Ge atoms outlining the sectional view of the [011] channel. The red circles represent transverse position of the projectile in the channel.

two channels. The [011] channel is the widest and has low electronic density around the center of channel (as discussed in Chapter 4, and shown in Fig. 4.10). This observation is in agreement with jellium models [19], that at low densities the \mathcal{S}_e of He is lower than that of H.

The change of slope observed in experimental measurements around 0.2 a.u. of velocity does not appear in our calculations. Although there is no clear explanation available, but its appearance in other systems around the same velocity suggest that a cross-over from hyper-channeling to more and more random trajectories as a possible cause. At velocities below 0.2 a.u. the projectile is more likely to get channeled and sample only large impact parameter trajectories. While at relatively higher velocities, the channeling becomes less likely and the projectile samples all impact parameters. The strong impact parameter dependence revealed in our calculations means low impact parameter trajectories would produce higher stopping power. Another likely cause of the change of slope of the \mathcal{S}_e could have been cross-over to the excitation of d -electrons of Ge. However, we have calculated the \mathcal{S}_e with d -electrons of Ge treated explicitly. The results are shown in Fig. 5.3. No

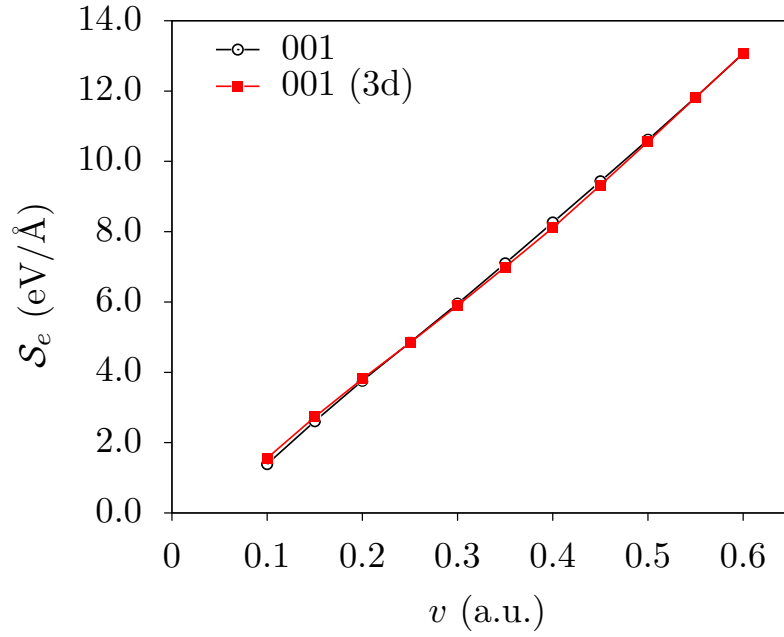


Figure 5.3: The electronic stopping power (\mathcal{S}_e) of He in Ge in the [001] direction. The black empty circle data points show the case when d -electrons of Ge are frozen into core by the pseudopotential approximation. The solid red square data points show the case when d -electrons are Ge are explicitly treated as valence electrons.

additional contribution to the \mathcal{S}_e is observed over the range of projectiles velocities considered in this work.

Chapter 6

Electronic stopping power of Ni in Ni

Electronic stopping power in the keV/Å range is accurately calculated from first principles. The energy loss to electrons in self-irradiated nickel, a paradigmatic system, using real-time time-dependent density functional theory is studied. Different core states are explicitly included in the simulations to understand their involvement in the dissipation mechanism. The experimental data are well reproduced in the projectile velocity range of 1.0 – 12.0 atomic units. The core electrons of the projectile are found to open additional dissipation channels as the projectile velocity increases. The systematic, explicit, and flexible inclusion of the core states reveals that almost all of the energy loss is accounted for within this first principles approach. Core electrons as deep as 2s are treated explicitly and are found to be necessary to account for the ion energy loss at relatively high projectile velocities.

6.1 Background

The pioneering work presented in Refs. [36–49, 90] is not only in good agreement with experiments and provides further insights into the problem

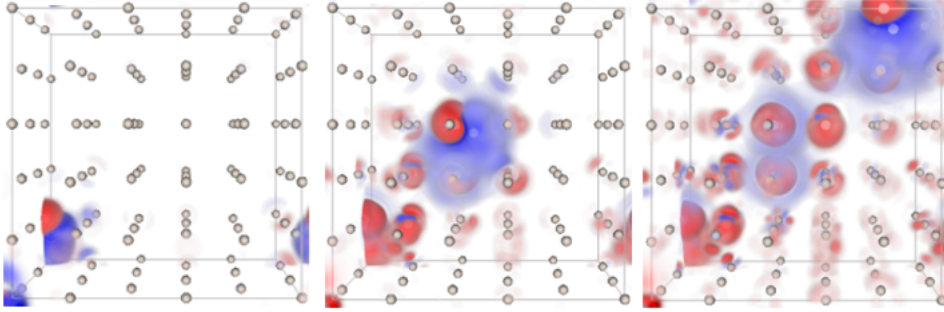


Figure 6.1: Ni projectile shooting in the $[111]$ direction as viewed from the $[100]$ direction. The snapshots of density difference (excited density minus ground state density) are shown at times (from left to right) 0.10 fs, 0.15 fs, and 0.30 fs. Regions in blue color indicate the positive difference and those in red indicate the negative difference.

of electronic stopping of ions but demonstrably sets the stage for using RT-TDDFT to study this problem in a wide variety of systems. However, most of the previous RT-TDDFT based studies have been limited to simple projectiles (H, He) [48], low projectile energies and mostly lighter host elements with low electronic stopping. In most of these cases, the electronic stopping power, which is the energy lost by the projectile per unit path length, $\mathcal{S}_e = -\frac{dE}{dx}$, is in the order of $10 \text{ eV}/\text{\AA}$ and at such energy deposition rates very little or no permanent damage is expected. The effect of explicit treatment of the core and semi-core electrons of the target with light projectiles (H,He) on the electronic stopping power has been studied using LR-TDDFT [35] and RT-TDDFT [40, 42]. Ojanperä *et al.* [41] have shown the significant effect of core electrons of the projectile using RT-TDDFT. The self-irradiated transition metals are known to have extremely high values of \mathcal{S}_e [58], in the range of $\text{keV}/\text{\AA}$, which can cause significant permanent damage, mainly in the form of ion-tracks [149]. The self-irradiated transition metals have not been studied using first-principles methods before, with the full effect of core states. In fact, no material with \mathcal{S}_e values in $\text{keV}/\text{\AA}$ range has ever before been simulated using RT-TDDFT. The physics of these systems remains poorly

Electronic configuration		Pseudo/Label
$1s^2 2s^2 2p^6 3s^2 3p^6$	$4s^2 3d^8$	Ni10
$1s^2 2s^2 2p^6 3s^2$	$3p^6 4s^2 3d^8$	Ni16
$1s^2 2s^2 2p^6$	$3s^2 3p^6 4s^2 3d^8$	Ni18
$1s^2$	$2s^2 2p^6 3s^2 3p^6 4s^2 3d^8$	Ni26
core	valence	

Table 6.1: Different pseudopotentials and labels utilised in this work. The number next to the element name indicates the number of explicit electrons simulated, for the projectile and for each of the host atoms.

explained and quite challenging to study within first principle approaches. The excitation of core states and their contribution in dissipation is expected to be critical in explaining extremely high stopping powers [150]. The precise mechanism of these excitations and their relative contributions remains poorly understood.

We have considered the prototypical problem of a self-irradiated transition metal, Ni, in which a primary knock-on atom (PKA) shoots through the bulk. This is a common occurrence in materials exposed to neutron radiation. Ni based alloys are known for their radiation tolerance [151], thermal stability and optimal mechanical properties, making them promising candidate materials for next generation energy and aerospace applications [152–154]. The presence of Ni in structural alloys is known to play an important role in mitigation of swelling under irradiation [155]. Ni, along with iron (Fe) and tungsten (W), is the subject of extensive radiation damage research [8, 156, 157]. Most of the radiation damage studies are limited to classical and adiabatic molecular dynamics simulations, but an accurate description of radiation damage demands a good characterization of non-adiabatic electronic

contributions. They become very pronounced in the case of heavy projectile and heavy target.

There are no direct experimental data available for the stopping power of Ni in Ni, except for the element-extrapolations of Stopping and Range of Ions in Matter (SRIM) model [58]. The SRIM model shows that in self-irradiated Ni, *nuclear stopping* is dominant for velocities up to 1 a.u. and quickly diminishes beyond it (see Fig. 6.2). However, \mathcal{S}_e becomes dominant beyond 1 a.u. of velocity and accounts for almost all of the stopping power in the high velocity regime. In this work we have considered the velocity range from 1.0 to 12.0 a.u. which includes the maximum of electronic stopping.

6.2 Simulation Method

We have used the RT-TDDFT formalism within the adiabatic local density approximation (ALDA) [80] for exchange and correlation potential. We have used the first principles (DFT, TDDFT) code, QB@LL [84, 86], for our calculations. The RT-TDDFT implementation is described in Ref. [85].

The Kohn-Sham wavefunctions are expanded in a plane-wave basis. The \mathcal{S}_e changes less than 3% as the energy cutoff is varied from 160 to 400 Ry (see Fig. 6.3). An energy cutoff of 160 Ry is used for the calculations. The ions are represented by norm-conserving non-local pseudopotentials, factorized in the Kleinman-Bylander form [132]. A supercell containing 108 atoms was constructed by $3 \times 3 \times 3$ conventional cubic cells of face-centred Ni crystal. The experimental value of 3.52 Å for the lattice constant is used.

The simulation scheme follows an almost virtual experiment. A Ni interstitial is placed inside the supercell and a self-consistent ground state is obtained. The self-consistent ground state serves as an initial state for the real-time evolution of Kohn-Sham wavefunctions. From the self-consistent ground state, the Ni interstitial is instantaneously given a velocity at $t = 0$ mimicking a PKA event, hence becoming a projectile. The sudden kick causes a relatively short-lived transient before the system enters a dynamical steady

state. As the projectile shoots through the bulk, the Kohn-Sham wavefunctions are propagated in time using a fourth order Runge-Kutta integrator [85] combined with all atoms fixed except the projectile, which moves with a constant velocity. The constrained ionic motion is based on the assumption that ionic velocities, for the considered simulation time and velocities, do not change significantly. After testing the convergence of simulation parameters, a time step of 0.2 attoseconds or smaller is used for time-integration ($dt = \frac{dx}{v}$ by additionally requiring $dx \leq 0.01 a_0$). The total Kohn-Sham energy of the electronic sub-system is recorded as a function of distance travelled by the projectile. The constrained motion of ions guarantees that the change in Kohn-Sham energy along the trajectory corresponds to the ‘electron-only’ stopping (\mathcal{S}_e) experienced by the projectile. The Kohn-Sham energy as a function of distance is recorded for different velocities. The slope of each of those curves is obtained by simple linear curve fitting as detailed in Refs. [42, 44, 90], which gives \mathcal{S}_e for that particular velocity. All the calculations in this work are in channeling condition along the [111] direction of the face-centred cubic crystal of Ni.

6.3 Results and Discussion

We have investigated the contribution of core-states by controlling their inclusion via a sequence of different pseudopotential approximations. The pseudopotential approximation replaces core electrons by an effective potential that defines the physics of the valence electrons. It is in general a necessary approximation when working with a plane wave basis [77]. The core states frozen into a pseudopotential cannot polarize or take part in any dynamic process. Redefining the partition between valence and core electrons allows us to tailor the pseudopotential approximation. We have exploited this freedom to study the participation of the different core states in the process of energy deposition. We have generated four pseudopotentials, namely, Ni10, Ni16, Ni18, and Ni26 with different valence electrons, as defined in Table 6.1 [159–

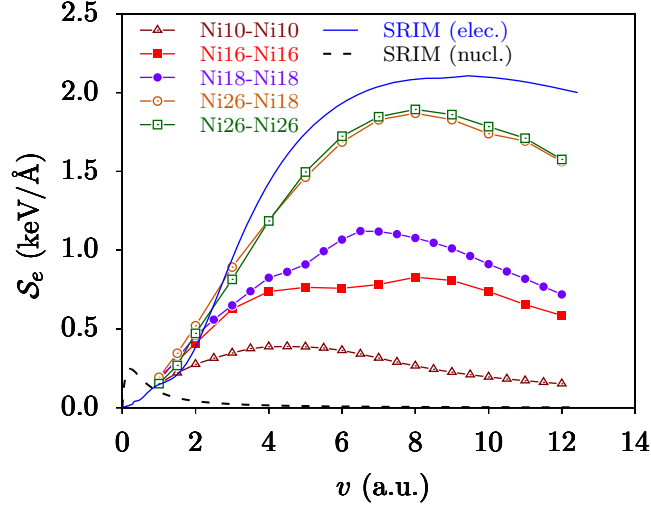


Figure 6.2: Calculated electronic stopping power (\mathcal{S}_e) of a Ni projectile in a Ni crystal with different electronic configurations, as a function of velocity, compared with the SRIM data. The dashed (black) curve shows the nuclear stopping power from SRIM data. The solid (blue) curve represents the electronic stopping power from SRIM data [158]. The open triangle (maroon) data points show calculated \mathcal{S}_e of a Ni10 projectile in a Ni10 host. The solid squares (red) data points display the calculated \mathcal{S}_e of a Ni16 projectile in a Ni16 bulk. The Solid circles (indigo) data points are for a Ni18 projectile in Ni18 host. The open circle for Ni26 in Ni18 and the open squares for Ni26 in Ni26

161].

The results of our calculations, for the different core/valence sets, are presented and compared with the SRIM data in Fig. 6.2. The calculated \mathcal{S}_e of Ni10 in Ni10 (Ni projectile and host atoms all with 10 explicit electrons) is clearly underestimated in practically the whole velocity range investigated, as shown by open triangle data points in Fig. 6.2, by about an order of magnitude as compared to SRIM data (solid line in Fig.6.2). Not only the \mathcal{S}_e is underestimated, the maximum of \mathcal{S}_e occurs around 5 a.u. of velocity while SRIM predicts it to peak around 9 a.u.. However, redefining more electrons

from frozen core to explicitly simulated valence states makes a very significant difference. In an otherwise similar calculation with a Ni16 projectile in Ni16 bulk, the calculated \mathcal{S}_e increases almost by a factor of two, as shown by the solid square data points in Fig. 6.2. This is a strong direct evidence of the core states participation in the energy dissipation mechanism. However, the \mathcal{S}_e remains underestimated in comparison to the SRIM data. Digging further in the same direction; we have calculated the \mathcal{S}_e of Ni18 in Ni18 bulk and Ni26 and Ni26 bulk. The Ni18 projectile in Ni18 bulk calculation, solid circle data points in Fig. 6.2, confirms the trend, although does not fully account for the underestimation in the \mathcal{S}_e . The Ni26 projectile in Ni26 bulk case, open square data points in Fig. 6.2, produces the \mathcal{S}_e , in perfect agreement with the SRIM data from 1.0 to 3.0 a.u. of velocity, while it is underestimated by less than 10% between 3.0 to 9 a.u., which is within the anticipated inaccuracy in the SRIM model for heavier elements [158].

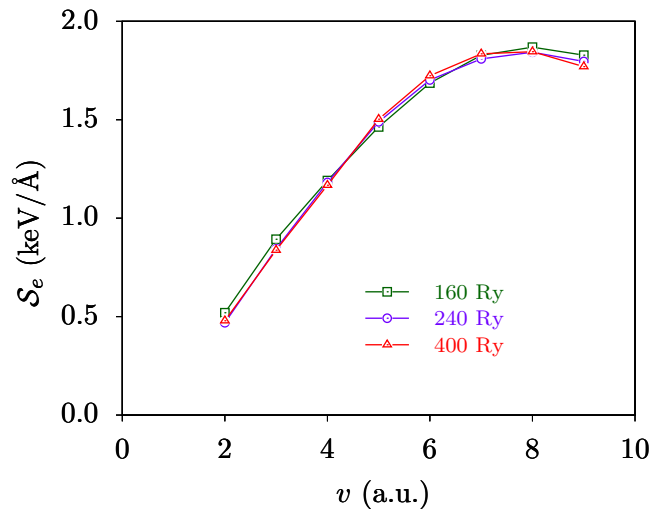


Figure 6.3: The convergence of the electronic stopping power with respect to the plane-wave energy cutoff

Apart from the good agreement with the SRIM model based data, these results provide a very clear evidence that core states as deep as $2s^22p^6$ very significantly contribute to the \mathcal{S}_e of the swift ions. Another very important

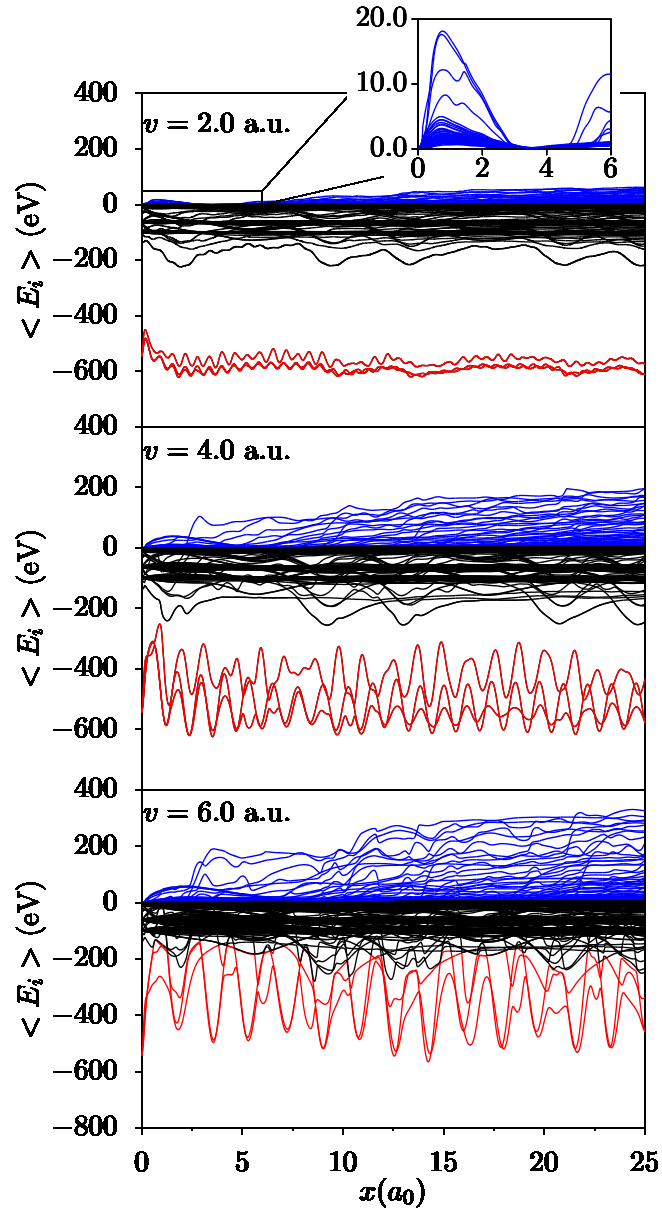


Figure 6.4: The energy expectation values of the TDKS wavefunctions as a function of the projectile position. The inset in the top panel shows the scale at initial transient, due to initial velocity kick, disappears.

inference is that if the right number of core electrons are allowed to participate in the dynamic processes, almost all of the dissipation can be accounted for

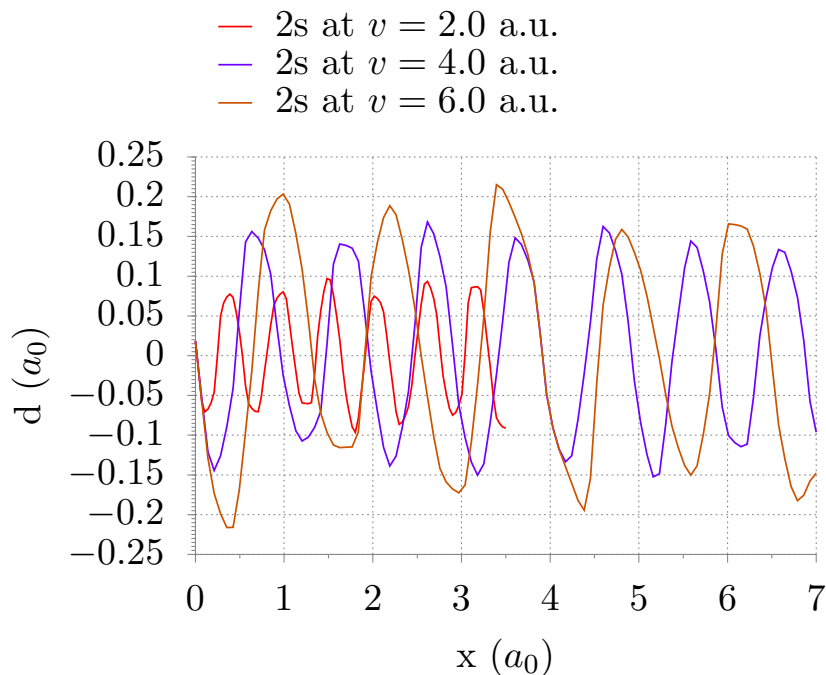


Figure 6.5: The center of charge of the 2s orbital with respect to the position or projectile along the line of motion.

within the RT-TDDFT formalism. The \mathcal{S}_e values for different valence states converges in the low-velocity limit. On the other hand, the \mathcal{S}_e of the system with limited valence states saturates at higher velocities. The smaller the number of valence electrons, the earlier the \mathcal{S}_e saturates with increasing velocity. This further confirms that the observed effect is truly due the contribution of core electrons.

To distinguish the effect of core electrons in the host from those of the projectile, we have computed the \mathcal{S}_e of a Ni26 projectile in a Ni18 host, as given by open square data points in Fig. 6.2. It is very interesting to note that it almost exactly matches the \mathcal{S}_e of the Ni26 in Ni26 case. The only difference, between Ni18 in Ni18 (solid circles in Fig. 6.2) and Ni26 in Ni18 is the presence of $2s^2 2p^6$ electrons of the projectile, which increases the \mathcal{S}_e by a factor of almost two. This points to the importance of bare charge of the highly ionized projectile. This result strongly suggests that the critical

contribution comes from the ionisation of $2s^22p^6$ electrons of *the projectile* while the deep electrons of the host do not make any significant difference.

Another important characteristic of the $\mathcal{S}_e(v)$ curve is the position of the peak. As more and more core electrons are treated explicitly, the \mathcal{S}_e peak position gradually corrects by shifting rightwards. The SRIM data predicts the \mathcal{S}_e peak position around 9.4 a.u. of velocity. Our calculations produce the \mathcal{S}_e peak position around 8.0 a.u. of velocity, underestimated by 15%.

The Ni26 projectile in a Ni18 host allows us to identify the dynamics of core electrons. In Fig. 6.4 we show the time evolution of the energy expectation values of the occupied Kohn-Sham orbitals for different projectile velocities. It shows different electronic levels and bands, the three lowest corresponding to the initially occupied $2p$ levels of the projectile (Ni26) (although the calculation of \mathcal{S}_e is well converged with respect to the energy cutoff, the convergence of individual core states would require higher cutoff energies, nevertheless, they offer a good qualitative insight). Two distinct features, depending on the velocity regime, are immediately noticeable. At low velocities the core occupied levels remain in their energy range, while the valence band shows that some dynamical states acquire energies that eventually reach hundreds of eV above the Fermi energy, forming an increasing set of ballistic electrons. At high velocity the effect is more pronounced, both in the number of electrons and the energy scale. More importantly we see an effect that is absent at low velocity, related to the excitation of core electrons of the projectile into valence band energies and further into the ballistic range. This excitation of core electrons of the projectile coincides with the transient region, which we interpret as an early ionisation of the projectile.

It is interesting to note that the oscillations in the energy expectation values of the $2p$ states do not commensurate with lattice spacing, but change with velocity, rather maintaining a constant period in time. These oscillation can be related to the oscillation of core-orbitals in real space. For example, we have calculated the center of charge, d_i , due to each core orbital with

respect to the position of the projectile r_p , along the line of motion;

$$d_i = r_p - \frac{\langle \psi_i | r | \psi_i \rangle}{\langle \psi_i | \psi_i \rangle}. \quad (6.1)$$

The center of charge, for $2s$ orbital, is shown in Fig. 6.5 for different projectile velocities. The $2s$ and $2p$ orbitals show this oscillation in real space as show in Figs. 6.6 and 6.7, respectively. The deformation increases but the time-period of oscillations remains constant. It is unclear if this fluttering in real space contributes to the dissipation mechanism. It would be an interesting prospect to explore the underlying cause of this flapping which bears some similarity with the classical flapping instability in an elastic media exposed to fluid flow.

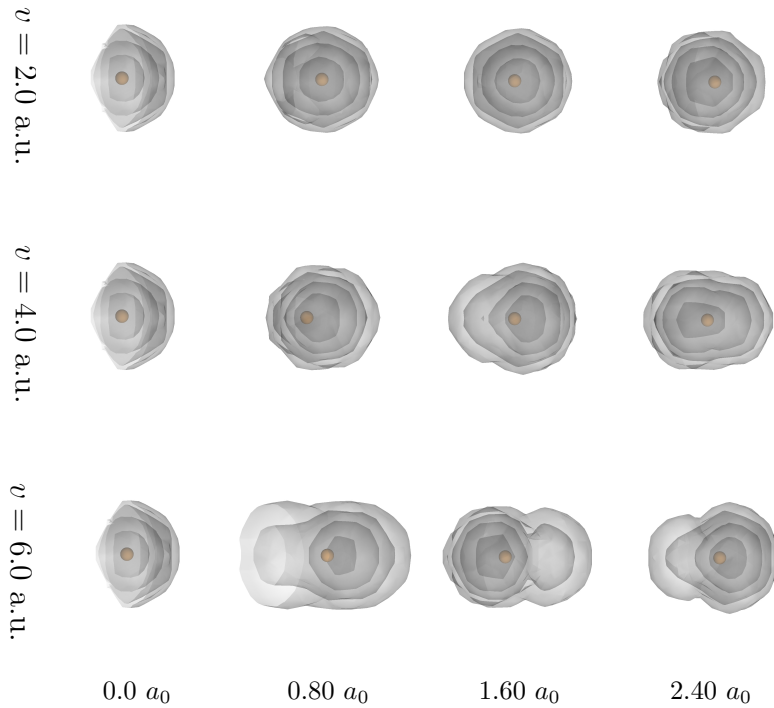


Figure 6.6: The contour plot of the $2s$ orbital at different positions along the trajectory. The initial orbital appears clipped because the projectile is initially placed at $[011]$ plane of the supercell. The yellow ball shows position of the projectile. The contours (isodensities) are plotted using logscale.

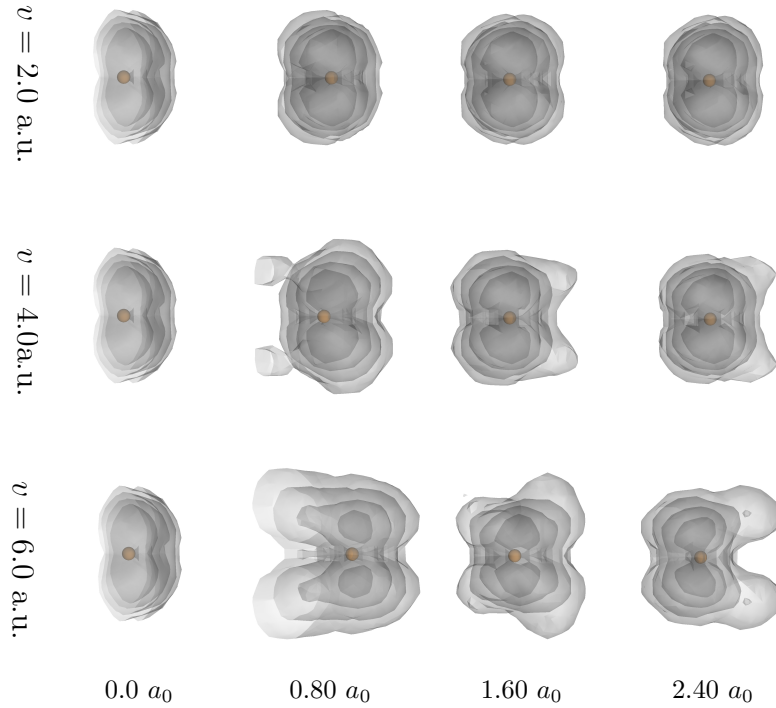


Figure 6.7: The contour plot of the one of $2p$ orbitals along the trajectory at different positions. The initial orbital appears clipped because the projectile is initially placed at $[011]$ plane of the supercell. The yellow ball shows position of the projectile. The contours (isodensities) are plotted using logscale.

In summary, for Ni, like other transition metals that show a very high electronic stopping power, core electrons were found to have a major contribution in it, particularly those of the projectile. Adding explicit electrons in the simulation has the dual effect of adding more excitation channels, mainly in the form of electrons of the host, and making the ion potential deeper when ionization occurs, mainly in the projectile. The 10 electrons per atoms with frozen core seems to be a good approximation only below $v < 1$ a.u., while 18 electrons per atom is valid for $v < 2$ a.u. before saturating. For larger velocities, more electrons need to be taken into account to reproduce a reasonable value for the stopping power; specially for the projectile ion.

Chapter 7

Electronic stopping power of W in W

7.1 Motivation

Transition metals and their alloys are of primary interest for nuclear engineering and energy applications. For this reason the interaction with fast ions is of primary interest. Tungsten for its unique physical and chemical properties is being considered the most promising candidate material for primary containment components in nuclear fusion reactors [162]. There is a growing interest in studying the nature of damage endured under sustained radiation exposure [163, 164]. Recent experimental [165] and atomistic simulation [166] studies have focused on damage caused by primary knock-on atoms (PKAs). An energetic neutron or α -particle can knock out an ion of the target material from its equilibrium position setting it into motion. This is called a PKA.

The PKA, as it shoots through the host material, dissipates its energy by exciting host electrons and elastic collisions with host ions. This interaction of the PKA with the host material determines the scale and nature of damage produced in the target. The role of energy dissipation to electrons in the classical molecular dynamics simulation of radiation damage is modelled by introducing friction terms in the equations of motion and a heat-bath [59, 167,

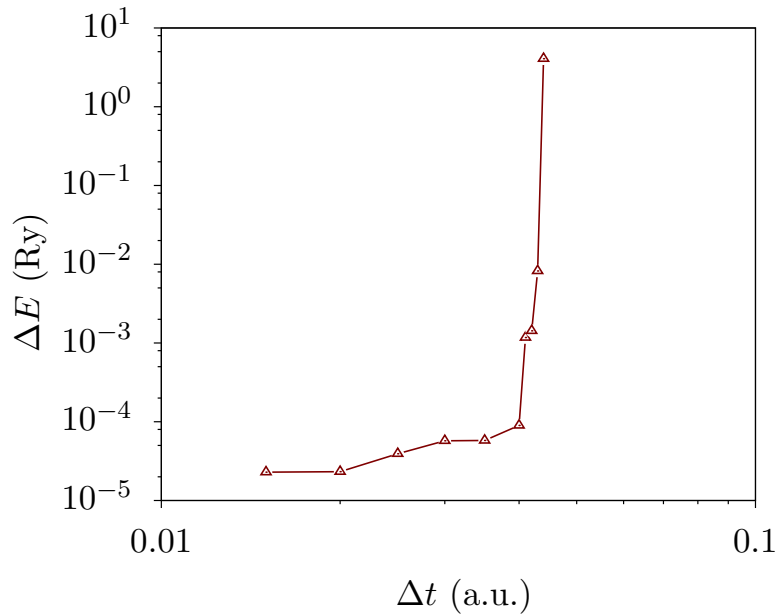


Figure 7.1: Change in the total Kohn-Sham energy for a given projectile distance with different time steps.

[168]. The radiation damage in W has been studied using classical molecular dynamics simulations. The electronic effects, included as a friction term and via a heat bath, have been shown to significantly effect the state of final damage [169]. The accuracy and predictive ability of such simulations depend on the accurate knowledge of the electronic stopping power and electron-phonon coupling. The role of electronic effects in radiation damage beyond these classical models remains to be understood.

The calculation of electronic stopping power using first principles approaches such as RT-TDDFT not only provides accurate data for classical molecular dynamics simulation but offers a better understanding of the dissipation mechanism. It further opens the possibility of going beyond the classical simulations to study radiation damage [170, 171].

We have calculated the electronic stopping power (\mathcal{S}_e) of self-irradiated W, a paradigmatic heavy metal with \mathcal{S}_e running into several thousands of eV/Å [58].

7.2 Simulation Details

The \mathcal{S}_e of W in W is calculated in hyper-channeling conditions in the [001] direction. The Kohn-Sham wavefunctions are expanded in plane-wave basis with an energy cutoff of 280 Ry. The atoms are represented by norm-conserving non-local pseudopotentials, factorized in the Kleinman-Bylander form [132]. A supercell of 108 atoms is constructed by $3 \times 3 \times 6$ conventional cubic cells of body-centered W crystal. The experimentally measured lattice constant of 3.16 Å is used. The Kohn-Sham wavefunctions are propagated in time using the fourth order Runge-Kutta algorithm implemented in Qbox code [85]. A time step of 0.02 a.u. or smaller is used, after convergence tests for the integration (See Fig. 7.1). The time is decreased, when necessary, to ensure $\Delta x \leq 0.01 a_0$ for the projectile.

The positions of the target atoms are constrained while the projectile is constrained to move with a constant velocity. For each given velocity the change in total Kohn-Sham energy of the electronic subsystem is recorded as a function of projectile distance to extract the \mathcal{S}_e . The projectile velocity range considered for these calculations is 1.0 – 12.0 a.u.

7.3 Results and Discussion

The \mathcal{S}_e is calculated using different pseudopotentials for the projectile and the host atoms. This approach allows to control the valence charge both in the target and the projectile. We have used three different pseudopotentials with valence charge of 12, 20, and 26 denoted by W12, W20, and W26 respectively. The results are compared between the cases with different valence charge and with the stopping data from SRIM model. Like the case of Ni in Ni, the valence charge or the number of electrons treated explicitly play a very important role. The \mathcal{S}_e increases by almost a factor of 2 when the valence charge on projectile is changed from 12 to 20 in the same target (W12) as shown by empty triangle data points (W12-W12) and the solid square data points (W20-W12) in Fig. 7.2. However, the \mathcal{S}_e of W20 in W12 and W20 in

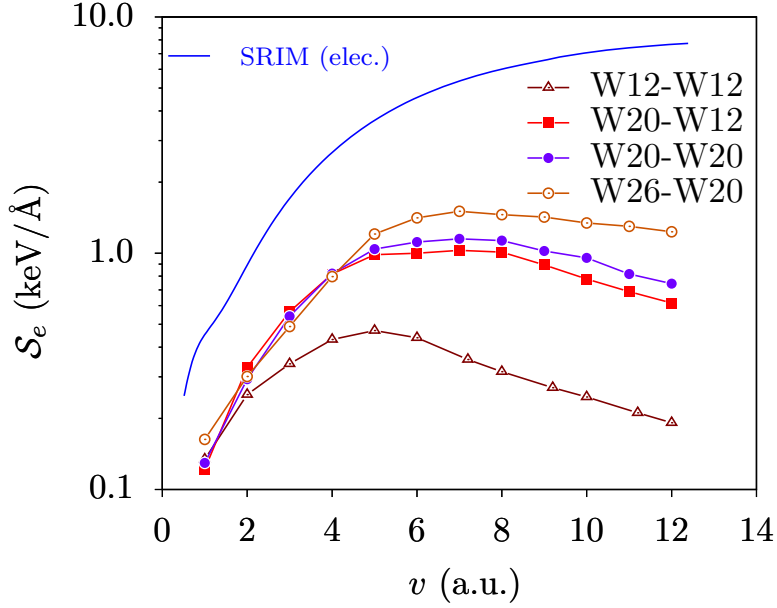


Figure 7.2: The electronic stopping power, \mathcal{S}_e , of W projectile in W host with different valence charge and the stopping data from the SRIM model for the same system is shown. The solid blue line shows \mathcal{S}_e from the SRIM data. The empty triangle data points show the stopping for the case in which both the host and the projectile have a valence charge of 12 (W12-W12). The solid squares show the case of tungsten projectile with 20 explicit electrons in the host with 12 electrons (W20-W12). The solid circle data points show the stopping for W20-W20 case while empty circles data points display W26-W20 case.

W20 is only slightly different. Again the \mathcal{S}_e is significantly different (larger) in the higher velocity range ($v \geq 5.0$ a.u.) for W26 in W20 than W20 in W20. In the low velocity range ($v \leq 5.0$ a.u.), the three case W20-W12, W20-W20, and W26-W20 give similar values of the stopping. But when compared to the SRIM data, our best calculated stopping is underestimated by a factor 8 approximately. The experimental data for the \mathcal{S}_e of W in W is almost non-existent. The accuracy of the SRIM model for higher elements is not as good as for lighter elements [58]. However, the apparent discrepancy between

our RT-TDDFT results and the SRIM model is still huge. We believe, taking into account the trend in our results, a major part of this discrepancy can be compensated by gradually allowing more and more explicit valence charge on the projectile. In terms of the computational cost it becomes quite expensive though.

Chapter 8

Conclusions and Outlook

8.1 Conclusions

We have implemented a real-time time-dependent density-functional theory algorithm within the SIESTA method. Building on the basic infrastructure of SIESTA we integrate the time-dependent Kohn-Sham equations using the Crank-Nicolson method. Crank-Nicolson integration and other complementary operations are performed in parallel, allowing for the possibility of simulating systems of thousands of atoms.

We have systematically studied the different aspects of the \mathcal{S}_e of H in bulk Ge, a representative narrow band gap semiconductor for which good experimental results are available. We have learned that the electronic stopping is sensitive to the crystal direction and, in certain directions, to the choice of impact parameter. A detailed model is needed to average the calculated \mathcal{S}_e over different directions. Similarly to what is known for insulators, a finite velocity threshold is found in the calculations, in agreement with what has been observed experimentally. Here the threshold is found to be much better defined (a strict threshold) than in previous similar studies of the \mathcal{S}_e of H in LiF [36], a wide band gap insulator. Careful analysis of the band structure of bulk Ge indicates that the threshold phenomenon is connected to the indirect band gap in given crystal directions. Our results

give further insight into the understanding of the threshold behaviour of the electronic stopping in materials with a band gap.

We have also study the case of He in Ge. The electronic stopping of He in Ge is found to have a very strong dependence on the impact parameter in the low electron density channel. The impact parameter dependence is related to the change in the local electronic density.

The energy loss to electrons in self-irradiated nickel, a paradigmatic transition metal, is studied. The electronic stopping power in the range of keV/Å is accurately calculated from first principles. The experimental data are well reproduced in a projectile velocity range of 1.0 – 12.0 atomic units. The core electrons of the projectile are found to open additional dissipation channels as the projectile velocity increases. The systematic, explicit, and flexible inclusion of the core states reveals that almost all of the energy loss is accounted for within this first principles approach. Core electrons as deep as 2s are treated explicitly and are found to be necessary to account for the ionic energy loss at relatively high projectile velocities.

The electronic stopping power of self-irradiated W further confirms the role of core states in accounting for the extremely high electronic stopping values of the transition and heavy metals.

8.2 Future Outlook

This is, arguably, the first successful calculation of electronic stopping power in the range of keV/Å using a first principles methodology. It establishes the applicability of first principles methods to the class of materials with extremely high stopping powers such as transition and heavy metals. This can be further extended to study the problem of ion energy dissipation and radiation damage in structural alloys (see Fig. [A.3](#)).

In the low velocity regime nuclear stopping power in self-irradiate transition and heavy metals is significantly larger than the electronic stopping power (see Fig. [A.5](#)). This is the most relevant velocity regime for radiation damage.

Both the experimentally measured and theoretically calculated electronic stopping powers may not have been well defined in this regime. We are working on a scheme to redefine the electronic stopping in this regime by coupled ion-electron Ehrenfest dynamics to trace the natural trajectories in contrast to the hyper-channeling conditions (see Fig. A.4). This can be further extended to compute correct initial forces (see Fig. A.2) for large scale classical molecular dynamics simulations of the radiation damage.

The optical response of materials is one of the most important response functions that helps us investigate materials' structure and properties. It has been extensively studied both experimentally and theoretically [172, 173]. Over the years, optical response has been studied within the linear response approximation. The basic assumption is that the external perturbation is rather weak and the excited state does not veer away from the ground state. Hence, a direct frequency-domain formalism is applied to calculate optical response and excitation spectra of the system. However, the frequency domain formalism, as successful as it has been, cannot be applied to systems for which the external perturbation is rather strong. Non-linear effects are significantly strong in plasmon dynamics in nanoparticles. RT-TDDFT allows explicit time domain evolution of the occupied Kohn-Sham states. This approach inherently includes the non-linear and correlation effects up to the adiabatic local density approximation (ALDA). Our parallel implementation of RT-TDDFT within an LCAO formalism makes practical system sizes (thousands of electrons) computationally accessible.

The accurate computation of forces within Ehrenfest dynamics is a straightforward problem when working with plane-wave basis sets. The computational cost, however, is prohibitively large to simulate systems beyond a few hundred atoms. The RT-TDDFT formalism in an LCAO basis is comparatively efficient. However, computing the forces within an LCAO formalism is a slightly complex problem [74, 110] but it would allow simulation of thousands of atoms.

There are a host of interesting phenomena involving non-adiabatic pro-

cesses like the non-adiabatic vibrational damping of molecules off metal surfaces [174, 175] and charge exchange in low-energy ion scattering from the solid surfaces [147]. The application of first principle approaches like RT-TDDFT to such problems is an interesting prospect.

Appendices

Appendix A

Work in progress: Low velocity regime

A.1 Self-irradiated Ge

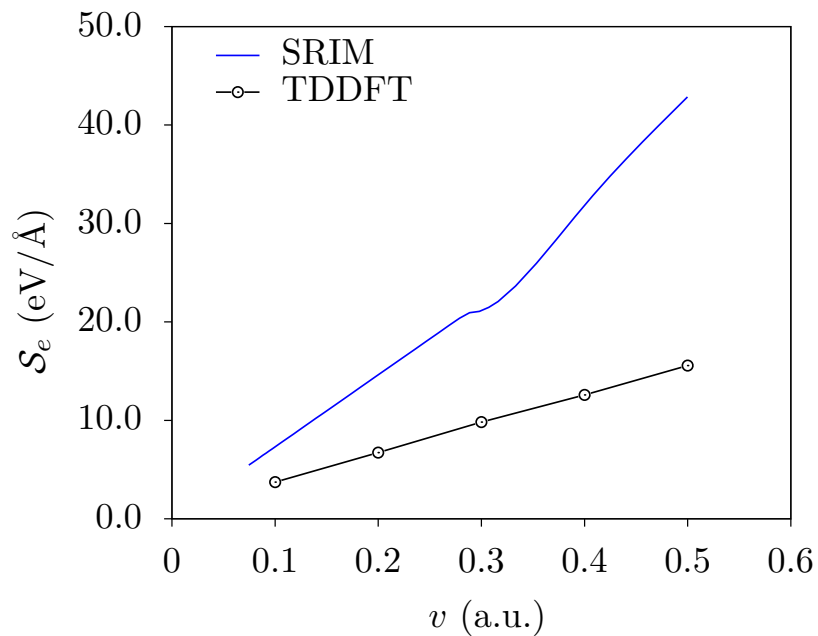


Figure A.1: The electronic stopping power of Ge in Ge in the [111] direction calculated using RT-TDDFT with SIESTA and compared with SRIM data.

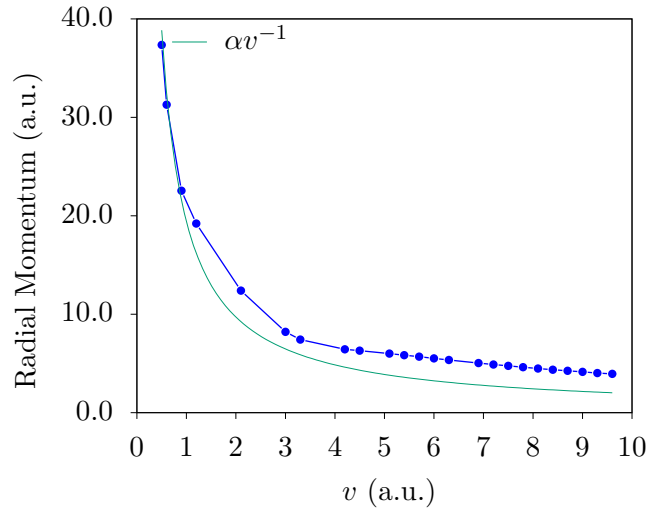


Figure A.2: Ge in Ge: radial momentum transferred to a host atom vs projectile velocity.

A.2 Self-irradiated Ni

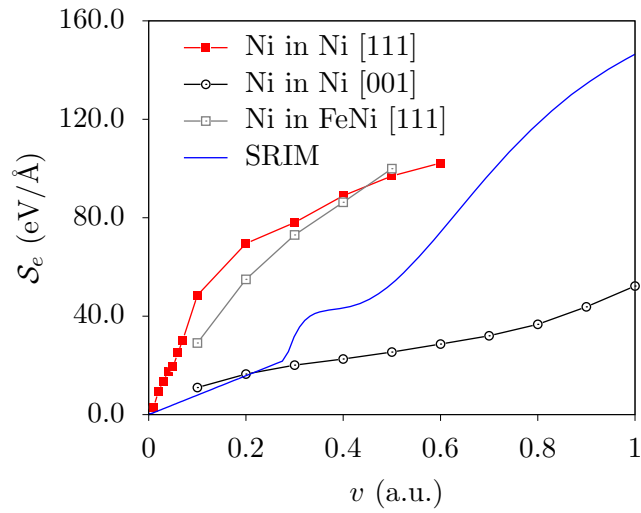


Figure A.3: The electronic stopping power of self-irradiate Ni in two different channels is compared with the electronic stopping power of Ni projectile in Ni crystal where 50% of random Ni sites in the host are replaced with Fe.

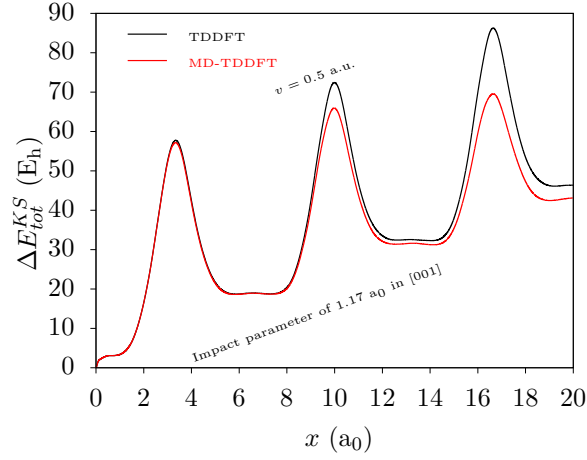


Figure A.4: The change in total Kohn-Sham energy of the electronic subsystem with atoms of the host are frozen (TDDFT) and allowed to move within Ehrenfest dynamics (MD-TDDFT).

A.3 Self-irradiated W

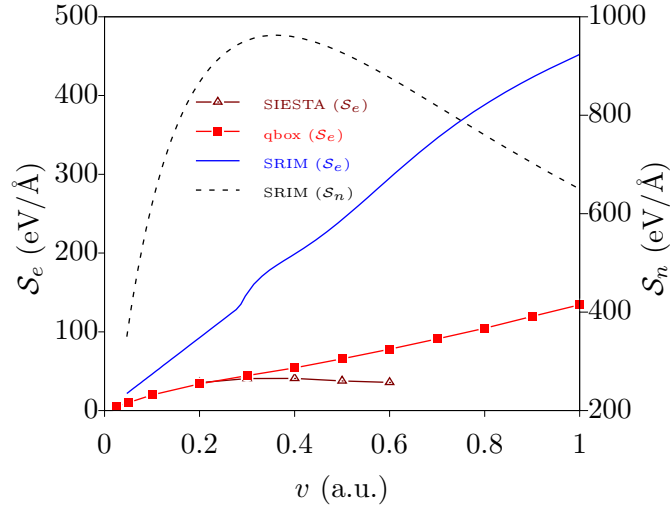


Figure A.5: The electronic stopping power of self-irradiated W with plane-wave basis and LCAO.

Bibliography

- [1] C. P. Race, D. R. Mason, M. H. F. Foo, W. M. C. Foulkes, A. P. Horsfield, and A. P. Sutton. *Quantum-classical simulations of the electronic stopping force and charge on slow heavy channelling ions in metals*. J. Phys Condens. Matter **25**, 125501 (2013) [1, 5, 6, 9].
- [2] N. Bohr. *On the Theory of the Decrease of Velocity of Moving Electrified Particles on Passing Through Matter*. Philos. Mag. **23**, 10 (1912) [2, 4].
- [3] J. F. Ziegler. *Stopping of energetic light ions in elemental matter*. Journal of Applied Physics **85**, 1249 (1999) [2, 6].
- [4] E. Rutherford. *The scattering of α and β particles by matter and the structure of the atom*. Philos. Mag. **21**, 669 (1911) [3].
- [5] W. P. Levin, H. Kooy, J. S. Loeffler, and T. F. DeLaney. *Proton beam therapy*. Br. J. Cancer **93**, 849 (2005) [3, 6].
- [6] D. I. Thwaites and J. B. Tuohy. *Back to the future: the history and development of the clinical linear accelerator*. Phys. Med. Biol. **51**, R343 (2006) [3].
- [7] A. C. Begg, F. A. Stewart, and C. Vens. *Strategies to improve radiotherapy with targeted drugs*. Nat. Rev. Cancer **11**, 239 (2011) [3].
- [8] F. Granberg, K. Nordlund, M. W. Ullah, K. Jin, C. Lu, H. Bei, L. M. Wang, F. Djurabekova, W. J. Weber, and Y. Zhang. *Mechanism of Radiation Damage Reduction in Equiatomic Multicomponent Single Phase Alloys*. Phys. Rev. Lett. **116**, 135504 (2016) [3, 6, 73].

- [9] M. Bagatin and S. Gerardin, eds. *Ionizing Radiation Effects in Electronics: From Memories to Imagers*. CRC Press: Taylor and Francis, 2015 [3, 6].
- [10] P. D. Townsend. *Optical effects of ion implantation*. Rep. Prog. Phys. **50**, 501 (1987) [3, 7].
- [11] P. Sigmund. *Particle Penetration and Radiation Effects: General Aspects and Stopping of Swift Point Charges*. 1st ed. Springer-Verlag Berlin Heidelberg, 2006 [4, 6].
- [12] M. Born. *Zur Quantenmechanik der Stoßvorgänge*. Z. Phys. **37**, 863 (1926) [4].
- [13] H. Bethe. *Zur Theorie des Durchgangs schneller Korpuskularstrahlen durch Materie*. Ann. Phys. **397**, 325 (1930) [4].
- [14] F. Bloch. *Zur Bremsung rasch bewegter Teilchen beim Durchgang durch Materie*. Ann. Phys. **16**, 285 (1933) [4].
- [15] E. Fermi and E. Teller. *The Capture of Negative Mesotrons in Matter*. Phys. Rev. **72**, 399 (1947) [4].
- [16] J. Lindhard. *On the properties of a gas of charged particles*. Dan. Mat. Fys. Medd. **28** (1954) [4].
- [17] R. H. Ritchie. *Interaction of Charged Particles with a Degenerate Fermi-Dirac Electron Gas*. Phys. Rev. **114**, 644 (1959) [4].
- [18] C. O. Almbladh, U. von Barth, Z. D. Popovic, and M. J. Stott. *Screening of a proton in an electron gas*. Phys. Rev. B **14**, 2250 (1976) [5].
- [19] P. Echenique, R. Nieminen, and R. Ritchie. *Density functional calculation of stopping power of an electron gas for slow ions*. Solid State Commun. **37**, 779 (1981) [5, 69].
- [20] P. M. Echenique, R. M. Nieminen, J. C. Ashley, and R. H. Ritchie. *Nonlinear stopping power of an electron gas for slow ions*. Phys. Rev. A **33**, 897 (1986) [5].

- [21] P. M. Echenique, F. Flores, and R. H. Ritchie. “Dynamic Screening of Ions in Condensed Matter”. *Solid State Physics*. Ed. by H. Ehrenreich and D. Turnbull. Vol. 43. Academic Press, 1990, 229 [5, 47].
- [22] I. Nagy, A. Arnau, and P. M. Echenique. *Screening and stopping of charged particles in an electron gas*. Phys. Rev. B **48**, 5650 (1993) [5].
- [23] J. J. Dorado and F. Flores. *Molecular-orbital theory for the stopping power of atoms in the low-velocity regime: The case of helium in alkali metals*. Phys. Rev. A **47**, 3062 (1993) [5].
- [24] I. Campillo, J. M. Pitarke, and A. G. Eguiluz. *Electronic stopping power of aluminum crystal*. Phys. Rev. B **58**, 10307 (1998) [5].
- [25] J. Pitarke and I. Campillo. *Band structure effects on the interaction of charged particles with solids*. Nucl. Instrum. Meth. B **164-165**, 147 (2000) [5].
- [26] J. I. Juaristi, C. Auth, H. Winter, A. Arnau, K. Eder, D. Semrad, F. Aumayr, P. Bauer, and P. M. Echenique. *Unexpected Behavior of the Stopping of Slow Ions in Ionic Crystals*. Phys. Rev. Lett. **84**, 2124 (2000) [5].
- [27] A. Salin, A. Arnau, P. M. Echenique, and E. Zaremba. *Dynamic nonlinear screening of slow ions in an electron gas*. Phys. Rev. B **59**, 2537 (1999) [5].
- [28] N. R. Arista. *Energy loss of ions in solids: Non-linear calculations for slow and swift ions*. Nucl. Instrum. Meth. B **195**, 91 (2002) [5].
- [29] V. U. Nazarov, J. M. Pitarke, C. S. Kim, and Y. Takada. *Time-dependent density-functional theory for the stopping power of an interacting electron gas for slow ions*. Phys. Rev. B **71**, 121106 (2005) [5].

- [30] M. Quijada, A. G. Borisov, I. Nagy, R. D. Muiño, and P. M. Echenique. *Time-dependent density-functional calculation of the stopping power for protons and antiprotons in metals*. Phys. Rev. A **75**, 042902 (2007) [5].
- [31] M. Quijada, A. G. Borisov, and R. D. Muiño. *Time-dependent density functional calculation of the energy loss of antiprotons colliding with metallic nanoshells*. phys. stat. sol. (a) **205**, 1312 (2008) [5].
- [32] N. E. Koval, D. Sánchez-Portal, A. G. Borisov, and R. D. Muiño. *Dynamic screening and energy loss of antiprotons colliding with excited Al clusters*. Nucl. Instrum. Meth. B **317**, Part A, 56 (2013) [5].
- [33] D. R. Mason, J. le Page, C. P. Race, W. M. C. Foulkes, M. W. Finnis, and A. P. Sutton. *Electronic damping of atomic dynamics in irradiation damage of metals*. J Phys. Condens. Matter **19**, 436209 (2007) [5].
- [34] C. P. Race, D. R. Mason, M. W. Finnis, W. M. C. Foulkes, A. P. Horsfield, and A. P. Sutton. *The treatment of electronic excitations in atomistic models of radiation damage in metals*. Rep. Prog. Phys. **73**, 116501 (2010) [5, 9, 47].
- [35] A. A. Shukri, F. Bruneval, and L. Reining. *Ab initio*. Phys. Rev. B **93**, 035128 (2016) [5, 9, 72].
- [36] J. M. Pruneda, D. Sánchez-Portal, A. Arnau, J. I. Juaristi, and E. Artacho. *Electronic Stopping Power in LiF from First Principles*. Phys. Rev. Lett. **99**, 235501 (2007) [5, 10, 29, 47, 71, 88].
- [37] R. Hatcher, M. Beck, A. Tackett, and S. T. Pantelides. *Dynamical Effects in the Interaction of Ion Beams with Solids*. Phys. Rev. Lett. **100**, 103201 (2008) [5, 10, 47, 71].
- [38] A. V. Krasheninnikov, Y. Miyamoto, and D. Tománek. *Role of Electronic Excitations in Ion Collisions with Carbon Nanostructures*. Phys. Rev. Lett. **99**, 016104 (2007) [5, 71].

- [39] A. A. Correa, J. Kohanoff, E. Artacho, D. Sánchez-Portal, and A. Caro. *Nonadiabatic Forces in Ion-Solid Interactions: The Initial Stages of Radiation Damage*. Phys. Rev. Lett. **108**, 213201 (2012) [[5](#), [8](#), [10](#), [29](#), [34](#), [39](#), [47](#), [71](#)].
- [40] M. A. Zeb, J. Kohanoff, D. Sánchez-Portal, A. Arnau, J. I. Juaristi, and E. Artacho. *Electronic Stopping Power in Gold: The Role of d Electrons and the H / He Anomaly*. Phys. Rev. Lett. **108**, 225504 (2012) [[5](#), [8](#), [10](#), [29](#), [34](#), [39](#), [47](#), [48](#), [65](#), [71](#), [72](#)].
- [41] A. Ojanperä, A. V. Krasheninnikov, and M. Puska. *Electronic stopping power from first-principles calculations with account for core electron excitations and projectile ionization*. Phys. Rev. B **89**, 035120 (2014) [[5](#), [10](#), [71](#), [72](#)].
- [42] A. Schleife, Y. Kanai, and A. A. Correa. *Accurate atomistic first-principles calculations of electronic stopping*. Phys. Rev. B **91**, 014306 (2015) [[5](#), [71](#), [72](#), [75](#)].
- [43] Z. Wang, S.-S. Li, and L.-W. Wang. *Efficient Real-Time Time-Dependent Density Functional Theory Method and its Application to a Collision of an Ion with a 2D Material*. Phys. Rev. Lett. **114**, 063004 (2015) [[5](#), [71](#)].
- [44] E. E. Quashie, B. C. Saha, and A. A. Correa. *Electronic band structure effects in the stopping of protons in copper*. Phys. Rev. B **94**, 155403 (2016) [[5](#), [9](#), [10](#), [29](#), [65](#), [71](#), [75](#)].
- [45] A. Lim, W. M. C. Foulkes, A. P. Horsfield, D. R. Mason, A. Schleife, E. W. Draeger, and A. A. Correa. *Electron Elevator: Excitations across the Band Gap via a Dynamical Gap State*. Phys. Rev. Lett. **116**, 043201 (2016) [[5](#), [29](#), [65](#), [71](#)].
- [46] K. G. Reeves, Y. Yao, and Y. Kanai. *Electronic stopping power in liquid water for protons and α particles from first principles*. Phys. Rev. B **94**, 041108 (2016) [[5](#), [10](#), [29](#), [71](#)].

- [47] C.-K. Li, F. Wang, B. Liao, X.-P. OuYang, and F.-S. Zhang. *Ab initio electronic stopping power and threshold effect of channeled slow light ions in HfO₂*. Phys. Rev. B **96**, 094301 (2017) [5, 10, 71].
- [48] D. C. Yost, Y. Yao, and Y. Kanai. *Examining real-time time-dependent density functional theory nonequilibrium simulations for the calculation of electronic stopping power*. Phys. Rev. B **96**, 115134 (2017) [5, 71, 72].
- [49] G. Bi, J. Kang, and L.-W. Wang. *High velocity proton collision with liquid lithium: a time dependent density functional theory study*. Phys. Chem. Chem. Phys. **19**, 9053 (2017) [5, 71].
- [50] B. Boudaïffa, P. Cloutier, D. Hunting, M. A. Huels, and L. Sanche. *Resonant Formation of DNA Strand Breaks by Low-Energy (3 to 20 eV) Electrons*. Science **287**, 1658 (2000) [6].
- [51] S. Duzellier. *Radiation effects on electronic devices in space*. Aerosp. Sci. Techno. **9**, 93 (2005) [7].
- [52] E. Alves, C. Marques, R. da Silva, T. Monteiro, J. Soares, C. McHargue, L. Ononye, and L. Allard. *Structural and optical studies of Co and Ti implanted sapphire*. Nucl. Instrum. Meth. B **207**, 55 (2003) [7].
- [53] L. Malerba. *Molecular dynamics simulation of displacement cascades in α -Fe: A critical review*. J. Nucl. Mater. **351**, 28 (2006) [8].
- [54] A. Caro and M. Victoria. *Ion-electron interaction in molecular-dynamics cascades*. Phys. Rev. A **40**, 2287 (1989) [8].
- [55] M. W. Finnis, P. Agnew, and A. J. E. Foreman. *Thermal excitation of electrons in energetic displacement cascades*. Phys. Rev. B **44**, 567 (1991) [8].
- [56] K. Nordlund, M. Ghaly, R. S. Averback, M. Caturla, T. Diaz de la Rubia, and J. Tarus. *Defect production in collision cascades in elemental semiconductors and fcc metals*. Phys. Rev. B **57**, 7556 (1998) [8].

- [57] J. le Page, D. R. Mason, C. P. Race, and W. M. C. Foulkes. *How good is damped molecular dynamics as a method to simulate radiation damage in metals?* New J. Phys. **11**, 013004 (2009) [8].
- [58] J. F. Ziegler, M. Ziegler, and J. Biersack. *SRIM – The stopping and range of ions in matter (2010)*. Nucl. Instrum. Meth. B **268**, 1818 (2010) [8, 47, 72, 74, 84, 86].
- [59] A. M. Rutherford and D. M. Duffy. *The effect of electron-ion interactions on radiation damage simulations*. J. Phys. Condens. Matter **19**, 496201 (2007) [8, 83].
- [60] A. M. Stoneham. *Energy transfer between electrons and ions in collision cascades in solids*. Nucl. Instrum. Meth. B **48**, 389 (1990) [8].
- [61] A. M. Stoneham. *Finding the gaps: Problems in radiation damage theory*. Radiat. Eff. Defect. S. **142**, 191 (1997) [8].
- [62] G. D. Samolyuk, L. K. Béland, G. M. Stocks, and R. E. Stoller. *Electron-phonon coupling in Ni-based binary alloys with application to displacement cascade modeling*. J. Phys. Condens. Matter **28**, 175501 (2016) [8].
- [63] M. Born and R. Oppenheimer. *Zur Quantentheorie der Molekeln*. Ann. Phys. **389**, 457 (1927) [8, 13].
- [64] C. Race, D. Mason, and A. Sutton. *A new directional model for the electronic frictional forces in molecular dynamics simulations of radiation damage in metals*. J. Nucl. Mater. **425**, 33 (2012) [8, 9].
- [65] D. Mason. *Incorporating non-adiabatic effects in embedded atom potentials for radiation damage cascade simulations*. J. Phys. Condens. Matter **27**, 145401 (2015) [8].
- [66] J. L. Alonso, X. Andrade, P. Echenique, F. Falceto, D. Prada-Gracia, and A. Rubio. *Efficient Formalism for Large-Scale Ab Initio Molecular Dynamics based on Time-Dependent Density Functional Theory*. Phys. Rev. Lett. **101**, 096403 (2008) [8].

- [67] X. Andrade, A. Castro, D. Zueco, J. L. Alonso, P. Echenique, F. Falceto, and A. Rubio. *Modified Ehrenfest Formalism for Efficient Large-Scale ab initio Molecular Dynamics*. J. Chem. Theory Comput. **5**, 728 (2009) [8].
- [68] A. P. Horsfield, D. R. Bowler, A. J. Fisher, T. N. Todorov, and C. G. Sánchez. *Beyond Ehrenfest: correlated non-adiabatic molecular dynamics*. J. Phys. Condens. Matter **16**, 8251 (2004) [9].
- [69] A. P. Horsfield, D. R. Bowler, A. J. Fisher, T. N. Todorov, and C. G. Sánchez. *Correlated electron-ion dynamics: the excitation of atomic motion by energetic electrons*. Journal of Physics: Condensed Matter **17**, 4793 (2005) [9].
- [70] V. Rizzi, T. N. Todorov, J. J. Kohanoff, and A. A. Correa. *Electron-phonon thermalization in a scalable method for real-time quantum dynamics*. Phys. Rev. B **93**, 024306 (2016) [9].
- [71] P. Hohenberg and W. Kohn. *Inhomogeneous Electron Gas*. Phys. Rev. **136**, B864 (1964) [9, 11, 12, 16, 27].
- [72] W. Kohn and L. J. Sham. *Self-Consistent Equations Including Exchange and Correlation Effects*. Phys. Rev. **140**, A1133 (1965) [9, 12, 17, 28].
- [73] E. Runge and E. K. U. Gross. *Density-Functional Theory for Time-Dependent Systems*. Phys. Rev. **52**, 997 (1984) [9, 11, 21, 25, 27].
- [74] T. N. Todorov. *Time-dependent tight binding*. J. Phys. Condens. Matter **13**, 10125 (2001) [9, 33, 37, 90].
- [75] M. A. Zeb, J. Kohanoff, D. Sánchez-Portal, and E. Artacho. *Electronic stopping power of H and He in Al and LiF from first principles*. Nucl. Instrum. Meth. B **303**, 59 (2013) [10, 39, 47, 48, 65].
- [76] N. D. Mermin. *Thermal Properties of the Inhomogeneous Electron Gas*. Phys. Rev. **137**, A1441 (1965) [12].

- [77] J. Kohanoff. *Electronic Structure Calculations for Solids and Molecules*. Cambridge University Press, 2006 [13, 14, 16, 75].
- [78] R. M. Martin. *Electronic Structure*. Cambridge University Press, 2004 [14, 16].
- [79] P. Ehrenfest. *Bemerkung über die angenäherte Gültigkeit der klassischen Mechanik innerhalb der Quantenmechanik*. Z. Phys. **45**, 455 (1927) [14].
- [80] D. M. Ceperley and B. J. Alder. *Ground State of the Electron Gas by a Stochastic Method*. Phys. Rev. Lett. **45**, 566 (1980) [20, 52, 66, 74].
- [81] J. P. Perdew and A. Zunger. *Self-interaction correction to density-functional approximations for many-electron systems*. Phys. Rev. B **23**, 5048 (1981) [20].
- [82] M. A. L. Marques, N. T. Maitra, F. M. S. Nogueira, E. K. U. Gross, and A. Rubio, eds. *Fundamentals of Time-Dependent Density Functional Theory*. Springer-Verlag Berlin Heidelberg, 2012 [23, 25].
- [83] J. M. Soler, E. Artacho, J. D. Gale, A. García, J. Junquera, P. Ordejón, and D. Sánchez-Portal. *The SIESTA method for ab initio order-N materials simulation*. J. Phys. Condens. Matter **14**, 2745 (2002) [26, 29, 48].
- [84] F. Gygi. *Architecture of Qbox: A scalable first-principles molecular dynamics code*. IBM J. Res. Dev. **52**, 137 (2008) [26, 74].
- [85] A. Schleife, E. W. Draeger, Y. Kanai, and A. A. Correa. *Plane-wave pseudopotential implementation of explicit integrators for time-dependent Kohn-Sham equations in large-scale simulations*. J. Chem. Phys. **137**, 22A546 (2012) [26, 29, 32, 37, 43, 74, 75, 85].
- [86] E. W. Draeger, X. Andrade, J. A. Gunnels, A. Bhatele, A. Schleife, and A. A. Correa. *Massively parallel first-principles simulation of electron dynamics in materials*. J. Parallel Distrib. Comput. **106**, 205 (2017) [26, 29, 37, 74].

- [87] K. Yabana and G. F. Bertsch. *Time-dependent local-density approximation in real time*. Phys. Rev. B **54**, 4484 (1996) [29].
- [88] A. Rubio, J. A. Alonso, X. Blase, L. C. Balbás, and S. G. Louie. *Ab Initio Photoabsorption Spectra and Structures of Small Semiconductor and Metal Clusters*. Phys. Rev. Lett. **77**, 247 (1996) [29].
- [89] A. Tsolakidis, D. Sánchez-Portal, and R. M. Martin. *Calculation of the optical response of atomic clusters using time-dependent density functional theory and local orbitals*. Phys. Rev. B **66**, 235416 (2002) [29, 30, 32, 35, 39].
- [90] R. Ullah, F. Corsetti, D. Sánchez-Portal, and E. Artacho. *Electronic stopping power in a narrow band gap semiconductor from first principles*. Phys. Rev. B **91**, 125203 (2015) [29, 34, 39, 71, 75].
- [91] D. C. Yost and Y. Kanai. *Electronic stopping for protons and α particles from first-principles electron dynamics: The case of silicon carbide*. Phys. Rev. B **94**, 115107 (2016) [29].
- [92] M. A. Marques, A. Castro, G. F. Bertsch, and A. Rubio. *octopus: a first-principles tool for excited electron-ion dynamics*. Comput. Phys. Commun. **151**, 60 (2003) [29].
- [93] A. Castro, H. Appel, M. Oliveira, C. A. Rozzi, X. Andrade, F. Lorenzen, M. A. L. Marques, E. K. U. Gross, and A. Rubio. *octopus: a tool for the application of time-dependent density functional theory*. Phys. Status Solidi B **243**, 2465 (2006) [29].
- [94] M. Walter, H. Häkkinen, L. Lehtovaara, M. Puska, J. Enkovaara, C. Rostgaard, and J. J. Mortensen. *Time-dependent density-functional theory in the projector augmented-wave method*. J. Chem. Phys. **128**, 244101 (2008) [29].
- [95] E. Artacho, E. Anglada, O. Diéguez, J. D. Gale, A. García, J. Junquera, R. M. Martin, P. Ordejón, J. M. Pruneda, D. Sánchez-Portal, and J. M. Soler. *The SIESTA method; developments and applicability*. J. Phys. Condens. Matter **20**, 064208 (2008) [29, 30, 48, 51].

- [96] J. Junquera, Ó. Paz, D. Sánchez-Portal, and E. Artacho. *Numerical atomic orbitals for linear-scaling calculations*. Phys. Rev. B **64**, 235111 (2001) [29, 30, 49, 51].
- [97] J. C. Phillips and L. Kleinman. *New Method for Calculating Wave Functions in Crystals and Molecules*. Phys. Rev. **116**, 287 (1959) [29].
- [98] S. Meng and E. Kaxiras. *Real-time, local basis-set implementation of time-dependent density functional theory for excited state dynamics simulations*. J. Chem. Phys **129**, 054110, 054110 (2008) [29, 35].
- [99] G. Kolesov, O. Granas, R. Hoyt, D. Vinichenko, and E. Kaxiras. *Real-Time TD-DFT with Classical Ion Dynamics: Methodology and Applications*. J. Chem. Theory Comput. **12**, 466 (2016) [29].
- [100] P. Ordejón, E. Artacho, and J. M. Soler. *Self-consistent order- N density-functional calculations for very large systems*. Phys. Rev. B **53**, R10441 (1996) [29].
- [101] D. Sánchez-Portal, P. Ordejón, E. Artacho, and J. M. Soler. *Density-functional method for very large systems with LCAO basis sets*. Int. J. Quantum Chem. **65**, 453 (1997) [29].
- [102] E. Artacho, D. Sánchez-Portal, P. Ordejón, A. García, and J. M. Soler. *Linear-Scaling ab-initio Calculations for Large and Complex Systems*. Phys. status solidi B **215**, 809 (1999) [30].
- [103] P. Ordejón. *Linear Scaling ab initio Calculations in Nanoscale Materials with SIESTA*. Phys. status solidi B **217**, 335 (2000) [30].
- [104] M. Brandbyge, J.-L. Mozos, P. Ordejón, J. Taylor, and K. Stokbro. *Density-functional method for nonequilibrium electron transport*. Phys. Rev. B **65**, 165401 (2002) [30].
- [105] N. Papior, N. Lorente, T. Frederiksen, A. García, and M. Brandbyge. *Improvements on non-equilibrium and transport Green function techniques: The next-generation transiesta*. Comput. Phys. Commun. **212**, 8 (2017) [30].

- [106] D. Sánchez-Portal, P. Ordejón, and E. Canadell. “Computing the Properties of Materials from First Principles with SIESTA”. *Principles and Applications of Density Functional Theory in Inorganic Chemistry II*. Springer Berlin Heidelberg, 2004, 103 [30].
- [107] C. Leforestier, R. Bisseling, C. Cerjan, M. Feit, R. Friesner, A. Guldberg, A. Hammerich, G. Jolicard, W. Karrlein, H.-D. Meyer, N. Lipkin, O. Roncero, and R. Kosloff. *A comparison of different propagation schemes for the time dependent Schrödinger equation*. J. Comput. Phys. **94**, 59 (1991) [32].
- [108] A. Castro, M. A. L. Marques, and A. Rubio. *Propagators for the time-dependent Kohn-Sham equations*. J. Chem. Phys. **121**, 3425 (2004) [32].
- [109] J. Crank and P. Nicolson. *A practical method for numerical evaluation of solutions of partial differential equations of the heat-conduction type*. Proc. Camb. Philos. Soc. **43**, 50 (1947) [32].
- [110] T. Kunert and R. Schmidt. *Non-adiabatic quantum molecular dynamics: General formalism and case study H_2^+ in strong laser fields*. Eur. Phys. J. D **25**, 15 (2003) [33, 37, 90].
- [111] E. Artacho and D. D. O’Regan. *Quantum mechanics in an evolving Hilbert space*. Phys. Rev. B **95**, 115155 (2017) [33, 34].
- [112] J. K. Tomfohr and O. F. Sankey. *Time-Dependent Simulation of Conduction through a Molecule*. Phys. Status Solidi B **226**, 115 (2001) [33].
- [113] G. Bao, G. Hu, and D. Liu. *Real-time adaptive finite element solution of time-dependent Kohn-Sham equation*. J. Comput. Phys. **281**, 743 (2015) [35].
- [114] F. Corsetti. *Performance Analysis of Electronic Structure Codes on HPC Systems: A Case Study of SIESTA*. PLOS ONE **9**, 1 (2014) [41].

- [115] F. Corsetti. *The orbital minimization method for electronic structure calculations with finite-range atomic basis sets*. *Comput. Phys. Commun.* **185**, 873 (2014) [41, 42].
- [116] E. Anderson, A. Benzoni, J. Dongarra, S. Moulton, S. Ostrouchov, B. Tourancheau, and R. van de Geijn. “Basic Linear Algebra Communication Subprograms”. *The Sixth Distributed Memory Computing Conference, 1991. Proceedings*. 1991, 287 [41].
- [117] L. S. Blackford, J. Choi, A. Cleary, E. D’Azevedo, J. Demmel, I. Dhillon, J. Dongarra, S. Hammarling, G. Henry, A. Petitet, K. Stanley, D. Walker, and R. C. Whaley. *ScaLAPACK Users’ Guide*. Society for Industrial and Applied Mathematics, Philadelphia, PA, 1997 [41].
- [118] V. W. Yu, F. Corsetti, A. García, W. P. Huhn, M. Jacquelin, W. Jia, B. Lange, L. Lin, J. Lu, W. Mi, A. Seifitokaldani, Á. Vázquez-Mayagoitia, C. Yang, H. Yang, and V. Blum. *ELSI: A unified software interface for Kohn-Sham electronic structure solvers*. *Comput. Phys. Commun.*, in press DOI: 10.1016/j.cpc.2017.09.007 (2017) [43].
- [119] F. Corsetti, A. A. Mostofi, and J. Lischner. *First-principles multiscale modelling of charged adsorbates on doped graphene*. *2D Mater.* **4**, 025070 (2017) [43].
- [120] F. Tisseur and J. Dongarra. *A Parallel Divide and Conquer Algorithm for the Symmetric Eigenvalue Problem on Distributed Memory Architectures*. *SIAM J. Sci. Comput.* **20**, 2223 (1999) [43].
- [121] R. Cabrera-Trujillo, P. Apell, J. Oddershede, and J. R. Sabin. *Why does the maximum in the stopping cross section for protons occur at approximately 100 keV most of the time?* *AIP Conf. Proc.* **680**, 86 (2003) [47].
- [122] A. Mertens and H. Winter. *Energy Transfer from Fast Atomic Projectiles to a Crystal Lattice under Channeling Conditions*. *Phys. Rev. Lett.* **85**, 2825 (2000) [47].

- [123] S. N. Markin, D. Primetzhofer, S. Prusa, M. Brunmayr, G. Kowarik, F. Aumayr, and P. Bauer. *Electronic interaction of very slow light ions in Au: Electronic stopping and electron emission*. Phys. Rev. B **78**, 195122 (2008) [47].
- [124] S. N. Markin, D. Primetzhofer, M. Spitz, and P. Bauer. *Electronic stopping of low-energy H and He in Cu and Au investigated by time-of-flight low-energy ion scattering*. Phys. Rev. B **80**, 205105 (2009) [47, 65].
- [125] D. Primetzhofer, S. Rund, D. Roth, D. Goebel, and P. Bauer. *Electronic Excitations of Slow Ions in a Free Electron Gas Metal: Evidence for Charge Exchange Effects*. Phys. Rev. Lett. **107**, 163201 (2011) [47, 65].
- [126] S. N. Markin, D. Primetzhofer, and P. Bauer. *Vanishing Electronic Energy Loss of Very Slow Light Ions in Insulators with Large Band Gaps*. Phys. Rev. Lett. **103**, 113201 (2009) [47, 48, 65].
- [127] D. Roth, D. Goebel, D. Primetzhofer, and P. Bauer. *A procedure to determine electronic energy loss from relative measurements with TOF-LEIS*. Nucl. Instrum. Meth. B **317, Part A**, 61 (2013) [47, 53–55, 65].
- [128] J. F. Ziegler and J. P. Biersack. “The Stopping and Range of Ions in Matter”. *Treatise on Heavy-Ion Science*. Ed. by D. A. Bromley. Vol. 6. Springer, New York, 1985, 93 [47].
- [129] D. Goebel, K. Khalal-Kouache, D. Roth, E. Steinbauer, and P. Bauer. *Energy loss of low-energy ions in transmission and backscattering experiments*. Phys. Rev. A **88**, 032901 (2013) [47, 65].
- [130] E. Anglada, J. M. Soler, J. Junquera, and E. Artacho. *Systematic generation of finite-range atomic basis sets for linear-scaling calculations*. Phys. Rev. B **66**, 205101 (2002) [49].
- [131] N. Troullier and J. L. Martins. *Efficient pseudopotentials for plane-wave calculations*. Phys. Rev. B **43**, 1993 (1991) [49, 66].

- [132] L. Kleinman and D. M. Bylander. *Efficacious Form for Model Pseudopotentials*. Phys. Rev. Lett. **48**, 1425 (1982) [49, 66, 74, 85].
- [133] J. M. Pruneda and E. Artacho. *Short-range repulsive interatomic interactions in energetic processes in solids*. Phys. Rev. B **70**, 035106 (2004) [49].
- [134] H. J. Monkhorst and J. D. Pack. *Special points for Brillouin-zone integrations*. Phys. Rev. B **13**, 5188 (1976) [52, 53, 66].
- [135] J. Moreno and J. M. Soler. *Optimal meshes for integrals in real- and reciprocal-space unit cells*. Phys. Rev. B **45**, 13891 (1992) [52, 66].
- [136] P. Śpiewak, K. J. Kurzydłowski, K. Sueoka, I. Romandic, and J. Vanhellefont. *First Principles Calculations of the Formation Energy of the Neutral Vacancy in Germanium*. Solid State Phenom. **131-133**, 241 (2008) [52].
- [137] A. J. Lee, M. Kim, C. Lena, and J. R. Chelikowsky. *Mechanical and electronic properties of strained Ge nanowires using ab initio real-space pseudopotentials*. Phys. Rev. B **86**, 115331 (2012) [52].
- [138] J. R. Chelikowsky, T. J. Wagener, J. H. Weaver, and A. Jin. *Valence- and conduction-band densities of states for tetrahedral semiconductors: Theory and experiment*. Phys. Rev. B **40**, 9644 (1989) [52].
- [139] J. P. Perdew, K. Burke, and M. Ernzerhof. *Generalized Gradient Approximation Made Simple*. Phys. Rev. Lett. **77**, 3865 (1996) [52].
- [140] X. Gonze, B. Amadon, P.-M. Anglade, J.-M. Beuken, F. Bottin, P. Boulanger, F. Bruneval, D. Caliste, R. Caracas, M. Côté, T. Deutsch, L. Genovese, P. Ghosez, M. Giantomassi, S. Goedecker, D. Hamann, P. Hermet, F. Jollet, G. Jomard, S. Leroux, M. Mancini, S. Mazevet, M. Oliveira, G. Onida, Y. Pouillon, T. Rangel, G.-M. Rignanese, D. Sangalli, R. Shaltaf, M. Torrent, M. Verstraete, G. Zerah, and J. Zwanziger. *ABINIT: First-principles approach to material and nanosystem properties*. Comput. Phys. Commun. **180**, 2582 (2009) [52].

- [141] E. Artacho. *Electronic Stopping in insulators: A simple model*. J. Phys. Condens. Matter **19**, 275211 (2007) [54, 57, 59].
- [142] N.-p. Wang and I. Nagy. *Nonlinear calculations of the stopping power for slow hydrogen and helium projectiles in solids*. Phys. Rev. A **56**, 4795 (1997) [62].
- [143] N.-p. Wang, I. Nagy, and P. M. Echenique. *Constrained local plasma density approximation for the calculation of the stopping power for slow ions in solids*. Phys. Rev. B **58**, 2357 (1998) [62].
- [144] H. Winter, J. I. Juaristi, I. Nagy, A. Arnau, and P. M. Echenique. *Energy loss of slow ions in a nonuniform electron gas*. Phys. Rev. B **67**, 245401 (2003) [62].
- [145] L. Martin-Gondre, G. A. Bocan, M. Blanco-Rey, M. Alducin, J. I. Juaristi, and R. Díez Muiño. *Scattering of Nitrogen Atoms off Ag(111) Surfaces: A Theoretical Study*. J. Phys. Chem. C **117**, 9779 (2013) [62].
- [146] D. Roth, B. Bruckner, M. V. Moro, S. Gruber, D. Goebel, J. I. Juaristi, M. Alducin, R. Steinberger, J. Duchoslav, D. Primetzhofer, and P. Bauer. *Electronic Stopping of Slow Protons in Transition and Rare Earth Metals: Breakdown of the Free Electron Gas Concept*. Phys. Rev. Lett. **118**, 103401 (2017) [65].
- [147] D. Goebel, D. Roth, D. Primetzhofer, R. C. Monreal, E. Abad, A. Putz, and P. Bauer. *Quasi-resonant neutralization of He⁺ ions at a germanium surface*. J. Phys. Condens. Matter **25**, 485006 (2013) [65, 91].
- [148] D. Roth. “Electronic interactions of H and He ions with solids: Fundamentals and applications”. PhD Dissertation. 2017 [65, 67, 68].
- [149] T. D. de la Rubia, R. S. Averback, R. Benedek, and W. E. King. *Role of thermal spikes in energetic displacement cascades*. Phys. Rev. Lett. **59**, 1930 (1987) [72].

- [150] M. Caro, A. A. Correa, E. Artacho, and A. Caro. *Stopping power beyond the adiabatic approximation*. Sci. Rep. **7**, 2618 (2017) [73].
- [151] C. Lu, L. Niu, N. Chen, K. Jin, T. Yang, P. Xiu, Y. Zhang, F. Gao, H. Bei, S. Shi, M.-R. He, I. M. Robertson, W. J. Weber, and L. Wang. *Enhancing radiation tolerance by controlling defect mobility and migration pathways in multicomponent single-phase alloys*. Nat. Commun. **7**, 13564 (2016) [73].
- [152] K. Jin, B. C. Sales, G. M. Stocks, G. D. Samolyuk, M. Daene, W. J. Weber, Y. Zhang, and H. Bei. *Tailoring the physical properties of Ni-based single-phase equiatomic alloys by modifying the chemical complexity*. Sci. Rep. **6**, 20159 (2016) [73].
- [153] Y. Zhang, K. Jin, H. Xue, C. Lu, R. J. Olsen, L. K. Beland, M. W. Ullah, S. Zhao, H. Bei, D. S. Aidhy, and et al. *Influence of chemical disorder on energy dissipation and defect evolution in advanced alloys*. J. Mater. Res. **31**, 2363 (2016) [73].
- [154] E. Levo, F. Granberg, C. Fridlund, K. Nordlund, and F. Djurabekova. *Radiation damage buildup and dislocation evolution in Ni and equiatomic multicomponent Ni-based alloys*. J. Nucl. Mater. **490**, 323 (2017) [73].
- [155] J. Bates and R. Powell. *Irradiation-induced swelling in commercial alloys*. J. Nucl. Mater. **102**, 200 (1981) [73].
- [156] Y. Osetsky, N. Anento, A. Serra, and D. Terentyev. *The role of nickel in radiation damage of ferritic alloys*. Acta Mater. **84**, 368 (2015) [73].
- [157] F. X. Zhang, S. Zhao, K. Jin, H. Xue, G. Velisa, H. Bei, R. Huang, J. Y. P. Ko, D. C. Pagan, J. C. Neuefeind, W. J. Weber, and Y. Zhang. *Local Structure and Short-Range Order in a NiCoCr Solid Solution Alloy*. Phys. Rev. Lett. **118**, 205501 (2017) [73].
- [158] J. F. Ziegler. *SRIM-2003*. Nucl. Instrum. Meth. B **219**, 1027 (2004) [76, 77].

- [159] M. Fuchs and M. Scheffler. *Ab initio pseudopotentials for electronic structure calculations of poly-atomic systems using density-functional theory*. Comput. Phys. Commun. **119**, 67 (1999) [75].
- [160] A. M. Rappe, K. M. Rabe, E. Kaxiras, and J. D. Joannopoulos. *Optimized pseudopotentials*. Phys. Rev. B **41**, 1227 (1990) [75].
- [161] I. Grinberg, N. J. Ramer, and A. M. Rappe. *Transferable relativistic Dirac-Slater pseudopotentials*. Phys. Rev. B **62**, 2311 (2000) [75].
- [162] M. Rieth, J. Boutard, S. Dudarev, T. Ahlgren, S. Antusch, N. Baluc, M.-F. Barthe, C. Becquart, L. Ciupinski, J. Correia, C. Domain, J. Fikar, E. Fortuna, C.-C. Fu, E. Gaganidze, T. Galán, C. García-Rosales, B. Gludovatz, H. Greuner, K. Heinola, N. Holstein, N. Juslin, F. Koch, W. Krauss, K. Kurzydowski, J. Linke, C. Linsmeier, N. Luzginova, H. Maier, M. Martínez, J. Missiaen, M. Muhammed, A. Muñoz, M. Muzyk, K. Nordlund, D. Nguyen-Manh, P. Norajitra, J. Opschoor, G. Pintsuk, R. Pippan, G. Ritz, L. Romaner, D. Rupp, R. Schäublin, J. Schlosser, I. Uytendhouwen, J. van der Laan, L. Veleva, L. Ventelon, S. Wahlberg, F. Willaime, S. Wurster, and M. Yar. *Review on the EFDA programme on tungsten materials technology and science*. J. Nucl. Mater. **417**, 463 (2011) [83].
- [163] Y. Hatano, M. Shimada, V. Alimov, J. Shi, M. Hara, T. Nozaki, Y. Oya, M. Kobayashi, K. Okuno, T. Oda, G. Cao, N. Yoshida, N. Futagami, K. Sugiyama, J. Roth, B. Tyburska-Püschel, J. Dorner, I. Takagi, M. Hatakeyama, H. Kurishita, and M. Sokolov. *Trapping of hydrogen isotopes in radiation defects formed in tungsten by neutron and ion irradiations*. J. Nucl. Mater. **438**, S114 (2013) [83].
- [164] B. Khripunov, V. Koidan, A. Ryazanov, V. Gureev, S. . Kornienko, S. Latushkin, A. Rupyshev, E. Semenov, V. Kulikauskas, and V. Zatekin. *Study of Tungsten as a Plasma-facing Material for a Fusion Reactor*. Phys. Procedia **71**, 63 (2015) [83].

- [165] X. Yi, M. Jenkins, M. Briceno, S. Roberts, Z. Zhou, and M. Kirk. *In situ study of self-ion irradiation damage in W and W-5Re at 500 °C*. Philos. Mag. **93**, 1715 (2013) [83].
- [166] A. E. Sand, S. L. Dudarev, and K. Nordlund. *High-energy collision cascades in tungsten: Dislocation loops structure and clustering scaling laws*. EPL (Europhysics Letters) **103**, 46003 (2013) [83].
- [167] D. M. Duffy and A. M. Rutherford. *Including the effects of electronic stopping and electron-ion interactions in radiation damage simulations*. J. Phys. Condens. Matter **19**, 016207 (2007) [83].
- [168] E. Zarkadoula, S. L. Daraszewicz, D. M. Duffy, M. A. Seaton, I. T. Todorov, K. Nordlund, M. T. Dove, and K. Trachenko. *Electronic effects in high-energy radiation damage in iron*. Journal of Physics: Condensed Matter **26**, 085401 (2014) [83].
- [169] E. Zarkadoula, D. M. Duffy, K. Nordlund, M. A. Seaton, I. T. Todorov, W. J. Weber, and K. Trachenko. *Electronic effects in high-energy radiation damage in tungsten*. J. Phys. Condens. Matter **27**, 135401 (2015) [84].
- [170] A. Caro, A. A. Correa, A. Tamm, G. D. Samolyuk, and G. M. Stocks. *Adequacy of damped dynamics to represent the electron-phonon interaction in solids*. Phys. Rev. B **92**, 144309 (2015) [84].
- [171] A. Tamm, G. Samolyuk, A. A. Correa, M. Klintonberg, A. Aabloo, and A. Caro. *Electron-phonon interaction within classical molecular dynamics*. Phys. Rev. B **94**, 024305 (2016) [84].
- [172] S. Huotari. “Spectroscopy in the Frequency Domain”. *Fundamentals of Time-Dependent Density Functional Theory*. Ed. by M. A. Marques, N. T. Maitra, F. M. Nogueira, E. Gross, and A. Rubio. Springer Berlin Heidelberg, 2012, 15 [90].
- [173] A. Rubio, J. A. Alonso, X. Blase, and S. G. Louie. *Theoretical Models for the Optical Properties of Clusters and Nanostructures*. International Journal of Modern Physics B **11**, 2727 (1997) [90].

- [174] N. Shenvi, S. Roy, and J. C. Tully. *Dynamical Steering and Electronic Excitation in NO Scattering from a Gold Surface*. *Science* **326**, 829 (2009) [91].
- [175] S. P. Rittmeyer, J. Meyer, and K. Reuter. *Nonadiabatic Vibrational Damping of Molecular Adsorbates: Insights into Electronic Friction and the Role of Electronic Coherence*. *Phys. Rev. Lett.* **119**, 176808 (2017) [91].

NON-ADIABATIC PROCESSES IN THE RADIATION DAMAGE OF MATERIALS
FROM FIRST PRINCIPLES

Rafi Ullah

2018



CIC nanoGUNE
Ave. Tolosa 76, Donostia - San Sebastian
Spain.